ANALYSIS AND DESIGN OF ULTRASOUND PHASED ARRAYS FOR HYPERTHERMIA CANCER THERAPY

BY

MOHAMMED SALAMEH IBBINI

Dipl., Universite de Caen, 1978
M.S., University of Colorado, 1980

THESIS

Submitted in partial fulfillment of the requirements
for the degree of Doctor of Philosophy in Electrical Engineering
in the Graduate College of the
University of Illinois at Urbana-Champaign, 1988

Urbana, Illinois

ANALYSIS AND DESIGN OF ULTRASOUND PHASED ARRAYS FOR HYPERTHERMIA CANCER THERAPY

Mohammed Salameh Ibbini, Ph. D.
Department of Electrical and Computer Engineering
University of Illinois at Urbana-Champaign 1988
Charles Cain, Advisor

Acoustic phased arrays, which can be focused and steered electronically, offer an attractive alternative to the mechanically scanned focused ultrasound systems currently in use in hyperthermia cancer therapy. However, both electrical and mechanical scannings require a very intense focal spot which could increase the risk of unwanted nonthermal effects such as cavitation. In addition, hot spots proximal to the tumor may occur because of the near-field beam overlapping due to scanning. This thesis introduces a new method which will allow the direct synthesis, without scanning, of the more diffuse heating patterns useful in hyperthermia. Two quite different phased arrays are theoretically evaluated as hyperthermia applicators: a concentric ring array (CRA), and an NxN square-element array.

The new synthesis method is based on the conjugate phase and amplitude matching techniques often used in optics.The field conjugation method (FCM), theoretically capable of tailoring the ultrasonic power deposition to virtually any tumor geometry without scanning, offers also the possibility of simultaneously focusing at different locations. The multiple focusing feature is combined with a new phasing technique involving angular phase rotation to eliminate hot spots that are often associated with the synthesis of annular patterns.

A concentric-ring array was chosen because of its ability to directly produce annular patterns with a minimum number of array elements. However, computer simulations demonstrated that the use of directly synthesized annular intensity profiles for heating could be severely limited due to the formation of undesired hot spots along the array axis. A new method, based on combining the multiple focusing feature and a simple mechanical

movement of the applicator, is proposed as a means of heating different size tumors at various depths.

While a concentric-ring array is limited to the synthesis of annular and spot foci, an NxN square-element array is investigated as a means of synthesizing heating patterns with or without circular symmetry. Simulated heating patterns produced by the FCM are compared to those produced by electronic scanning. Although the two techniques result in equivalent power deposition patterns, the SPTP focal intensity associated with the FCM is substantially lower than that used for scanning. A method is also proposed to combine the FCM with electronic scanning to produce more complicated diffuse heating patterns. The advantage of this method is to minimize the number of scan points and, hence, to use a lower SPTP intensity. Moreover, an 8X8 square-element phased array prototype built and radiation patterns produced by single and multiple elements were measured, and agreed well with theoretically predicted patterns..

To evaluate the different applicators, the steady-state bioheat transfer equation was solved using a finite difference technique. The simulated temperature distributions associated with different power deposition patterns demonstrate the potential of the field conjugation technique for the design of diffuse heating patterns for hyperthermia cancer therapy.

DEDICATION

Dedicated to the soul of my father, Salameh Ali Ibbini, whose love, support, and encouragement for me were, unlike his life, unlimited.

ACKNOWLEDGEMENTS

The author is indebted to his advisor, Professor Charles A. Cain, for his time, suggestions, and especially his moral support provided during this project. Thanks to Professor Leon A. Frizzell and Dr. Shin-Ichiro Umemura for their very helpful discussions. Thanks are also extended to Professors W. O'Brien and S. Lee for serving on my committee. Thanks are due to my brother, Emad, for his exemplary moral support he provided, particularly during the last 18 months of this work. Wanda Elliot, Billy McNeill, Joe Cobb, and Robert Cicone deserve many thanks for their help and assistance. My appreciation goes to the NCSA staff and students for their help and assistance which made the computer simulations on their supercomputer (CRAYX-MP48) very enjoyable. Special thanks to all the Bioacoustics Research Laboratory staff and students who made the laboratory an excellent work environment. The continuous support and love provided by my family will always be remembered. The biggest thanks of all goes to my wife, Etaf, and my children, Emad and Esam, for putting up with me during the different stages of this thesis. In particular, Etaf's effort to put up with me and with Esam, while he was patient in the hospital, during six months of this work, is to be remembered.

This work was funded in part by Grant CA44124 from the National Institute of Health, an award from Hitachi Central Research Laboratory, Hitachi, LTD, Tokyo, Japan, and Grant ECS870001 from the National Center for Supercomputer Applications (NCSA) at the University of Illinois.

TABLE OF CONTENTS

CHAPTER		PAGE
1	INTRODUCTION	1
2	DIRECT SYNTHESIS OF DIFFUSE INTENSITY PROFILE PATTERNS USING A FIELD CONJUGATION TECHNIQUE	5
3	ANALYSIS AND DESIGN OF A CONCENTRIC-RING ARRAY	32
4	ANALYSIS AND DESIGN OF AN NxN SQUARE-ELEMENT ULTRASONIC PHASED ARRAY	101
5	SIMULATED TEMPERATURE DISTRIBUTIONS ASSOCIATED WITH HEATING BY A CONCENTRIC-RING APPLICATOR	148
6	THE SIMULATED TEMPERATURE DISTRIBUTIONS ASSOCIATED WITH HEATING BY AN NxN SQUARE-ELEMENT ARRAY	190
7	PRELIMINARY EVALUATION OF A PROTOTYPE SQUARE-ELEMENT ARRAY	218
8	RECOMMENDATIONS FOR FUTURE RESEARCH	236
	APPENDIX A--- NxN SQUARE-ELEMENT ARRAY FIELD PROGRAM	239
	APPENDIX B--- CYLINDRICAL BIOHEAT EQUATION PROGRAM	251
	APPENDIX C--- THREE-DIMENSIONAL BIOHEAT EQUATION PROGRAM	257
	REFERENCES	261
	VITA	265

CHAPTER 1

INTRODUCTION

The use of hyperthermia, or elevated temperature, in the treatment of malignant tissues was initiated by the Roman and Greek physicians more than twenty centuries ago [1,2]. However, attitude toward hyperthermia went through different stages of optimism and pessimism within the last few decades [3]. The resurgent interest in hyperthermia cancer therapy today is probably due to an increased number of investigators confirming the higher sensitivity of malignant and tumorous tissue to induced heat compared to that of normal tissue [4-7]. While it is now well established that tumor cells are more sensitive to heat than normal tissue cells, the difference between these sensitivities is not very well known but believed to be rather small [8]. This last statement emphasizes the importance of a precise control of the induced heat if hyperthermia is to be recognized as an efficient and safe cancer treatment. An ideal hyperthermia treatment would consist of raising the tumor temperature to therapeutic levels while keeping the surrounding tissue temperature level below thresholds that can cause damage to normal tissue.

Different modalities can be used to induce heat in tissue noninvasively. Among those modalities are EM waves, radio frequency current, and ultrasound energy. However, ultrasound may be the modality of choice for the treatment of deep seated tumors. In fact, the small size of its wavelength and its relatively low attenuation in tissue, at the frequencies of interest (0.3-3.0 MHz), make ultrasound superior to any other noninvasive modality for the production of localized heat at depth [9]. Another advantage of ultrasound is that it does not require special arrangements such as shielding and the use of particular measures to ensure the safety of the operating technicians as opposed to other modalities. A serious problem with ultrasound is its impedance mismatch at tissue-gas and tissue-bone interfaces. The ultrasonic energy is almost totally reflected (99%) at a tissue-air interface, while about 50%

reflection occurs at the interface between tissue and bone. Moreover, the ultrasonic absorption coefficient in bone is many times greater than that in tissue, and hence, bone or air cavities make some body regions inaccessible to noninvasive ultrasound.

Unfocused ultrasound can be used to heat superficial tumors but cannot produce therapeutic gain at depth [10]. Focused transducers can be used to concentrate the ultrasonic energy into a small region deep in the body. However, the small size of the resulting focal spot makes it difficult to heat typical size tumors without some manipulation. This problem can be resolved by mechanically translocating the applicator so that the focal spot is swept over a desired path, a technique known as mechanical scanning. Several mechanical scanning systems are currently in clinical use [11-13]. Mechanical scanning, while demonstrating the possibility of localized focused treatment at depth, suffers generally from a lack of speed, allowing only a crude control of power deposition and a complex and cumbersome patient-machine interface due to the mechanical movement of a transducer which must be continuously coupled to the tissue.

Phased arrays, which can be focused and steered electronically, offer an attractive alternative to the mechanical scanning of focused systems. This could be attributed in part to the speed and flexibility of electronic control systems which, while complex, can be implemented remotely from the applicator aperture. Electronic scanning offers the advantage of eliminating the need of any mechanical movement of the transducer, allowing a more precise electronic control, and permitting the scanning of very irregular heating patterns as compared to the simple ones achieved by mechanical scanning. A number of phased array configurations have been investigated [14-16].

Both electronic and mechanical scanning require the use of high spatial-peak temporal-peak focal intensity ultrasound. This requirement is crucial to compensate for the short dwell time (time spent at each scan point) to eliminate thermal ripples. Recently, phased array applicators of particular configurations were proposed which were capable of directly synthesizing diffuse intensity profiles without electrical or mechanical scanning [17].

This thesis will introduce a new general method which is expected to allow the direct synthesis of optimal laterally diffuse intensity profiles. As a demonstration, two quite different array configurations are examined, a concentric-ring and a square-element NxN phased array.

In Chapter 2, a method based on phase and amplitude matching concepts will be proposed as a means of directly synthesizing many heating patterns useful in hyperthermia. Besides its capability of producing conventional foci (intense focal spots), the field conjugation method can potentially be used to directly tailor the heating pattern to the geometry of the tissue to be heated. The method can also be used to produce multiple foci at different locations which can be useful in different hyperthermia applications (i.e., heating of large tumors). The direct synthesis of diffuse heating patterns is achieved by splitting the array focal intensity over a larger volume and, hence, a focal intensity lower than those associated with scanning can be used. The method can also be used in clinical situations where tissue inhomogeneity might decrease the focusing capability of conventional focusing systems which primarily use geometrical concepts in establishing the relative excitation phase for each array element.

The capability of a concentric-ring array of producing power deposition patterns useful for hyperthermia applications is analyzed in Chapter 3. The applicator geometry was chosen for its capability of producing 3-D focusing volumes with a minimum number of elements compared to the large number of elements generally required by 2-D phased arrays. While computer simulations demonstrate the possibility of producing conventional (spot foci) and annular foci uniquely by adjusting the electronic control circuitry, a new technique combining mechanical and electrical scanning is proposed as a means of producing optimal heating patterns that probably cannot be produced by either type of scanning separately.

A square-element NxN phased array is then chosen to produce intensity profiles that cannot be produced by a concentric-ring applicator. In particular, patterns with or without circular symmetry are synthesized and analyzed. The direct synthesis technique is then

compared to electronic scanning of an intense focal spot and shown to be a potential alternative to scanning. A combination of electronic scanning and direct synthesis techniques is also proposed and some resulting heating patterns are simulated.

Investigated in Chapter 5 is the thermal response associated with some power deposition patterns of Chapter 3. To obtain the temperature distributions, a geometrical thermal model of the tumor and surrounding tissue is adopted and the method of finite difference with over-relaxation is used to solve the 2-D radially symmetrical bioheat equation.

A 3-D thermal model is proposed in Chapter 6 and the finite difference with over-relaxation technique is used to solve the 3-D bioheat transfer equation in rectangular coordinates. An evaluation of the direct technique as a means of synthesizing different heating patterns using an NxN square-element applicator is offered. Temperature distributions resulting from direct synthesis, electronic scanning, and their combinations are simulated and discussed.

The fabrication process of an 8x8 square-element phased array prototype is described in Chapter 7. In particular, practical problems such as PZT handling, impedance matching, and electronic control are discussed. The frequency response of the PZT-8 ceramic electrical impedance is measured and the resonance frequency is determined. Experimental data of a preliminary study of the array radiation patterns are presented and compared to theoretically predicted simulations.

This thesis is concluded in Chapter 8 with some suggestions for future research in hyperthermia cancer therapy applicators design.

CHAPTER 2

DIRECT SYNTHESIS OF DIFFUSE INTENSITY PROFILE PATTERNS USING A FIELD CONJUGATION TECHNIQUE

2.1 Introduction

Heating the periphery of a poorly perfused tumor is more efficient than uniform heating throughout the treated volume if the goal is to obtain a uniform temperature distribution within the tumor tissue [10]. By delivering enough energy at the edges of the tumor to compensate for the heat losses to surrounding normal tissues by conduction or convection, the temperature of the whole tumor volume might be raised evenly to a therapeutic level ($\geq 42^{\circ}$ C).

Several techniques are currently used to deposit the ultrasonic energy at the tumor periphery. These techniques range from simply aiming several unfocused transducers at points around the tumor periphery to scanning an intense focal spot along the tumor border using sophisticated electronics. Fessenden et al. proposed a system consisting of six unfocused transducers mounted in a spherical shell section and driven at slightly different frequencies [18]. This arrangement is capable of producing a waist of focal points around the tumor. Moreover, a specially designed lens, to deposit the ultrasonic energy around the tumor periphery, was simultaneously proposed by Lele [19] and Beard et al. [20]. Lele also proposed a similar design to heat the tumor periphery and its center as well. This later design can be used to heat well perfused or larger tumors (diameter > 20 mm) for which heating the periphery might prove inadequate.

Figure 2.1a) is a schematic of the geometry of the multitransducer system developed at Stanford (Fessenden) while Figures 2.1b) and c) illustrate a cross section of the specially designed lenses proposed by Lele. The main disadvantage of the multitransducer system and the specially designed lenses is their inflexibility for treatment of different tumor geometries

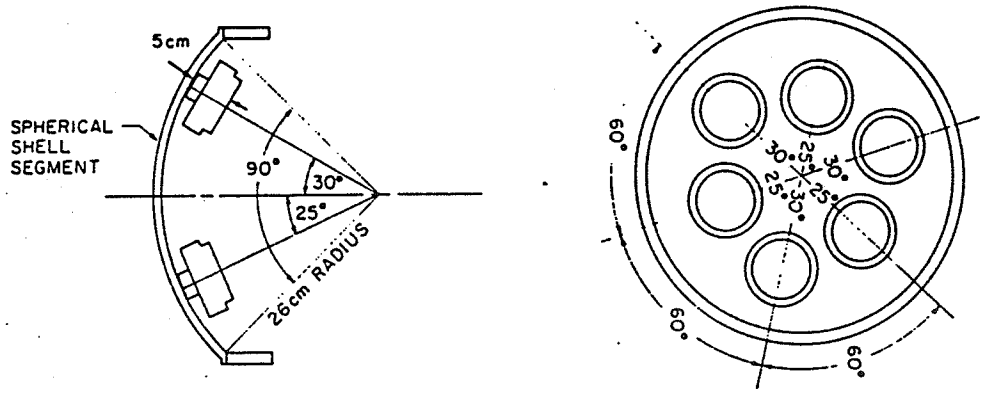

a)

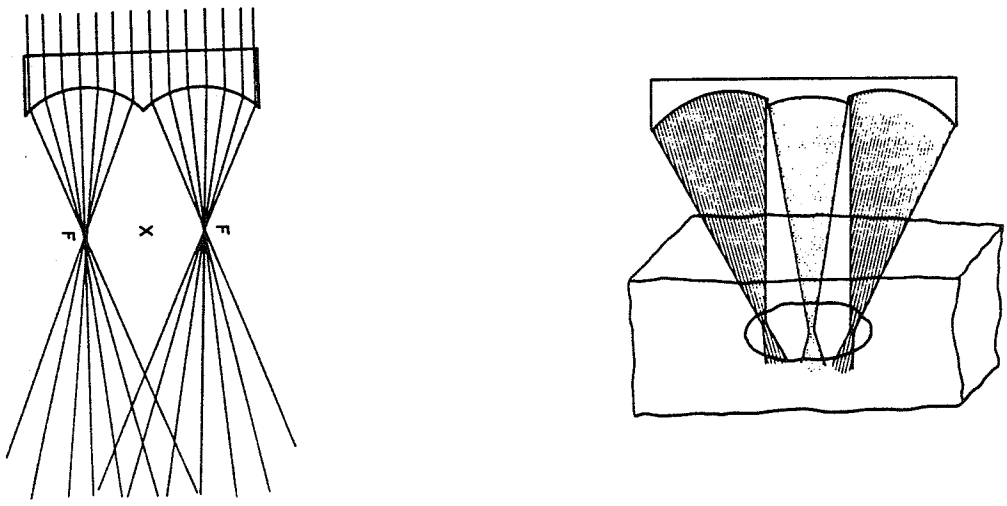

b)

c)

Figure 2.1. a) The geometrical configuration of the Stanford system [18], b) specially designed lens capable of producing annular foci [20], and c) specially designed lens proposed by Lele [19].

or tumor depths. In fact, these transducers are often designed to accommodate tumors with certain geometries at specific depths and their adjustment to different tumor specifications might involve tilting (or even displacing) the transducers and/or increasing (decreasing) the bolus (coupling medium) thickness. These adjustments could increase the complexity of the patient-machine interface and, consequently, a new design is needed to allow the treatment of tumors of different sizes or at different depths.

Dynamic scanning of an intense focal spot offers an alternative to specially designed transducers. An intense focal spot is first produced and then swept along a prescribed path, often around the tumor periphery, by mechanical or electrical means.

Mechanical scanning consists of using a focused transducer to produce an intense focal spot, and the transducer is then translocated by some mechanical arrangement [21]. On the other hand, electrical scanning consists of producing an intense focal spot by adjusting the electrical phase of the signal applied to each element of a phased array (multielement-transducer), The resulting focus is then swept over a prescribed trajectory by simply adjusting the electronic control [16,22].

Both types of scanning require a very short dwell time (time spent at each scanning point) to obtain proper heating of the treated volume while keeping the temperature fluctuation to a minimum level. The requirement of a short dwell time implies the use of a very high intensity ultrasound in order to deliver the proper thermal dose. The use of high intensity ultrasound might increase the risk of undesired nonthermal effects such as cavitation [23]. In addition, mechanical scanning suffers from lack of speed resulting in a relatively crude control of heating patterns and from the need for a cumbersome coupling medium which complicates the patient-machine interface during the treatment.

In the following section, a method is proposed which allows the direct generation of an optimal heating pattern without scanning. Moreover, the method will allow simultaneous focusing at more than one site, a feature that may be used to heat simultaneously different parts of the treatment volume. Establishing the phase and amplitude of the driving signals

required to synthesize the desired heating pattern (annular, elliptical, multiple foci, etc.) is accomplished using simple geometrical considerations. The essence of the method is a direct application of the reciprocity theorem combined with phase and amplitude matching techniques often used in optics [24,25]. Similar methods have been used in the design of microwave applicators [26,27,28]. The method lends itself admirably to many types of transducers including planar and nonplanar arrays [16,29]. First, a mathematical presentation of the method is given. Second, different versions of the method will be presented and advantages and limitations of the technique will be pointed out.

In summary, the method will provide a means of directly synthesizing different heating patterns without scanning, heating simultaneously different parts of a large tumor, and reducing the ultrasound intensity to levels lower than those used in scanning while achieving the required time-averaged intensity gain [30].

2.2 The Field Conjugation Method (FCM)

The essence of the proposed method is an application of the reciprocity theorem combined with the conjugate phase and amplitude matching technique. In general, one assumes a source at the desired focal location and calculates the field produced by the assumed source at the center of each element of the array. Finally, the values of the complex amplitude of the field are conjugated and used as excitation for the different array elements.

To generate multiple foci with different amplitudes, the procedure is repeated for every focus independently, complex amplitudes of the fields are then calculated, multiplied by the appropriate scaling factor, conjugated, and then summed to lead to the final expression necessary for the excitation of each element. The amplitude of each focus is controlled by adjusting the scaling factor associated with that focus.

2.2.1 Formulation of the problem

The synthesis problem considered here is to produce M foci of different amplitudes using a phased array of N elements. As an illustration, Figure 2.2 shows the elements S_1, S_2, ..., S_N arranged along the same line in the source plane. However, the method is not restricted to any geometrical configuration and can be applied to nonplanar arrays as well.

2.2.2 The field conjugation method (FCM)

The method is first presented in general form. A mathematical presentation based on matrix notation is then adopted. The matrix notation, while not essential for the development of the method, will help in adapting the synthesis procedure to the use of digital computers. Furthermore, this same presentation can be used in the formulation of an optimization problem where a desired criterion index (power deposition, intensity gain, etc.) is to be optimized while the excitation signal is constrained to remain within some specified limits. A matrix presentation will prove useful for applying optimization techniques. The FCM can be described as follows:

Step 1: Consider a source at a point P in the focal plane (desired focus) and let it radiate back toward the surface of the array. The source excitation is assumed to be a time-harmonic signal of the form A exp(jωt), where t, ω, and A are the time, the frequency in rad/sec, and a real scaling factor, respectively. However, in a later section, the source excitation signal will be modified by introducing a phasing term to eliminate some undesired hot spots.

Step 2: Compute the field F_{11} at the center of element S_1 in the source plane due to the assumed source at point P. Calculate the fields F_{12}, F_{13},..., F_{1N} at the center of S_2, S_3,...S_N, respectively. An Nx1 vector V_1 is then formed:

$$V_1 = (F_{11} \quad F_{12} \quad \ldots \quad \ldots \quad F_{1N})^T$$

where T is the transpose.

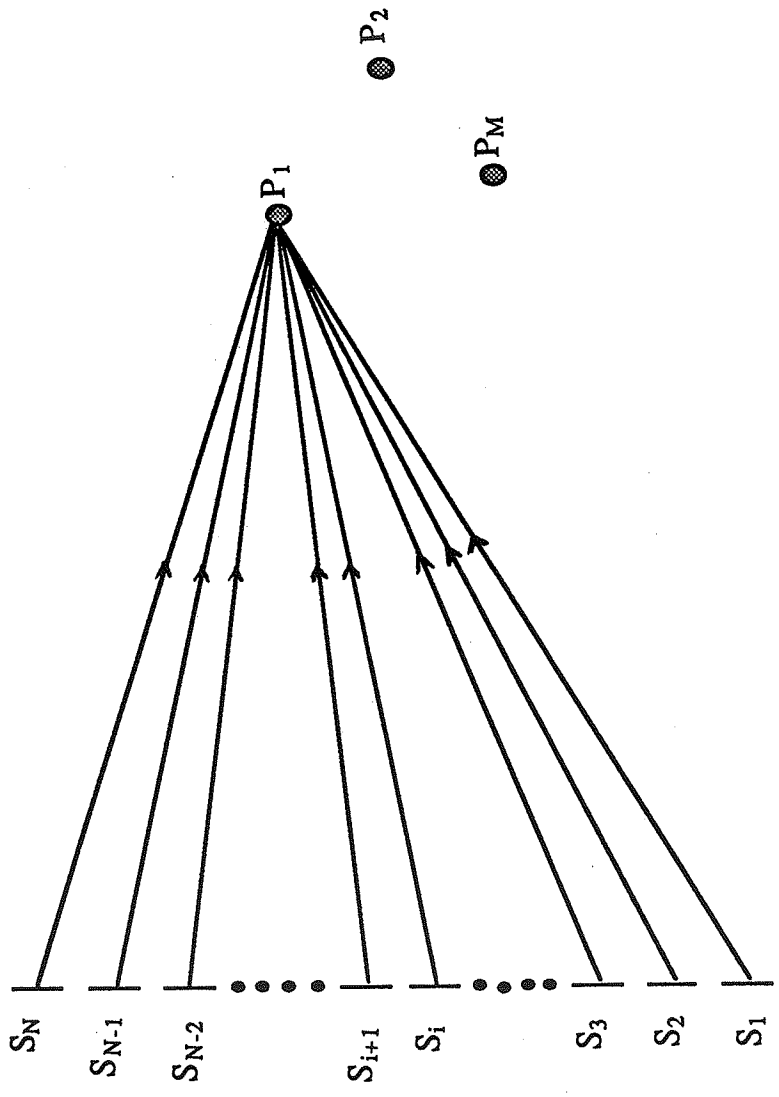

Figure 2.2. A schematic of the field conjugation technique. The assumed sources are designated by P_1, P_2,..., P_M and the array elements are arranged in linear fashion for simplicity.

Step 3: The same procedure (step 2) is then repeated for the different desired foci P_2, P_3,..., P_M and form the vectors V_2, V_3,..., V_M as follows:

$$V_2 = (F_{21} \quad F_{22} \quad \dots \quad \dots \quad F_{2N})^T$$

$$V_3 = (F_{31} \quad F_{32} \quad \dots \quad \dots \quad F_{3N})^T$$

.

.

.

$$V_M = (F_{M1} \quad F_{M2} \quad \dots \quad \dots \quad F_{MN})^T$$

The notation F_{ik} means a complex field at the location S_i due to a source with a harmonic excitation A_k placed at location P_k.

Step 4: The NxM matrix F is then formed .

$$F = \begin{bmatrix} F_{11} & F_{21} & \dots & \dots & F_{M1} \\ F_{12} & F_{22} & \dots & \dots & F_{M2} \\ \dots & \dots & \dots & \dots & \dots \\ \dots & \dots & \dots & \dots & \dots \\ F_{1N} & F_{2N} & \dots & \dots & F_{MN} \end{bmatrix}$$

Step 5: The conjugate matrix F^* is then formed by substituting each component in the matrix F by its conjugate.

$$F^* = \begin{bmatrix} F_{11}^* & F_{21}^* & \dots & \dots & F_{M1}^* \\ F_{12}^* & F_{22}^* & \dots & \dots & F_{M2}^* \\ \dots & \dots & \dots & \dots & \dots \\ \dots & \dots & \dots & \dots & \dots \\ F_{1N}^* & F_{2N}^* & \dots & \dots & F_{MN}^* \end{bmatrix}$$

Step 6: The signal needed to excite each element of the array is then computed by summing the components of the corresponding row of the matrix F^*.

$$I = \begin{bmatrix} I_1 \\ I_2 \\ . \\ . \\ I_N \end{bmatrix} = \begin{bmatrix} \sum_1^M F^*_{i1} \\ \sum_1^M F^*_{i2} \\ . \\ . \\ \sum_1^M F^*_{iN} \end{bmatrix}$$

[I] is the excitation vector where $I_1, I_2, \dots, I_N$ are the complex signals needed to excite the elements $S_1, S_2, \dots, S_N$, respectively.

2.2.3 Direct synthesis of intensity profile patterns

The FCM, like other phasing techniques, can be used to produce an intense focal spot that can be swept along a prescribed trajectory leading to some desired field intensity patterns. However, the ultimate goal of the method is to directly synthesize heating patterns overlaying tumor geometry by direct deposit of ultrasonic energy where it is needed, without scanning. An attractive feature of the FCM is its ability to reconstruct a desired intensity profile by examining the field produced by a "fictitious" source of shape and size similar to those of the desired profile at the center of each array element.

In its very elementary form, the method consists of assuming a source of shape and size similar to those of the intensity profile to be synthesized at the desired location and applying the procedure described in Section 2.2. As an illustration, Figure 2.3a) shows the simultaneous synthesis of an annular ring and an elliptical pattern at a certain distance from the applicator (arbitrary two-dimensional array). A similar pattern can be produced by substituting the spatially continuous assumed source by N discrete point sources appropriately distributed over the contour of the desired pattern. The number of the assumed point sources and their relative spacings are governed by the dimension of the focal spot produced by the array and the size of the desired pattern. Figure 2.3b) illustrates the procedure for the synthesis of a focal ring.

The direct synthesis of heating patterns, like scanning the periphery of a tumor, requires the predetermination of the size, shape, and the location of the tissue volume to be heated. In a clinical situation, this can be accomplished prior to the treatment using an imaging system which could in some cases be a part of the therapeutic system.

2.2.4 The rotating field conjugation method (RFCM)

The synthesis method, presented in the previous section, is characterized by its ease of application which allows the production of a complex field pattern by assuming a source of an appropriate shape. However, the method can lead, in some cases, to particularly strong secondary foci along the axis of symmetry. The formation of these foci is the result of the constructive interference of the acoustic waves along the axis due to the reconstructive nature of the field conjugation method. The method assumes N point sources distributed appropriately over the periphery of the desired ring (see Figure 2.3b)). The N fictitious sources are assumed to vibrate in phase as described in Section 2.2. Moreover, the acoustic path between an arbitrary point on the main axis and any assumed source is the same due to the circular symmetry. This means that the acoustic waves will interfere constructively over the main axis to reconstruct the desired annular pattern.

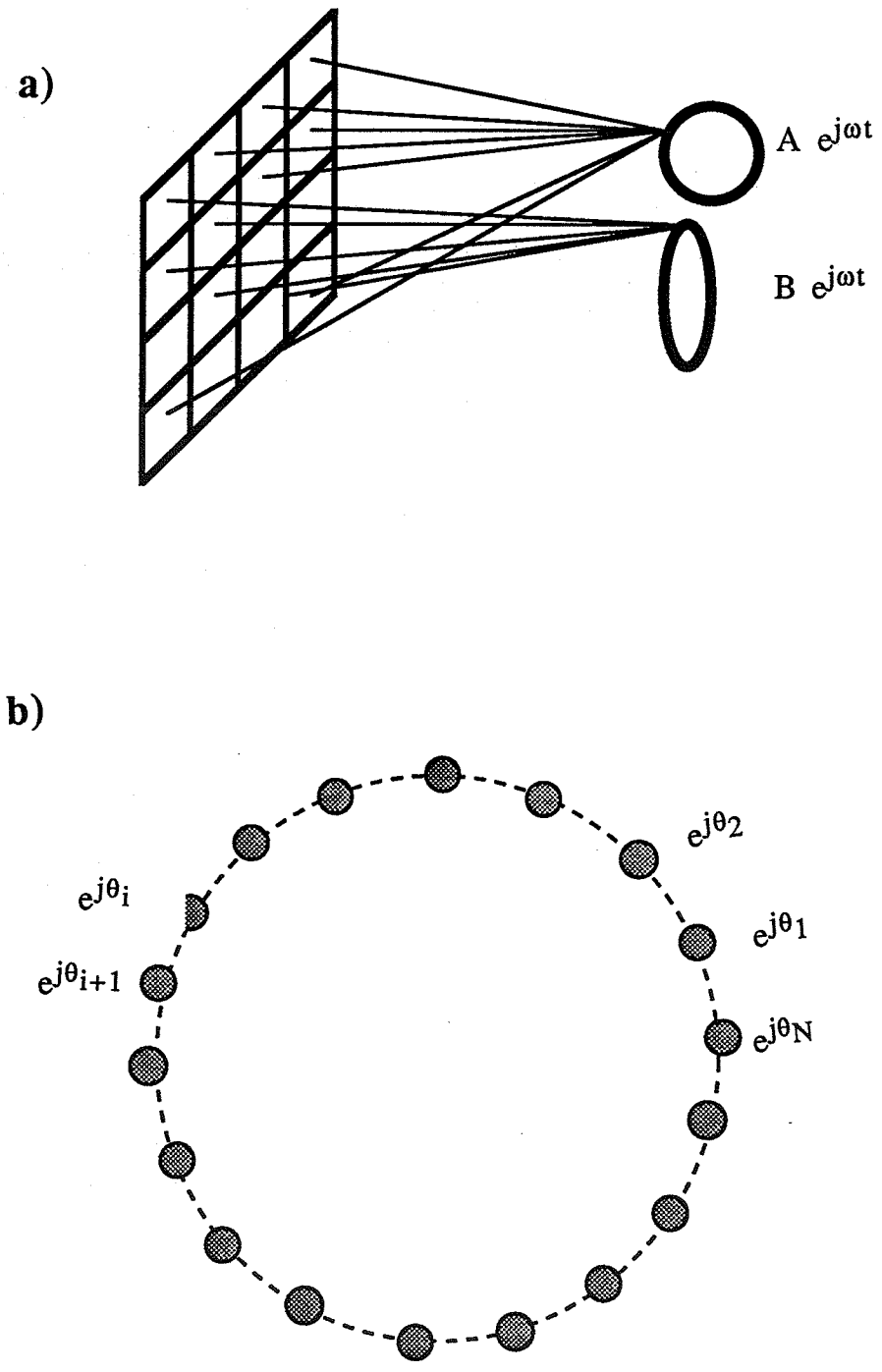

Figure 2.3. Application of the FCM to synthesize different intensity profiles. a) Synthesis of annular and elliptical intensity profiles using spatially continuous shapes and b) synthesis of an annular pattern using N point sources.

This problem can be resolved by introducing an appropriate phasing function to the excitation of each assumed source as will be shown in the following paragraphs. It is demonstrated that the problem of the formation of secondary foci on the axis is completely eliminated in some cases (i.e., annular and disk-shaped patterns). However, the problem is only alleviated in some other cases such as the synthesis of elliptical patterns.

The number of the necessary point sources (or small disk-shaped ones) and their distribution depend on the geometry of the the desired pattern and that of the focal spot produced by the array. It is often appropriate to choose the spacing in such a way that a minimal interference occurs between the individual half power focal spots resulting in the focal plane. This implies that the spacing between assumed sources should be at least of the order of the focal-spot size. An estimate of the number of the required point sources is obtained by dividing the length of the periphery (i.e., $2\pi R$ for an annular ring of radius R) by a length slightly larger than the transverse size of the 3 dB region of the focal spot characteristic of the array. The necessary phasing terms are then calculated by computing the expression of the field resulting on the main axis and forcing its value to zero by choosing the appropriate phase necessary for every vibrating source.

The procedure is illustrated for two cases of interest, annular rings and elliptically shaped patterns. The distributions of the assumed point sources over the periphery of an annular ring of radius R is illustrated in Figure 2.3b). These assumed sources are then excited by signals of the form $\exp j(\omega t+\theta_1)$, $\exp j(\omega t+\theta_2)$,..., $\exp j(\omega t+\theta_N)$ where θ_1, θ_2,..., θ_N are the individual phases to be determined. The calculation of the resulting field, at an arbitrary point q along the main axis, is then performed as follows:

$$P = A \sum_{i=1}^{N} \exp(j\theta_i) \frac{\exp(-jkr_i)}{r_i} \tag{2.1}$$

where r_i is the distance separating the point q and the source i, k is the propagation constant of the medium, and A is a proportionality constant. The time dependency of Eq. (2.1) was dropped for simplicity. The pressure field expression becomes

$$P = A \sum_{i=1}^{N} \exp(j\theta_i) \frac{\exp(-jk\sqrt{R^2+z^2})}{\sqrt{R^2+z^2}} \tag{2.2}$$

where R and z are the distances separating the center of the annular ring from the source i and the point q, respectively. It is clear from above that only θ_i depends on the position of the element and hence, the summation becomes

$$P = A \frac{\exp(-jk\sqrt{R^2+z^2})}{\sqrt{R^2+z^2}} \sum_{i=1}^{N} \exp(j\theta_i) \tag{2.3}$$

By choosing $\theta_i = i\theta_0$ in the above expression, the summation can be performed as follows:

$$P = A \frac{\exp(-jk\sqrt{R^2+z^2})}{\sqrt{R^2+z^2}} \frac{\exp(j\theta_0)-\exp(j(N+1)\theta_0)}{1-\exp(j\theta_0)} \tag{2.4}$$

The technique consists of forcing the field to be zero along the axis by choosing an appropriate θ_0. This condition can be achieved by choosing N $\theta_0 = 2m\pi$ and $\theta_0 \neq 2p\pi$ simultaneously (m and p are integers). Finally, the required phasing angle can be written as $\theta_i = i \frac{2\pi}{N}$ where i and N are the indexes of the assumed source S_i and the total number of sources, respectively.

The above calculation shows that by choosing $\theta_1 = \frac{2\pi}{N}$, $\theta_2 = \frac{4\pi}{N}$,...,$\theta_N = 2\pi$, the secondary foci on the main axis are eliminated. A similar calculation, in the case of elliptically shaped pattern synthesis, can be performed as follows:

$$P = A \sum_{i=1}^{N} \exp(j\theta_0) \frac{\exp(-jkr_i)}{r_i} \tag{2.5}$$

By assuming the ellipse parameters to be a,b and ϕ such that $\frac{x^2}{a^2}+\frac{y^2}{b^2}=1$ and ϕ is the angle between the vector (x,y) and the horizontal axis (see Figure 2.4), then r_i can be expressed as;

$$r_i=\sqrt{a^2\cos^2\phi_i+b^2\sin^2\phi_i+z^2} \tag{2.6}$$

and by considering the trigonometric identity, $\cos^2\phi-\sin^2\phi=\cos 2\phi$, r_i becomes

$$r_i=\sqrt{a^2+b^2+z^2}\sqrt{1+\frac{a^2-b^2}{a^2+b^2+z^2}\cos 2\phi_i} \tag{2.7}$$

and by noticing that $\frac{a^2-b^2}{a^2+b^2+z^2}<<1$, Eq. (2.5) becomes

$$P=A\frac{\exp(-jk\sqrt{a^2+b^2+z^2})}{\sqrt{a^2+b^2+z^2}}\sum_{i=1}^{N}\exp(j\theta_i-jk\frac{a^2-b^2}{2(a^2+b^2+z^2)}\cos 2\phi_i) \tag{2.8}$$

Equation 2.8 is identically zero if $\sum_{m=1}^{N}\exp^{jm\beta}=0$ with $m\beta=\theta_m-k\frac{a^2-b^2}{2(a^2+b^2+z^2)}\cos 2\phi_m$

and by using the result of the circular case, the necessary phase of element m is

$$\theta_m=\frac{2\pi}{N}m+k\frac{a^2-b^2}{2(a^2+b^2+z^2)}\cos 2\phi_m \tag{2.9}$$

Unlike the result reached for the annular case, the resulting expression here depends on z, and hence, it is necessary to specify the depth at which the secondary focus is to be eliminated. In a simulation situation, one needs to determine the field along the axis of the array without the phasing term; then z is chosen to eliminate the highest observed secondary foci along the axis. This technique will be demonstrated in Chapter 4.

2.3 The driving amplitude control required by the FCM

The FCM requires not only a driving phase but also a driving amplitude control for every array element. As an illustration, the phase and the amplitude distributions of the signal needed to excite a point-source linear array of 15 elements are given in Table 2.1.

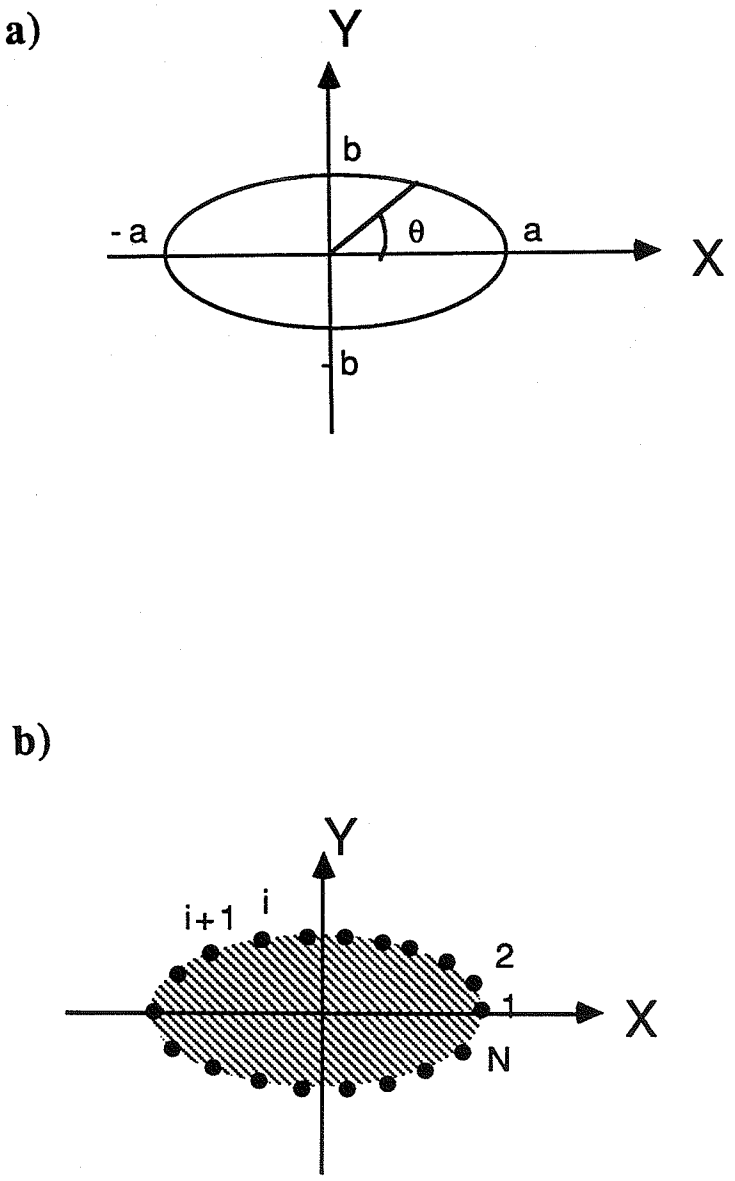

Figure 2.4. Synthesis of an elliptical pattern. a) A schematic of an ellipse and b) geometrical arrangement of the assumed N point sources in the focal plane.

These distributions were obtained by assuming a point source at a point p along the axis of the array as illustrated in Figure 2.5a). The amplitudes were normalized to the maximum amplitude required by the method. The medium is assumed lossless ($\alpha = 0$) for this example.

Table 2.1

Relative Amplitude and Phase Associated with the Pattern of Figure 2.5

Element	Amplitude	Phase in rad
1	0.65	3.21
2	0.71	2.43
3	0.761	1.81
4	0.83	1.21
5	0.89	0.71
6	0.94	0.32
7	0.98	0.08
8	1.00	0.00

The phase and relative amplitude for elements 9, 10,..., 15 are the same as those of elements 7, 6,..., 1 due to the symmetry of the synthesized pattern. Table 2.1 was obtained for d= one wavelength and D= 6d (see Figure 2.5a)). Figure 2.5b) shows the normalized amplitude distribution required for this simple case of synthesis. It can be seen that the required amplitudes are shaded strongly toward the center with relatively low amplitudes toward the edges of the array. The same conclusion can be reached for the case where the beam is steered to an arbitrary point off-axis except that the amplitudes will be shaded strongly toward the nearest point source to the point p' as shown in Figures 2.6a) and b). It is interesting to notice that this kind of shading is commonly used in underwater ultrasonic array design to control the directivity and side lobes, as will be discussed. However, the amount of maximum power that the array can provide is also affected by the amplitude shading and needs to be considered. In the following, the effect of the amplitude shading on

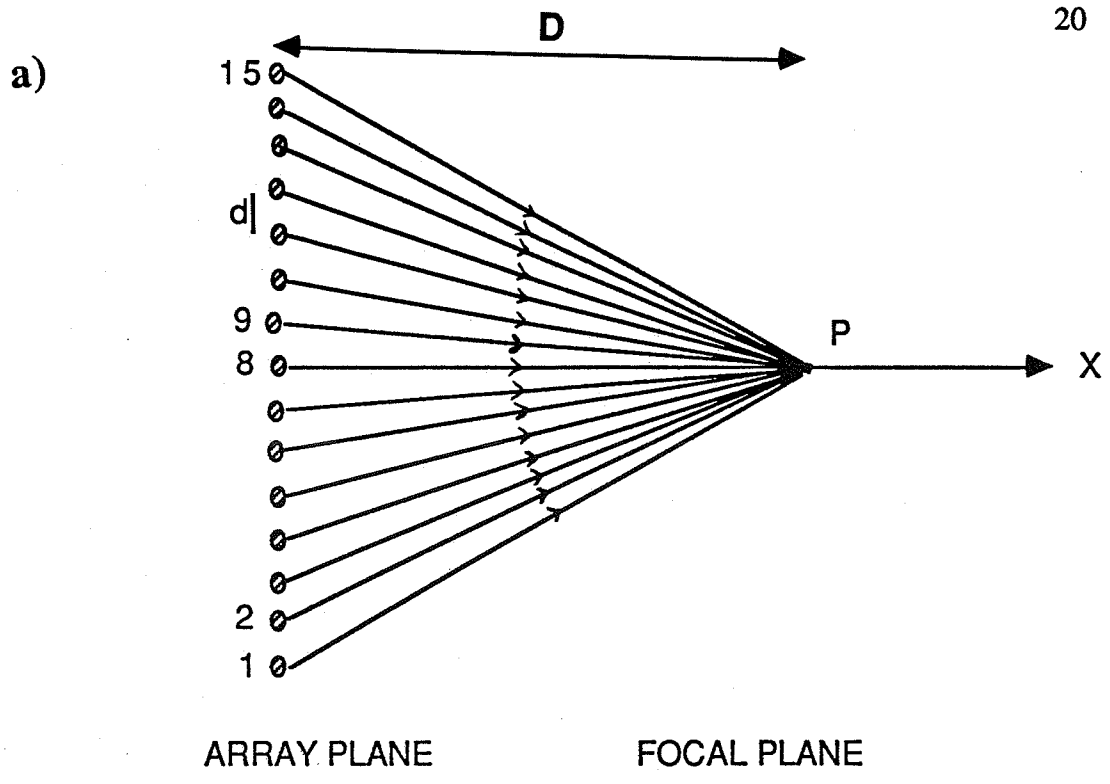

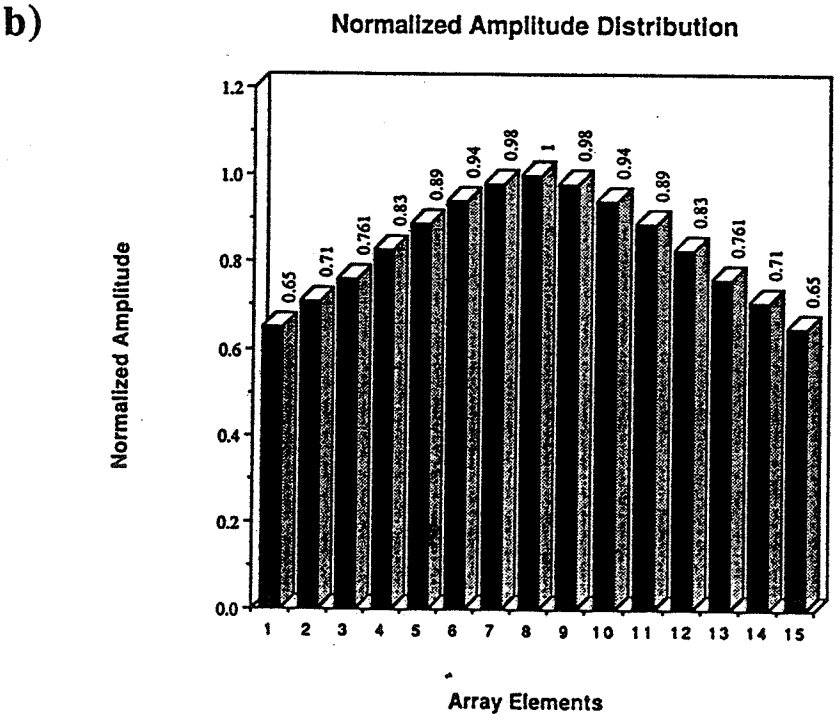

Figure 2.5. The driving amplitude control required by the FCM. a) A linear array of point sources focused along its axis and b) the normalized amplitude distribution of the excitation signal required for the synthesis of a).

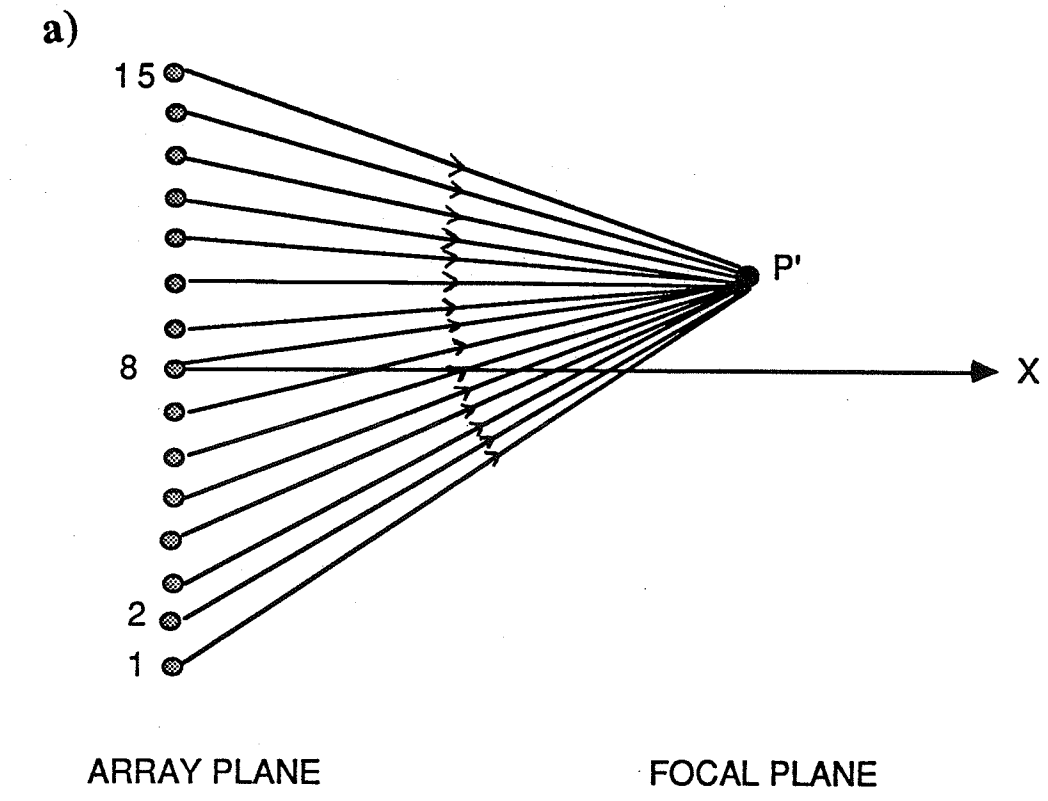

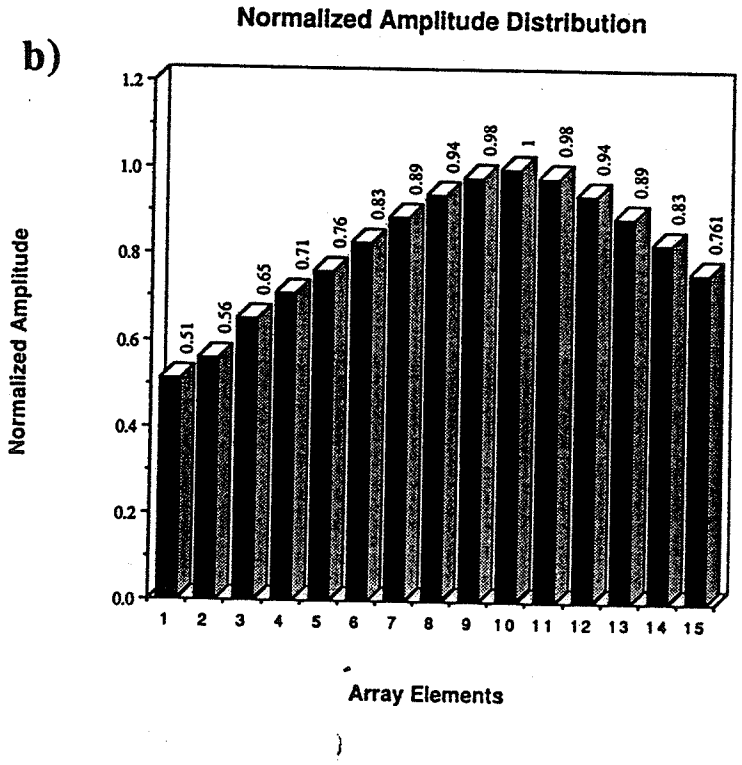

Figure 2.6. The driving amplitude control required by the FCM. a) The array of Fig. 2.5 steered to a point p' off axis and b) the required normalized amplitude distribution.

the directivity and the maximum power available along with some other issues are considered.

2.3.1 Effect of the amplitude shading on the directivity of the array

Amplitude shading has been used widely to achieve some degree of control over the patterns produced by sonar arrays. The shading consists of adjusting the amplitude of the received signal to provide maximum sensitivity [31]. In most cases, shading is accomplished with maximum amplitude toward the center and least amplitude toward the outer elements [31,32,33]. As noticed earlier, the FCM results in a similar shading and, consequently, an illustration of the effect of shading on the directivity of the array is attempted in the following paragraphs.

A linear array of point sources with uniform spacing is considered for the demonstration. Although this situation might be too simple to simulate any case of interest, it is believed that the results will provide a better understanding of the effect of shading on the patterns produced by multitransducer applicators. Figure 2.7 illustrates the geometry of the considered array.

The far field approximation of the pattern produced by this array in a direction relative to an arbitrary point q is given by

$$P = P_0 \sum_{i=1}^{2N} u_i \exp(-jk(r \times r_i)) \qquad (2.10)$$

where u_i is the strength of the point source i, r is a unit vector pointing toward the point q, r_i is a vector originating from the center toward the position of the source i, k is the propagation constant of the medium, and x is the cross product. P_0 is a normalization factor to make P equal unity along the axis of maximum pressure (array axis in this example).

In the following, it is assumed that the number of elements is 2N (the case of 2N+1 can be treated similarly) and that $u_1 = u_{2N}$, $u_2 = u_{2N-1}$,..., $u_{N-1} = u_{N+2}$, $u_N = u_{N+1}$. The

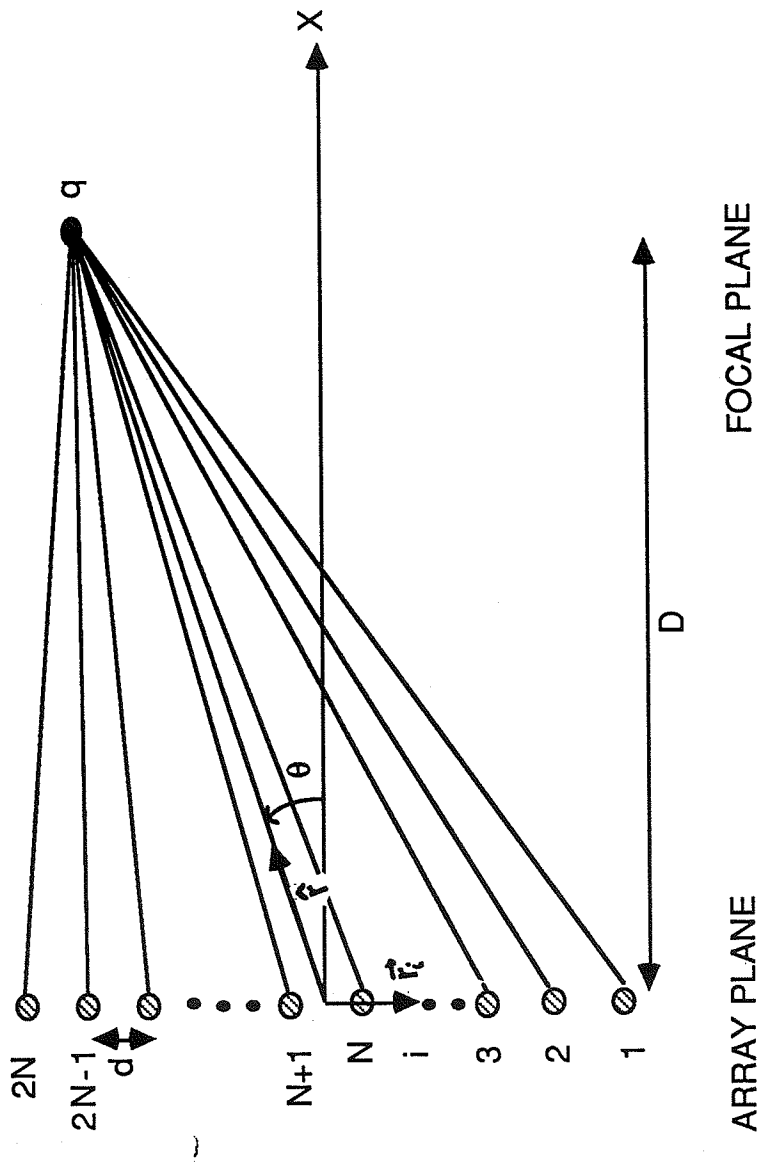

Figure 2.7. A point-source linear array of 2N elements steered to an arbitrary point q in the focal plane.

normalization factor is then found to be $(1/\sum_{1}^{N}2u_i)$ and the expression of the far field pattern becomes

$$P = 2P_0 \sum_{i=1}^{N} u_i \cos[(2i-1)\frac{kd\sin\theta}{2}] \tag{2.11}$$

To illustrate the effect of the amplitude shading on the side lobes, point-source linear arrays of four and ten elements are considered for different weighting functions $(u_1,u_2,...,u_n)$. These two cases were chosen because of the different nature of side lobes as a function of the element number (array length). As could be expected, the number of the side lobes increases with the number of elements, but their relative amplitudes decrease (with respect to the main lobe amplitude). The simulations of the resulting patterns were performed for a uniform source-to-source spacing (0.5 λ).

Different weighting functions (amplitude shading) were assumed for the simulations. Figure 2.8 illustrates the resulting patterns for shading function (2, 1, 1, 2), (1, 1, 1, 1), (1, 2, 2, 1), and (1, 4, 4, 1). It is observed that an increase or decrease in the amplitude of side lobes may result depending on the scheme used for amplitude shading. If shading is accomplished with maximum amplitude toward the array edges, the relative amplitude of the side lobes is increased (compared to the nonshading case) as illustrated in Figure 2.8. On the other hand, shading with maximum amplitude toward the center results in suppressing the side lobes while widening the main lobe. Similar observations result from simulating the case of a 10-point-source linear array as shown in Figure 2.9. By comparing the different patterns with that resulting from the nonshading case (1, 1, 1, 1, 1), it is clear that the particular amplitude shading required by the FCM may help suppress some side lobes. However, grating lobes (of amplitude equivalent to that of the main lobe) seem to be insensitive to amplitude shading, as illustrated in Figure 2.10, which is obtained for a uniform spacing of a full wavelength.

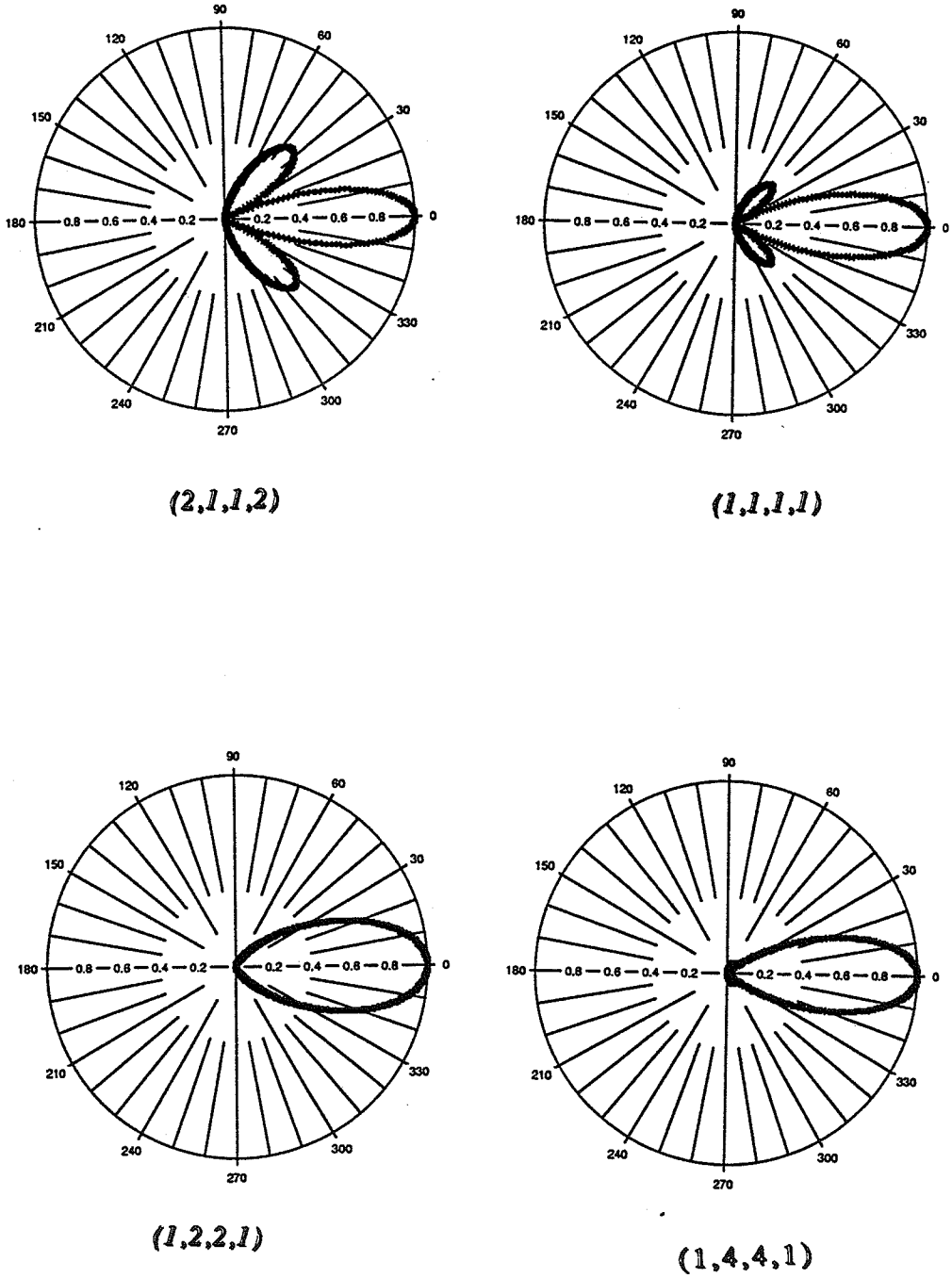

Figure 2.8. Effect of the amplitude shading on side lobes. The assumed linear array consists of 4 elements of a strength function (u_1,u_2,u_3,u_4). Different patterns each associated with a strength function as shown.

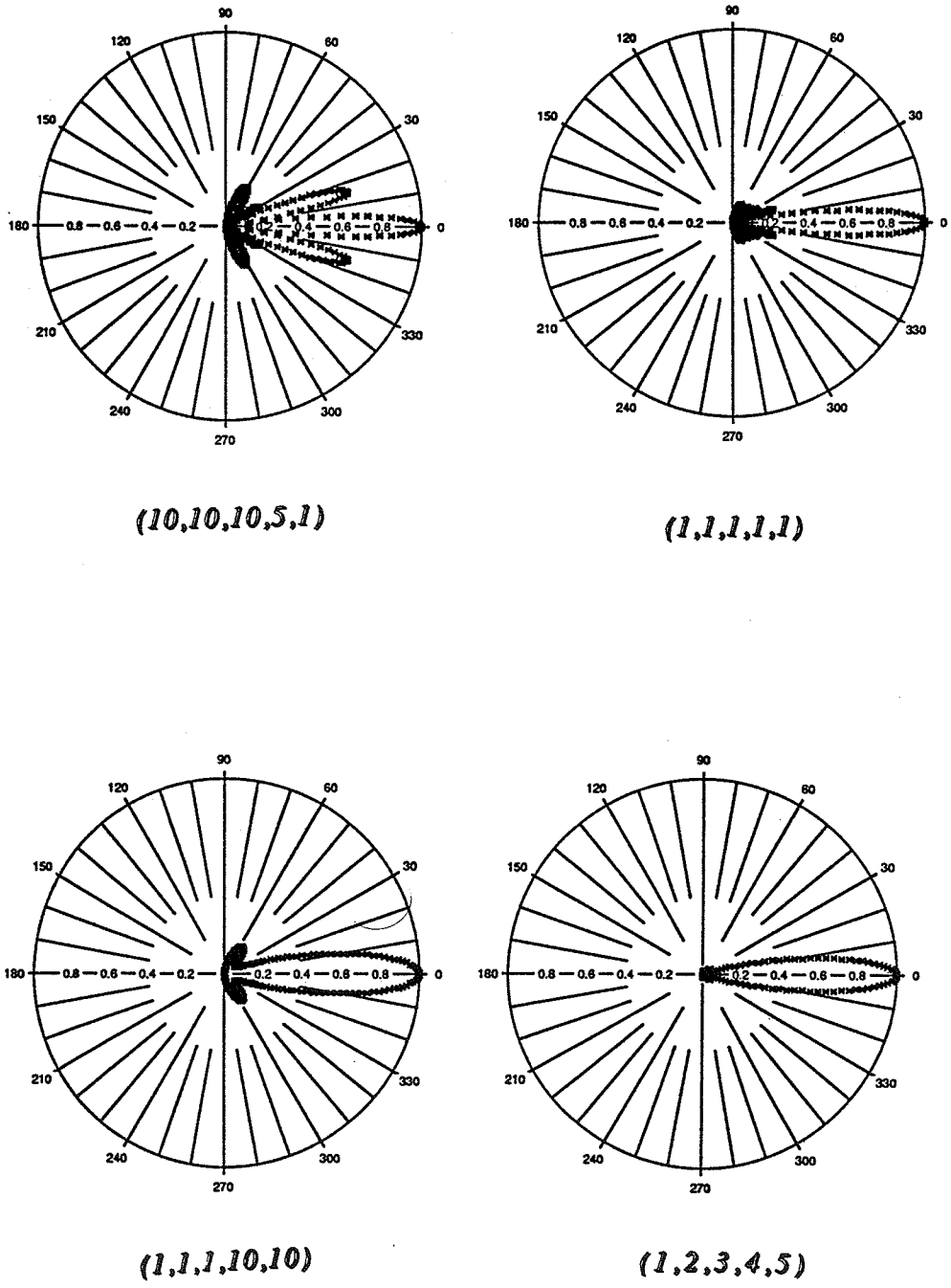

Figure 2.9. Effect of the amplitude shading on side lobes. A point-source linear array of 10 elements is used. The elements are symmetrical with respect to the axis and hence, the strength function is of the form (u_1,u_2,u_3,u_4,u_5). Different patterns each associated with a strength function are illustrated.

a)

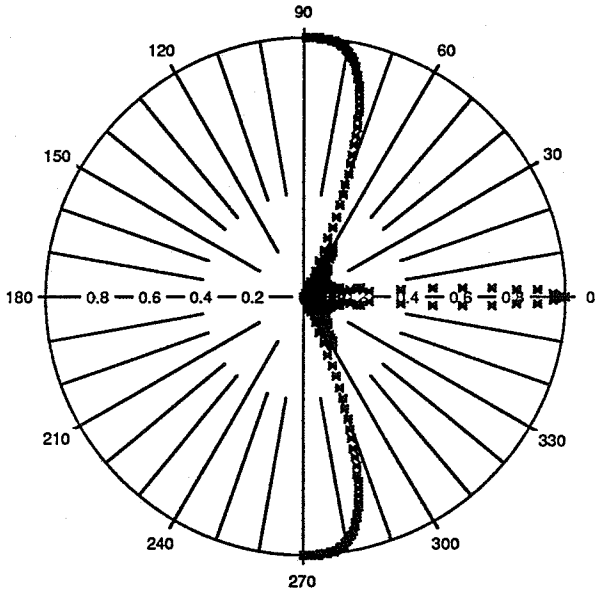

b)

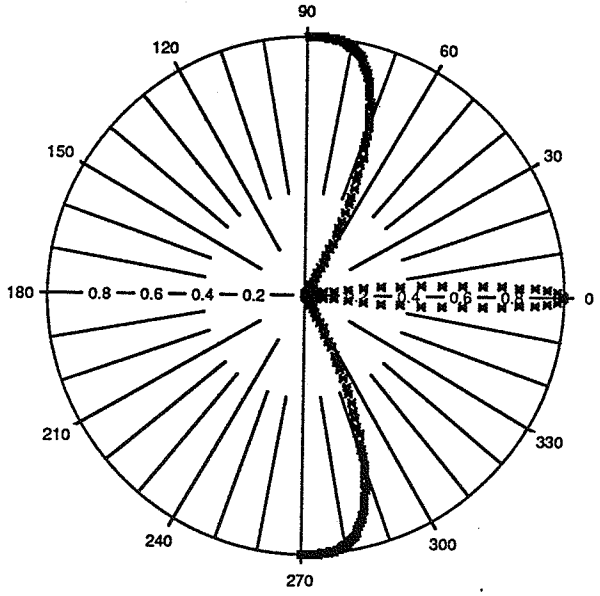

Figure 2.10. Effect of the amplitude shading on side lobes. a) Pattern associated with a nonshaded case and b) pattern associated with a shaded case.

2.3.2 Effect of the amplitude shading on the maximum power produced by the array

The power delivered by a vibrating source is proportional to the square of its surface velocity and, consequently, it is assumed that the maximum power that can be extracted from an array is achieved if each element is vibrating at its maximum velocity tolerable by the transducer material. This observation indicates that due to the amplitude shading of the FCM, the resulting power is always less than that which would have resulted under the assumption of uniform excitation amplitude.

Figure 2.11a) shows the normalized driving amplitude distribution resulting when the FCM was used to synthesize a focal spot along the axis of a 20-element concentric-ring applicator. The analysis of the concentric-ring array is presented in Chapter 3, and Figure 2.11 will be subject to a deeper analysis at that point. It is obvious from Figure 2.11a) that while some elements are excited with relatively high amplitude signals (i.e., elements 1,2,...,7), other elements are merely vibrating with relatively low amplitudes (i.e., elements 15,16,...,20). This amplitude distribution influences the array maximum power capability as some elements will be delivering their maximum power while others are only delivering a fraction of it. For the sake of example, the annular elements of the concentric-ring array are assumed to be of equal effective surface (variable element widths).

The effect of the amplitude shading on the array power can be measured by defining a parameter to characterize each driving amplitude distribution. A simple parameter can be obtained by summing the squares of all normalized amplitudes and dividing the resulting sum by the number of elements. The resulting parameter will be called the " amplitude shading factor" and is actually an indication of the relative average power produced, when the FCM is used, versus that which would have resulted from a uniform amplitude excitation. The amplitude shading factor derived in this section assumes equal area elements. However, a more precise definition will be given in Chapter 3 to account for the cases of elements with different effective surface areas as well. The definition given in Chapter 3 will be slightly different and will be adopted for the remainder of the thesis.

a)

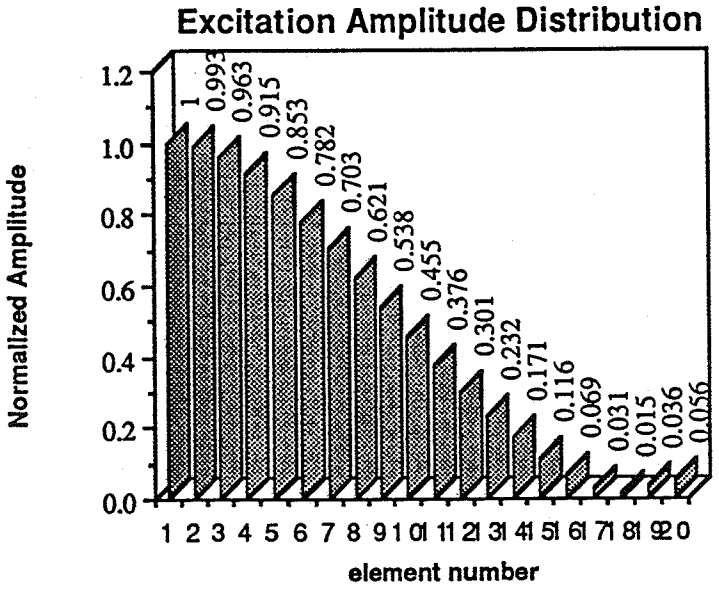

b)

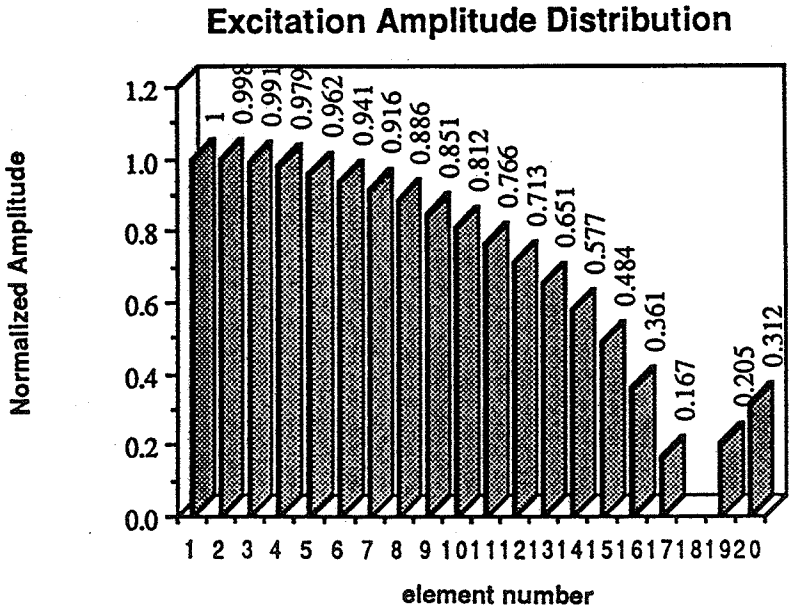

Figure 2.11. Effect of amplitude shading on the maximum power produced by an array. a) Amplitude distribution of the excitation signal as required by the FCM and b) a logarithmically scaled amplitude distribution.

The amplitude shading factor relative to the distribution shown in Figure 2.11a) was found to be 0.337, which might be low for some practical applications. However, it is possible in some cases to improve the amplitude shading factor by modifying the scaling of the amplitude distribution. In some cases, one needs to shorten the dynamical range between the different amplitudes while keeping the general behavior of the distribution close to the original one. One possible approach is to logarithmically scale all amplitudes after dividing them by the lowest amplitude of the original distribution. The division is meant to avoid negative numbers that arise if the logarithm of numbers smaller than unity is attempted. The resulting numbers are then normalized to their maximum and used as driving amplitudes. Figure 2.11b) shows the normalized amplitude distribution resulting from the application of this procedure to the distribution shown in Figure 2.11a). The amplitude shading factor for this logarithmic scaled distribution is found to be 0.61 compared to 0.337 obtained above. This technique will be extensively used in the following chapters. In some simple cases such as simple focusing (point or diffuse focus), it is also possible to drive the array with constant amplitude control while using only the phase control resulting from the FCM as will be shown in Chapter 4.

As will be shown in Chapters 3 and 4, the amplitude shading will prove useful in alleviating the problems associated with the secondary foci formation beyond the focal plane. In particular, for extreme cases where masking the outer elements of the array is proposed [17], the FCM seems to lead to a better power deposition pattern as demonstrated in Chapter 3.

2.4. Conclusions

The field conjugation method was proposed as a means of directly synthesizing the more diffuse intensity profiles without scanning. In other cases where scanning is necessary, the multiple focusing feature of the FCM could potentially simplify scanning by

reducing the number of scan points and/or lowering the focal intensity which is often a concern in scanning techniques.

The method can be used to synthesize very complicated intensity profiles which might be used in hyperthermia, imaging and other applications as well. Although the driving amplitude control might appear as an added complexity to already complicated electronics associated with phase control, the required hardware is essentially the same except for the addition of a digital counter, as will be illustrated in Chapter 7.

CHAPTER 3

ANALYSIS AND DESIGN OF A CONCENTRIC-RING ARRAY

3.1 Introduction

Many ultrasonic systems currently in clinical use employ a single large aperture focused transducer. The focal spot produced by this transducer is too small to heat even the smallest tumor; hence, it is translocated over a desired trajectory (often around the tumor periphery) by some mechanical arrangement. The disadvantages of this technique were mentioned earlier. Systems using multiple transducers arranged in a certain geometrical fashion have also been reported. These systems are based on the use of the overlapping ultrasonic beams which can be controlled by positioning the individual transducers. However, those systems are cumbersome and require a large acoustical window. Moreover, excessive pain can result and often lead to a premature termination of the treatment [18,34]. This problem can be attributed in large part to the absence of the ability to precisely control or modify the power deposition pattern during the treatment. Heating of bone distal to the tumor is a particularly difficult problem which can limit the treatment.

A potential alternative is the use of ultrasonic phased arrays in which the control is mainly electronic and can be built remotely from the applicator allowing a simpler patient-machine interface. Moreover, the associated sophistication in electronics and transducer array configuration should permit more precise control of the heating pattern, and would allow modification of the pattern during treatment, without the need to mechanically move the applicator.

A disadvantage of 2-D phased arrays technology is the need for a large number of transducer elements which increases the complexity of the associated electronic control circuitry [35]. Although this may no longer be a severe limitation due to advances in microelectronics and power amplifier design, it is always preferable to minimize the number

of array elements. In this chapter, the concentric ring array (CRA) is analyzed and the synthesis of different field patterns is simulated using the field conjugation method of Chapter 2. Because of its circular symmetry, the CRA does not require a large number of elements. Moreover, this array is chosen because of its ability to produce 3-D volume heating at different depths. Conventional focusing (intense focal spot) as well as annular intensity profiles are synthesized. The synthesis of multiple foci, conventional and annular, is demonstrated. The advantages and disadvantages of the method are discussed and compared to those of other techniques. Finally, a method based on a simple mechanical scanning of multiple conventional foci (on the main axis) is proposed as a means of heating small and moderate sized tumors deep in the body. The possibility of heating the back and the front of the tumor simultaneously is also demonstrated through computer simulations.

3.2 Geometrical Configuration of the Array

A concentric-ring applicator has been chosen as one array configuration for further study because it allows 3-D volume focusing of the acoustic power at variable depths. Moreover, this configuration is expected to produce circular heating patterns of different diameters simply by adjusting the amplitude and the phase of the driving signal.

Two concentric-ring configurations with the same active surface area and the same number of elements are investigated. The goal is to choose the most appropriate one for simulations and, ultimately, for implementation. In what follows, an applicator diameter of 12 cm is considered for simulations. The applicator size has been chosen to ensure the delivery of adequate acoustic power (more than 350 watts) [36,37] while being within the limits imposed by the acoustical window available for ultrasonic use in the body. It is also desired to keep the number of annular elements as low as possible to reduce the cost of associated phasing and amplifier electronics. For the sake of simplicity of analysis, the small gap between adjacent annular elements will be neglected and the whole surface of the applicator will be considered active. The two configurations under investigation are the

concentric-ring array with a constant-electrode surface area and that with a constant-electrode width.

3.2.1 The equal surface area element array

In this configuration, the effective surface area of every annular element is kept the same. Figure 3.1 illustrates the configuration of the array. The elements S_1, S_2,. , S_N are of the same active surface S, and d_1, d_2,. , d_N are the widths of the elements S_1, S_2,. ., S_N, respectively. It is noticed that the outermost elements are considerably thinner than the innermost ones. This is due to the fact that, in this configuration, the annular element width is inversely proportional to the radius.

The acoustical power extracted from a piezoelectric element is proportional to its active surface and hence, every element will deliver the same acoustical power. Because the widths d_1, d_2,. ,d_N are all different for this geometry, the width-to-thickness ratio of each ceramic element will be different and, consequently, a different operating frequency is needed for each electrode. This could significantly increase the cost of the driving electronics.

Another drawback of this configuration is the need for a very large number of annular elements to achieve annular focusing. This is due to the large width of the innermost elements, compared to the outermost ones, which cannot be steered easily by adjusting the driving phase. Thus, the innermost element widths need to be kept small enough ($<\lambda$) to achieve focusing. The requirement of small width innermost elements implies the division of the applicator into very small equal areas and, consequently, a large number of elements.

As an illustration, a 12 cm diameter applicator is considered. Twenty annular elements, each of a surface area of 5.65 cm^2, are assumed. For the sake of simplicity, the spacing between adjacent elements is neglected and the total surface was simply divided by the number of annular elements. The widths of some of the resulting outer and innermost annular elements are given in Table 3.1. It should be noticed that, while the outermost element width (d_{20}) is 2.5 mm, the innermost element width (d_1) is 13.5 mm. For an

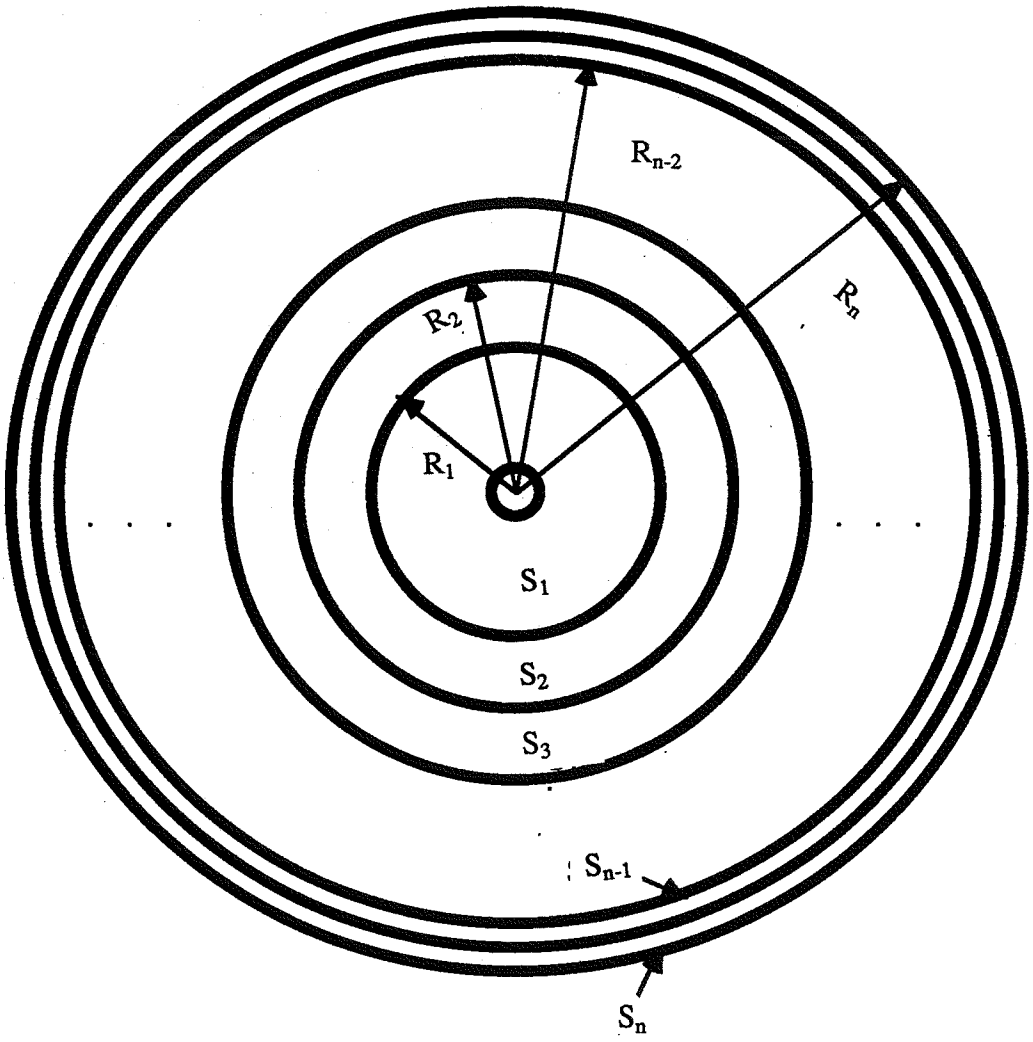

Figure 3.1. Geometrical configuration of a constant area per element concentric-ring array.

Table 3.1.
Outer and Innermost Electrodes Widths for 20-Element Array

innermost electrodes	electrode width in mm	outermost electrodes	electrode width in mm
1	13.45	16	1.77
2	5.60	17	1.70
3	4.40	18	1.65
4	3.70	19	1.60
5	3.20	20	1.50

Table 3.2.
Outer and Innermost Electrodes Width for an 80-Element Array

innermost electrodes	electrode width in mm	outermost electrodes	electrode width in mm
1	6.60	76	0.39
2	2.75	77	0.38
3	2.13	78	0.38
4	1.80	79	0.38
5	1.61	80	0.37

operating frequency of 500 kHz and assuming a sound velocity of 1500 m/s (in tissues), some of the innermost elements are much wider than the wavelength in the medium. Because of these wide elements, steering the sound beam to the desired focal location, by assuming a constant driving phase over the wide electrode, will prove very difficult. Figure 3.2 shows the normalized intensity along a longitudinal axis passing through the focus when synthesizing an annular ring of 30 mm radius at 80 mm depth. This intensity pattern demonstrates that no focus is achieved at the desired location (z=80 mm). However, when the number of elements is increased to 80 (surface area is decreased to 1.41 cm^2 for each element), focusing at the desired location is achieved as demonstrated in Figure 3.3. The widths of the annular electrodes are given in Table 3.2.

It is obvious that reducing the widths of the innermost elements, while resulting in better focusing, leads to a higher number of electrodes and to extremely thin outermost elements which might be impractical for implementation (see Table 3.2). Due to these major drawbacks, no further attention is given to this configuration and the investigation will use the configuration of the equal width element array.

3.2.2 Equal width element array

In this configuration, the width of each annular electrode is kept the same, i.e., $d_1 = d_2 = d_3 = \ldots = d_n$. Figure 3.4 illustrates the geometry of the applicator. As mentioned earlier, the step between adjacent elements is neglected and the center-to-center spacing is considered to be equal to the width of a single element.

The advantage of this configuration is that the width-to-thickness ratio is the same for all annular elements. Therefore, the same resonance frequency is used to drive all electrodes. Moreover, the number of elements can be kept reasonably small to reduce the complexity of the associated electronics. Finally, the realization of such a configuration is simplified since it does not require cutting annular elements of extremely small widths.

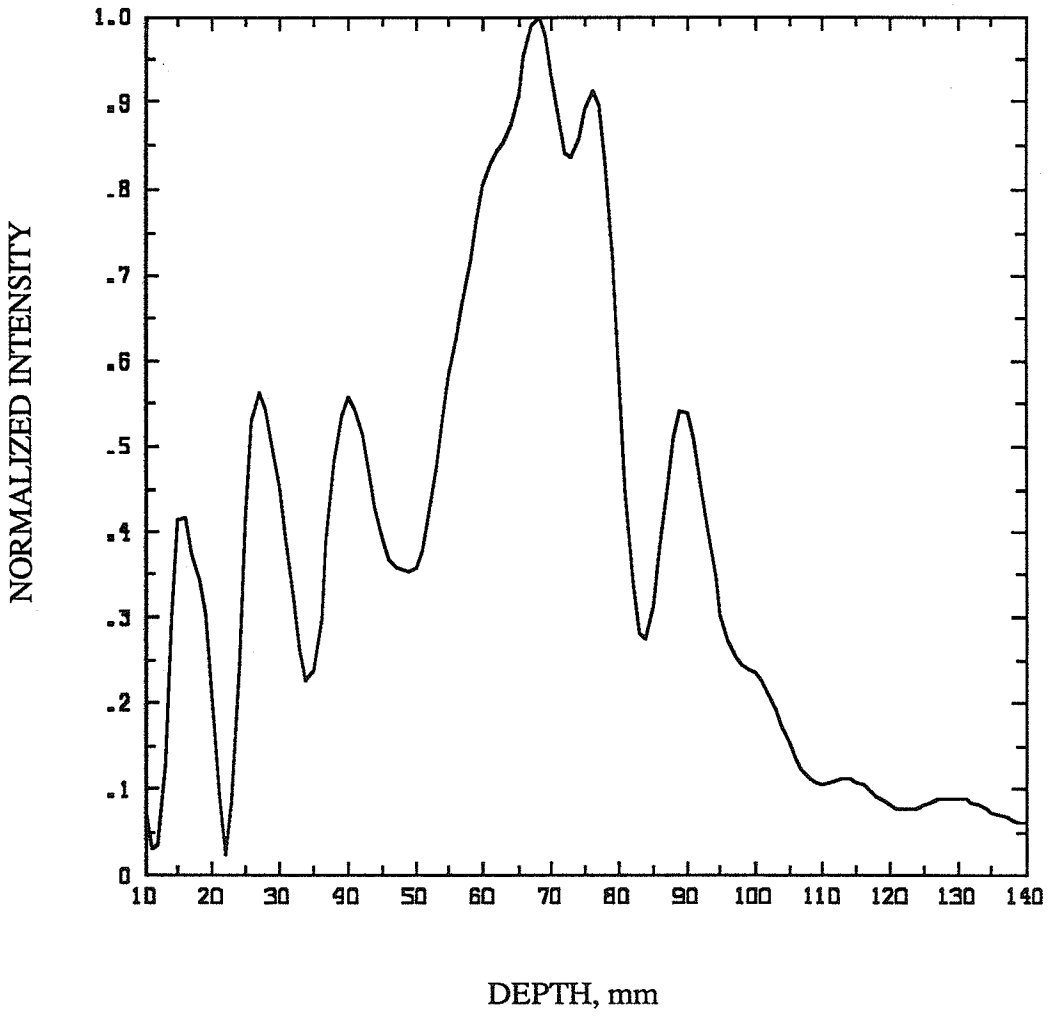

Figure 3.2. Relative field intensity of a constant-electrode surface CRA versus z position. The pattern resulted from attempting to focus the array at (o,o,80) along the axis. The number of elements is 20.

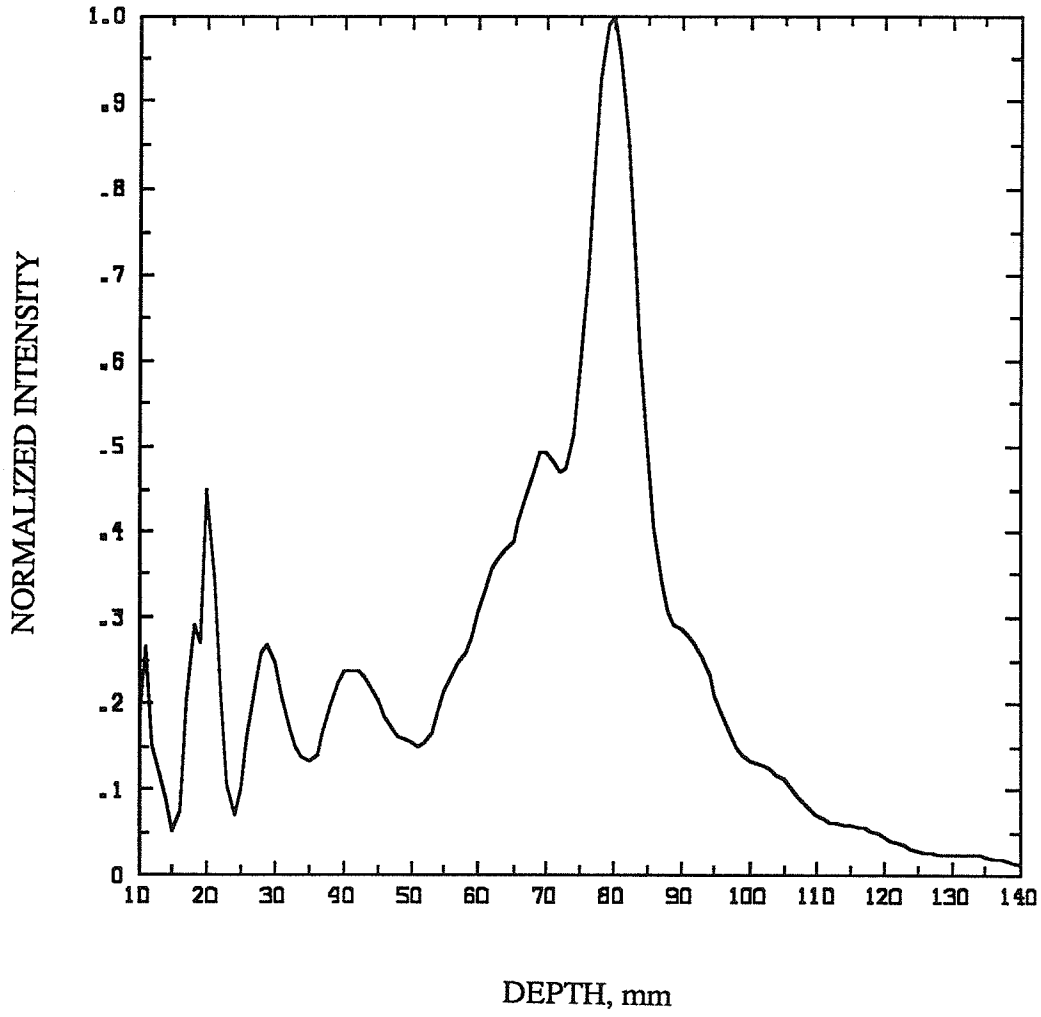

Figure 3.3. Relative field intensity resulting from increasing the number of elements of Fig. 3.2 to 80. Intensities are normalized to that of the focus.

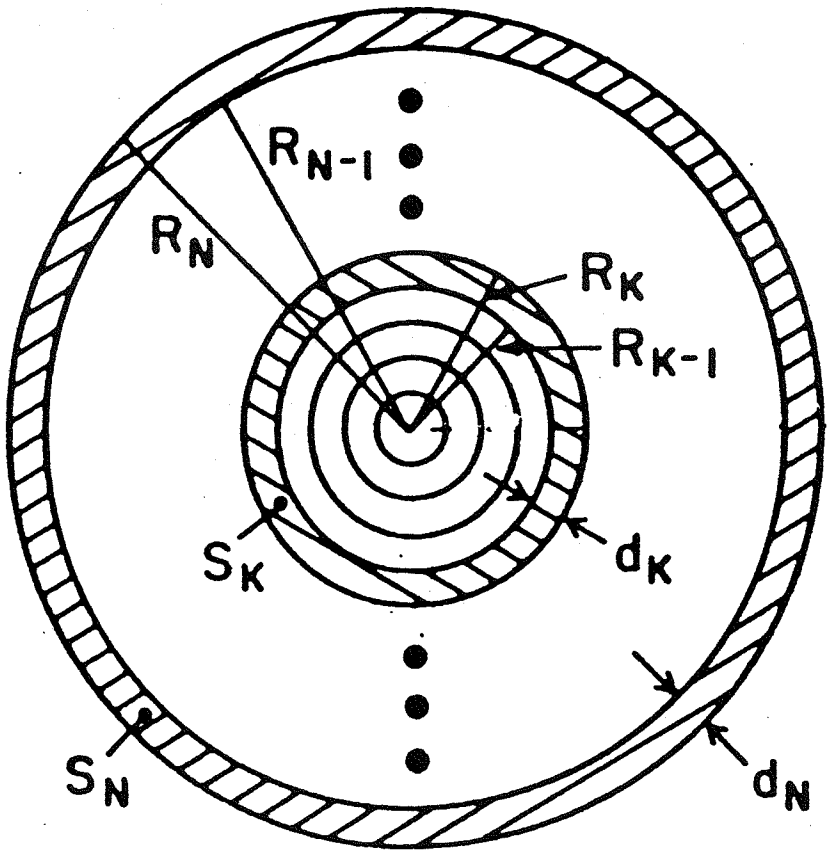

Figure 3.4. Geometrical configuration of an equal-width element concentric-ring array.

As a comparison, the normalized intensity as a function of the depth along the axis of the focus (R=30 mm) is shown in Figure 3.5. The pattern is obtained for the 12 cm diameter applicator divided into 20 annular elements, each of a 3 mm width. In conclusion, this configuration is chosen for further study and for application of the FCM in the following sections.

3.3 Modeling of the Acoustic Field

The Sommerfield-Rayleigh diffraction integral can be evaluated numerically to obtain the pressure field, due to the array, at an arbitrary point in space. This integral can be handled in a straightforward manner as a double summation in cylindrical coordinates. However, because of the rapid change in the phase term exp(jkr), the summation increment needs to be very small and the computation time increases accordingly. To achieve the calculation in a reasonable computation time, the method of equidistant areas described in [38] is modified for the calculation of the field produced by a CRA. The advantage of the method is the transformation of the double integral into a simple one that can be handled easily by digital computers. A summary of the method is given below.

The field produced by the CRA at an arbitrary point P is the sum of the contributions of all annular elements computed at P. A complex surface velocity u_i is associated with the the annular element i. The field due to the element i is then given by

$$P = \frac{j\rho ck}{2\pi} \sum_{i=1}^{N} \int_{s_i} u_i \frac{e^{jKr_i}}{r_i} ds_i \qquad (3.1)$$

where N is the number of the annular elements, ds_i and s_i are the incremental and the total surface areas, respectively. Also, r_i is the distance between the element ds_i and the point where the field is to be evaluated. The surface velocity is assumed uniform over the annular

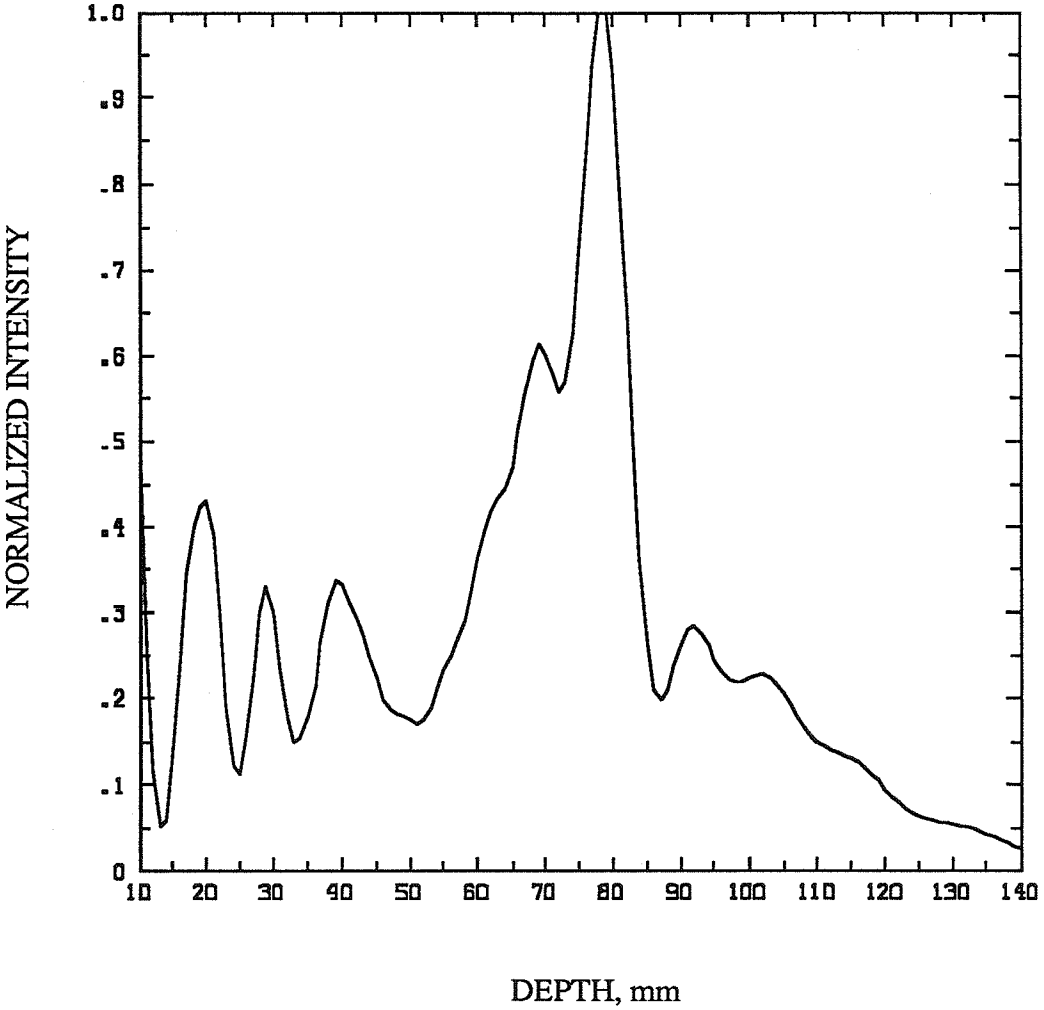

Figure 3.5. Normalized field intensity versus z position resulting from focusing a 20 equal-width element array at point (0,0,80).

element surface, and the problem is that of calculating a surface integral as suggested by Eq. (3.1).

In the above integral, the propagation constant K is assumed complex to account for medium attenuation ($K= k+j\alpha$). To transform the double integral into a simple one, the incremental area is taken as the area over which r_i is sensibly the same. This incremental area is determined by projecting the point P onto the plane of annular element surface and, using geometrical concepts, to evaluate the equidistant areas. To illustrate this, an annular element of inner and outer radii R_1 and R_2 is considered . It is desired to evaluate the field at point P as illustrated in Figure 3.6a) where the point P is projected on P', situated in the plane of the transducer. The equidistant areas are then determined as the intersection between the annular element surface and all the annular strips centered at P' as illustrated in Figure 3.6b).

It is obvious from the illustration that the number of incremental areas (equidistant areas) depends on the width of the annular strips and, hence, the precision of the method can be improved by making the strip width very small. However, the choice of the strip width should be a trade-off between the required accuracy and the computation time. Finally, the double integral is transformed to a simple one given by

$$P_i = \sum_{m=1}^{M} \Delta A_m \frac{\exp(jkr_m)}{r_m} \tag{3.2}$$

where ΔA_m is the area common to the electrode and the annular strip m, r_m is the distance between the point P and the mth annular strip, and M is the total number of annular strips needed to cover the whole electrode surface.

Once the expression P_i is computed for all annular electrodes (i=1, 2, 3,..., N), then the total pressure due to the array is handled as a simple sum. The final expression is given by

$$P = \frac{j\rho ck}{2\pi} \sum_{i=1}^{N} P_i \tag{3.3}$$

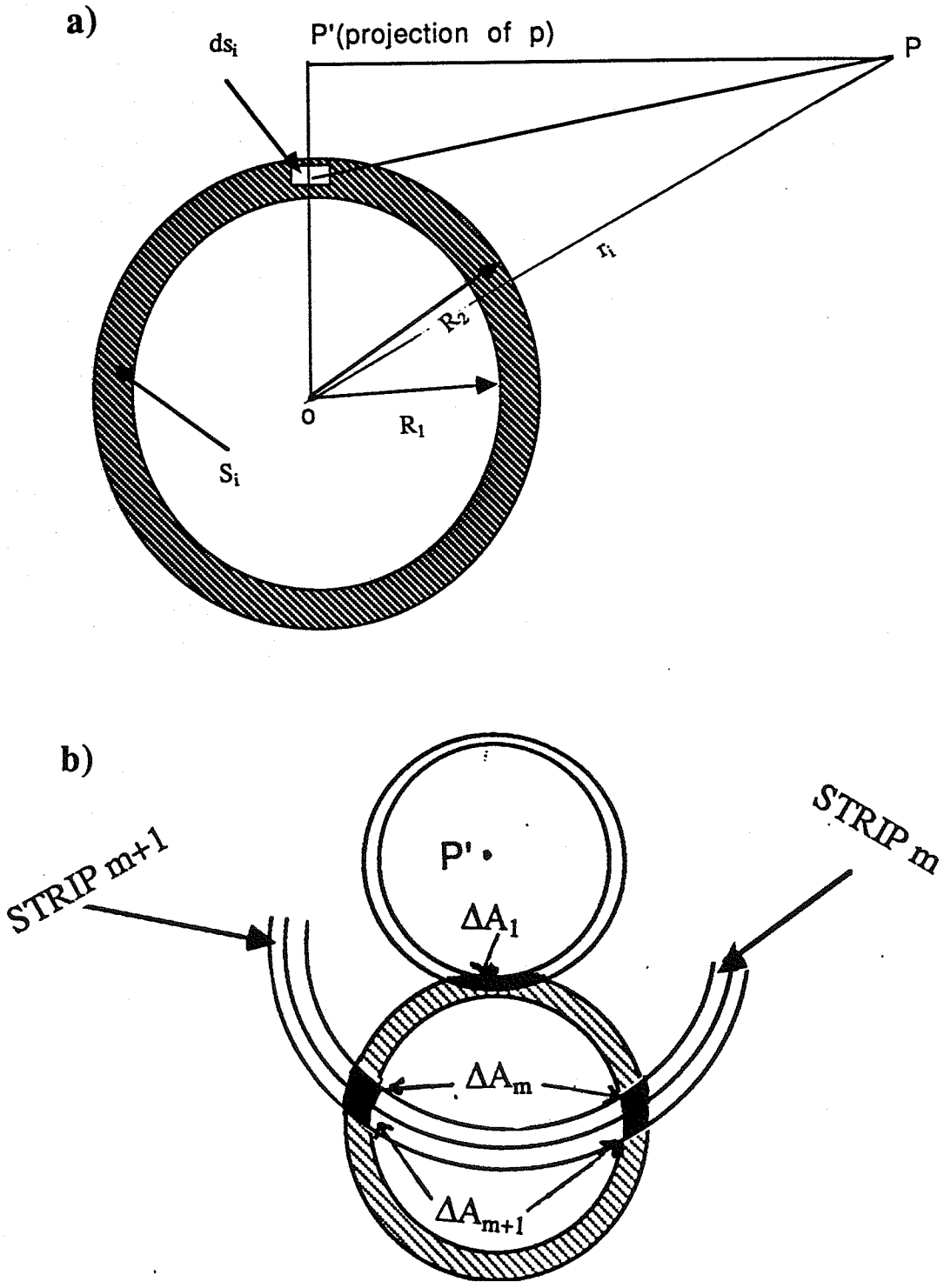

Figure 3.6. Equidistant-areas method. a) A schematic used for the calculation of the pressure field at point P due to an annular ring source and b) determination of the incremental areas.

It is clear that the accuracy of the method depends essentially on the width of the considered annular strips. To choose an appropriate width, our calculations were compared to those obtained by Zemanek for the case of a disk transducer [39]. This case was simulated by considering all electrodes vibrating with the same complex velocity, and the results showed perfect agreement for increments on the order of 1/8 wavelength.

3.4 Synthesis Using the FCM

The general approach consists of assuming a source of annular shape at the desired location, the field due to this source being then computed at the midwidth point of each annular element. Finally, these values are conjugated and used as excitation signals to the corresponding electrodes. However, it is sometimes necessary to modify the procedure slightly to optimize the desired pattern (i.e., elimination of hot spots, etc.). These modifications often deal with the nature of the assumed source and merely require the modification of the software to obtain different heating patterns.

In this section, the general approach is first presented, simulations of some heating patterns obtained by this approach are then given, and a comparison with some existing methods is then discussed.

3.4.1 Synthesis of annular heating patterns using the FCM

An annular source is first assumed at the desired focal plane. The field due to this source is then calculated at the midwidth point of each annular array element. These values are conjugated and the resulting complex expressions are used as excitation signals to the corresponding array elements. Figure 3.7 illustrates the configuration of the assumed source with respect to the array.

This method can be used to synthesize single and multiple annular heating patterns. The annular pattern obtained by assuming a ring of a 40 mm radius at an 80 mm depth is illustrated in Figures 3.8 and 3.9. Figure 3.8 is the surface plot of the patterns resulting in

a) CONCENTRIC-RING ARRAY

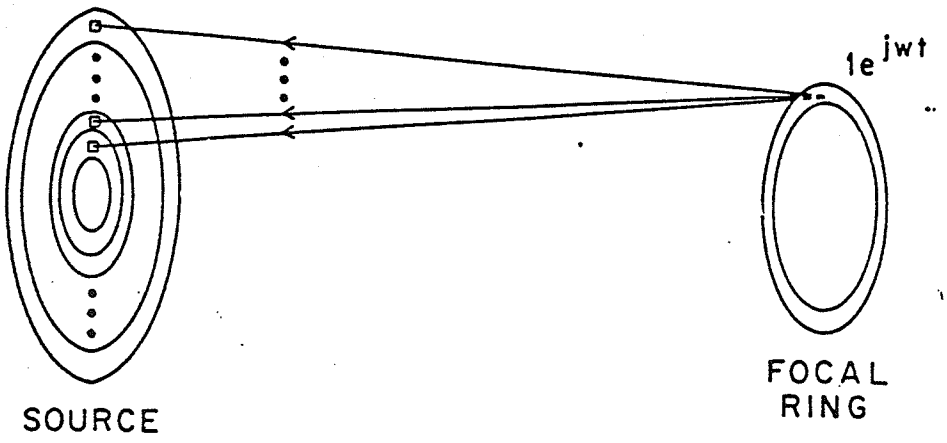

b) CROSS SECTION

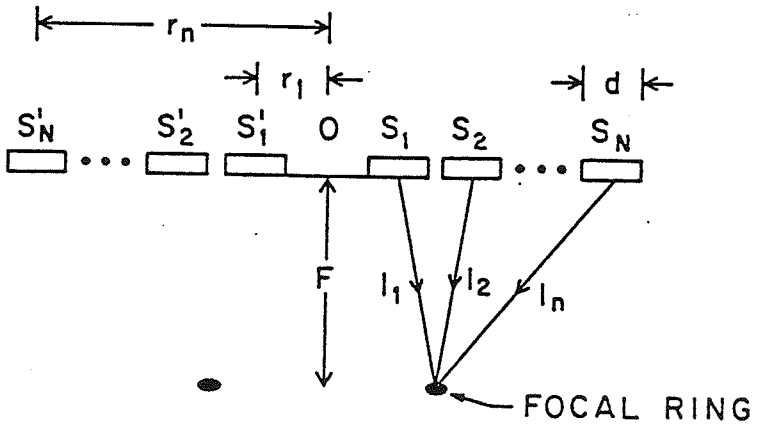

Figure 3.7. Synthesis of annular pattern using the FCM. a) A general view and b) a cross section.

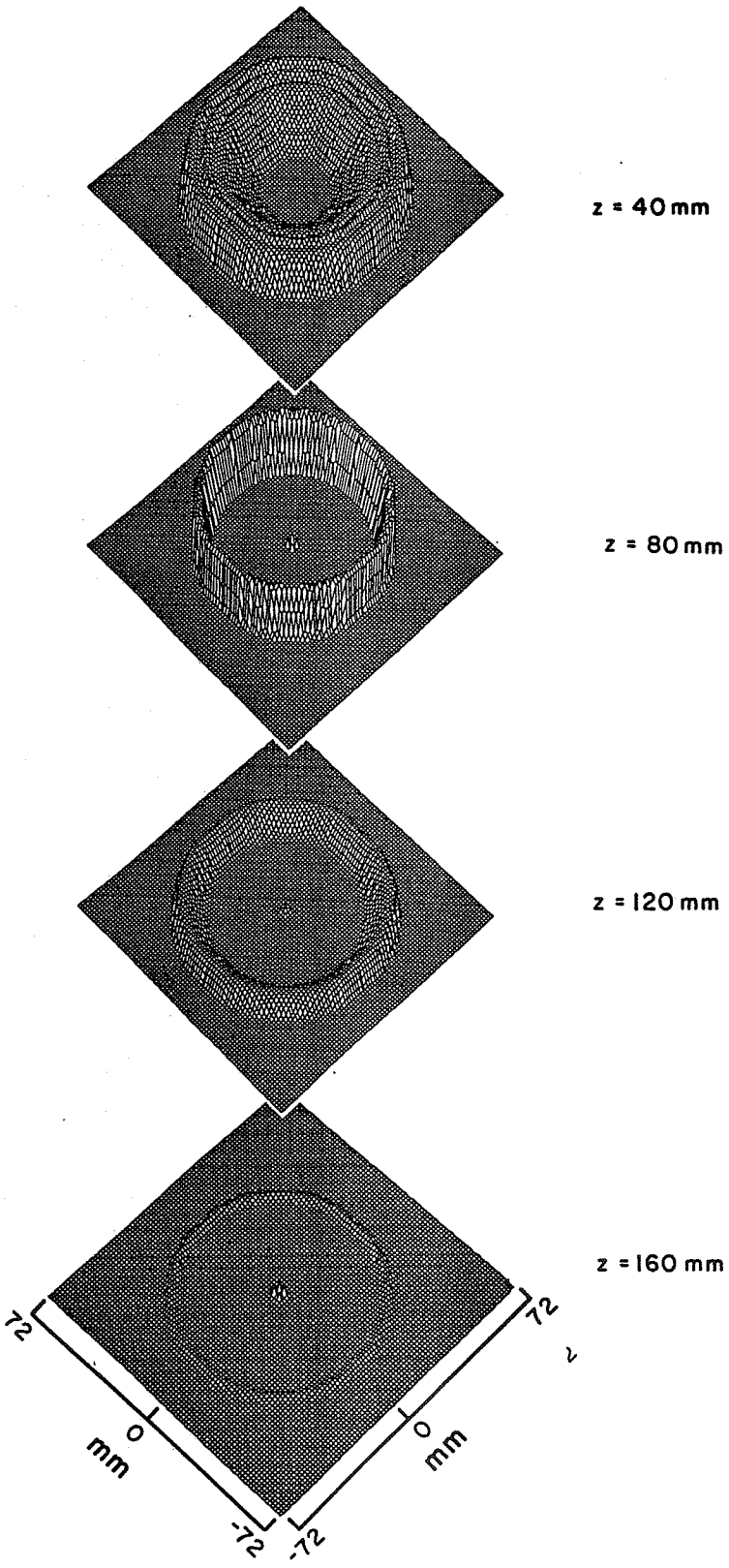

Figure 3.8. Synthesis of an annular pattern of 40 mm radius at z=80 mm. Surface plot of the resulting pattern in 4 transverse planes, parallel to the array surface, at different depths.

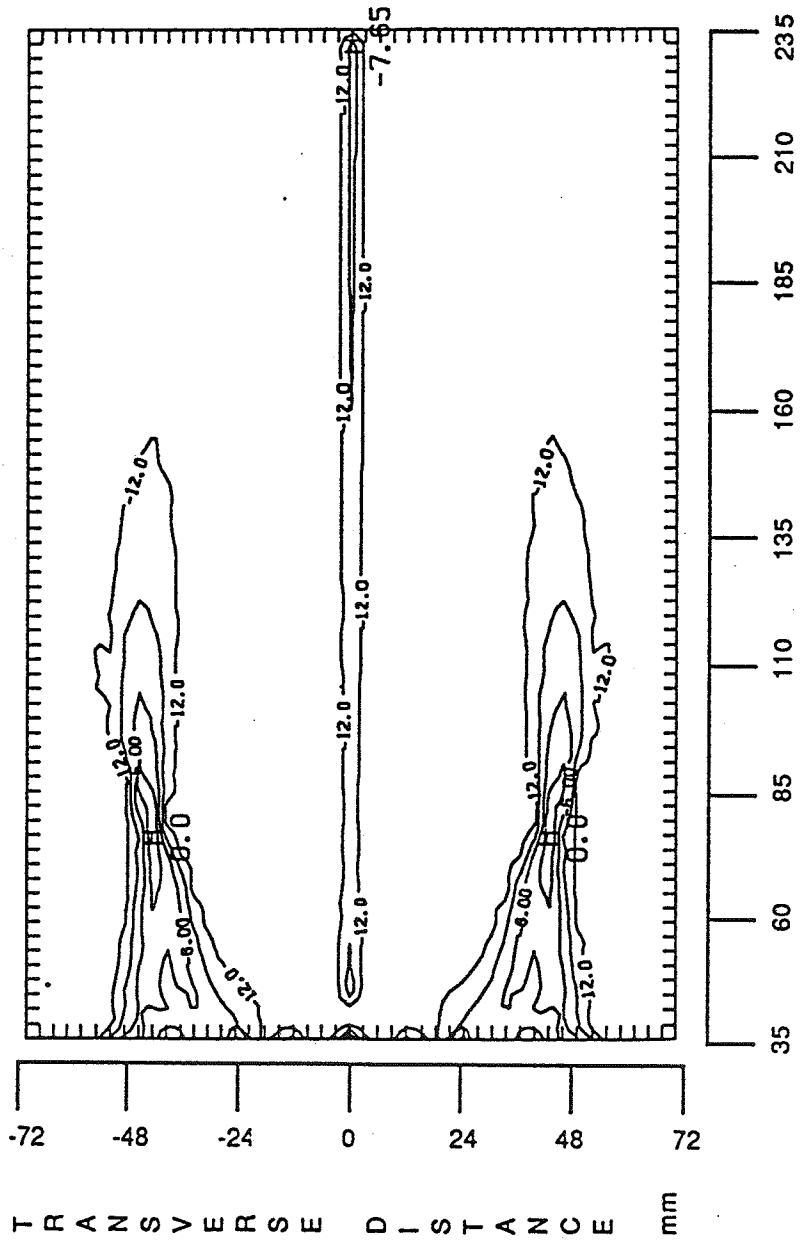

Figure 3.9. Synthesis of an annular pattern of 40 mm radius at 80 mm depth.
a) A contour plot of the pattern in the (r,z) plane with a contour increment of 3 dB.

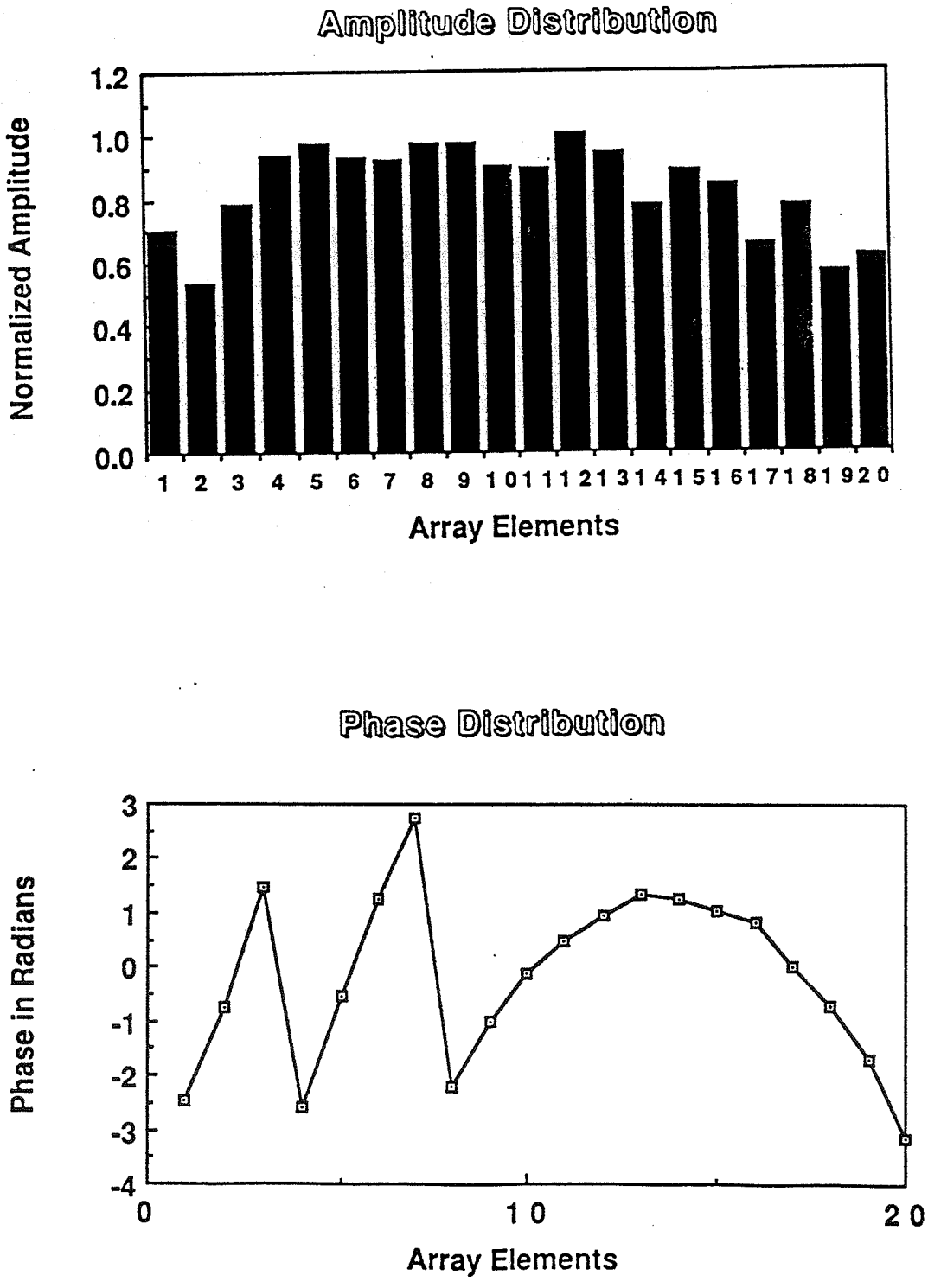

Figure 3.9. b) amplitude and phase distributions required for the synthesis of the above pattern.

four transverse planes including the focal plane (z= 80 mm) while Figure 3.9a) is a contour plot of the heating pattern in a plane containing the primary axis of the array. The width of the assumed ring was 5 mm. The phase and amplitude of the signals necessary to excite each of the elements are illustrated in Figure 3.9b).

The FCM can also be used to generate spot foci (conventional focusing) on the main axis. To do that, one assumes a point source at the desired location on the main axis. This can also be done by assuming a full disk shaped source of a small radius (< wavelength) at the desired main axis location. Figure 3.10a) is a contour plot of the pattern obtained by assuming a disk shape (4 mm diameter) at 100 mm from the array. Figure 3.10b) is a surface plot of the same pattern as seen in the focal plane (z= 100). The advantage of assuming a disk shaped small source over a point source is the production of a more diffuse focal spot compared to that resulting from a point source.However, the depth of field of the focal region is also increased and hence, the radius of the assumed source should be kept small.

Multiple foci on the main axis can be produced by assuming a disk shaped source (or a point source) at the location of each focus and adjusting the scaling factor to obtain the desired amplitude. Figure 3.11a) is a contour plot of the power deposition pattern resulting from simultaneously focusing at two depths (z= 60 and 130 mm). An elongated focal region can be generated by shortening the distance separating the two foci to allow their 3 dB focal regions to overlap. Figure 3.11b) is an elongated focus on the axis, obtained by simultaneously focusing at z= 85 and 100 mm, respectively. Figure 3.12 demonstrates the multiple focusing feature of the method by simultaneously focusing at three locations distributed along the main axis. The pattern is obtained by assuming a disk shaped source at z= 55, 100, and 160 mm from the applicator surface. The number of foci is obviously limited by the lower limit of the power necessary to produce therapeutic heating. These issues will be examined in Chapter 5 in which the resulting temperature distributions are investigated.

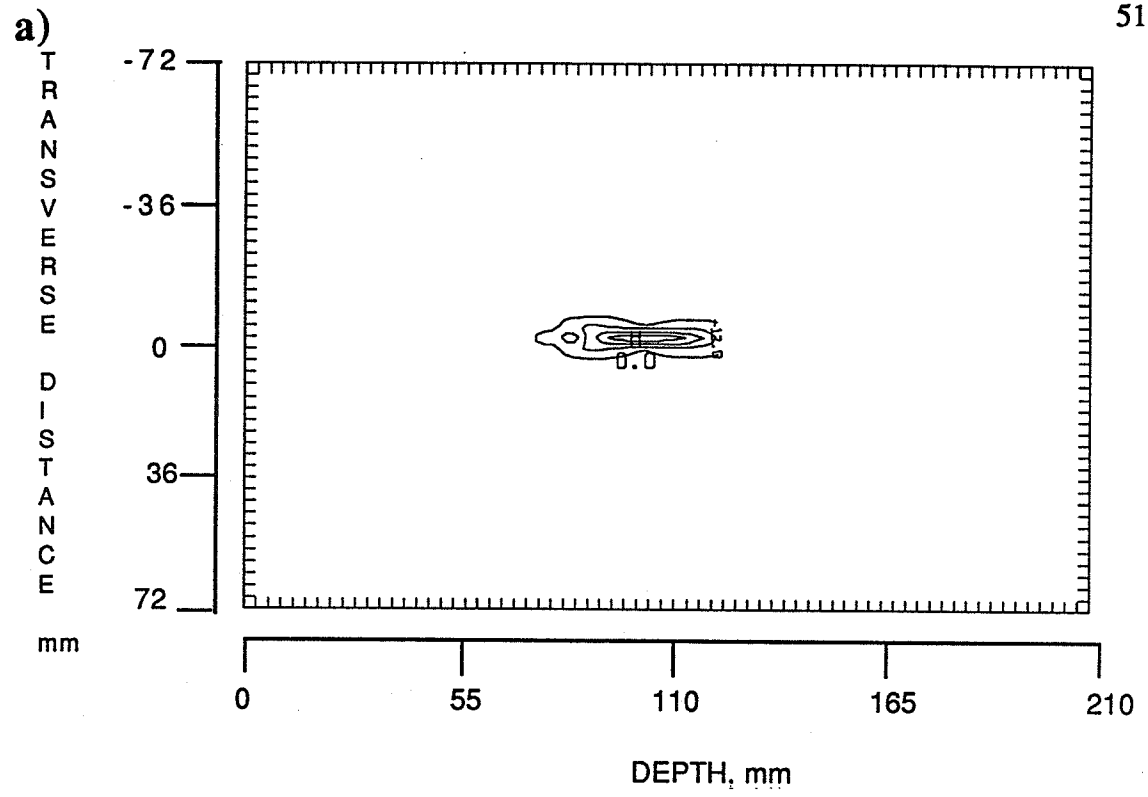

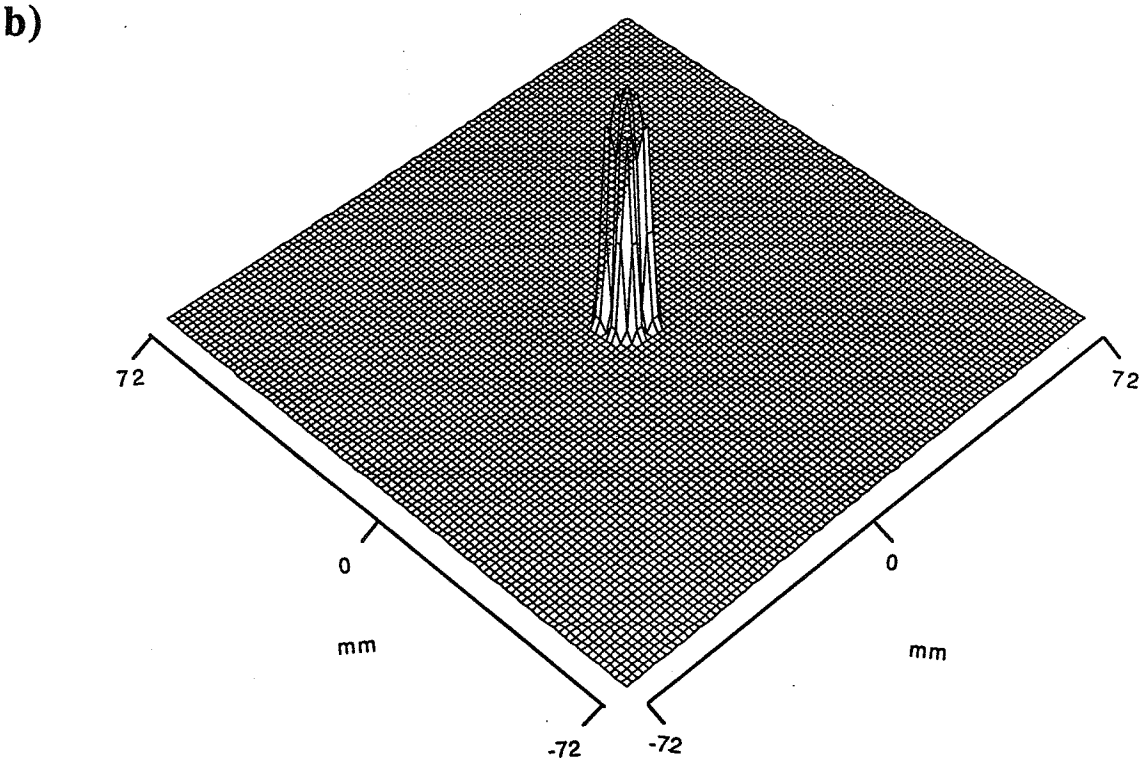

Figure 3.10. Simple focus at (0,0,80). a) A contour plot of the pattern in the (r,z) plane with a contour interval of 3 dB and b) a surface plot of the pattern in the focal plane (z=80).

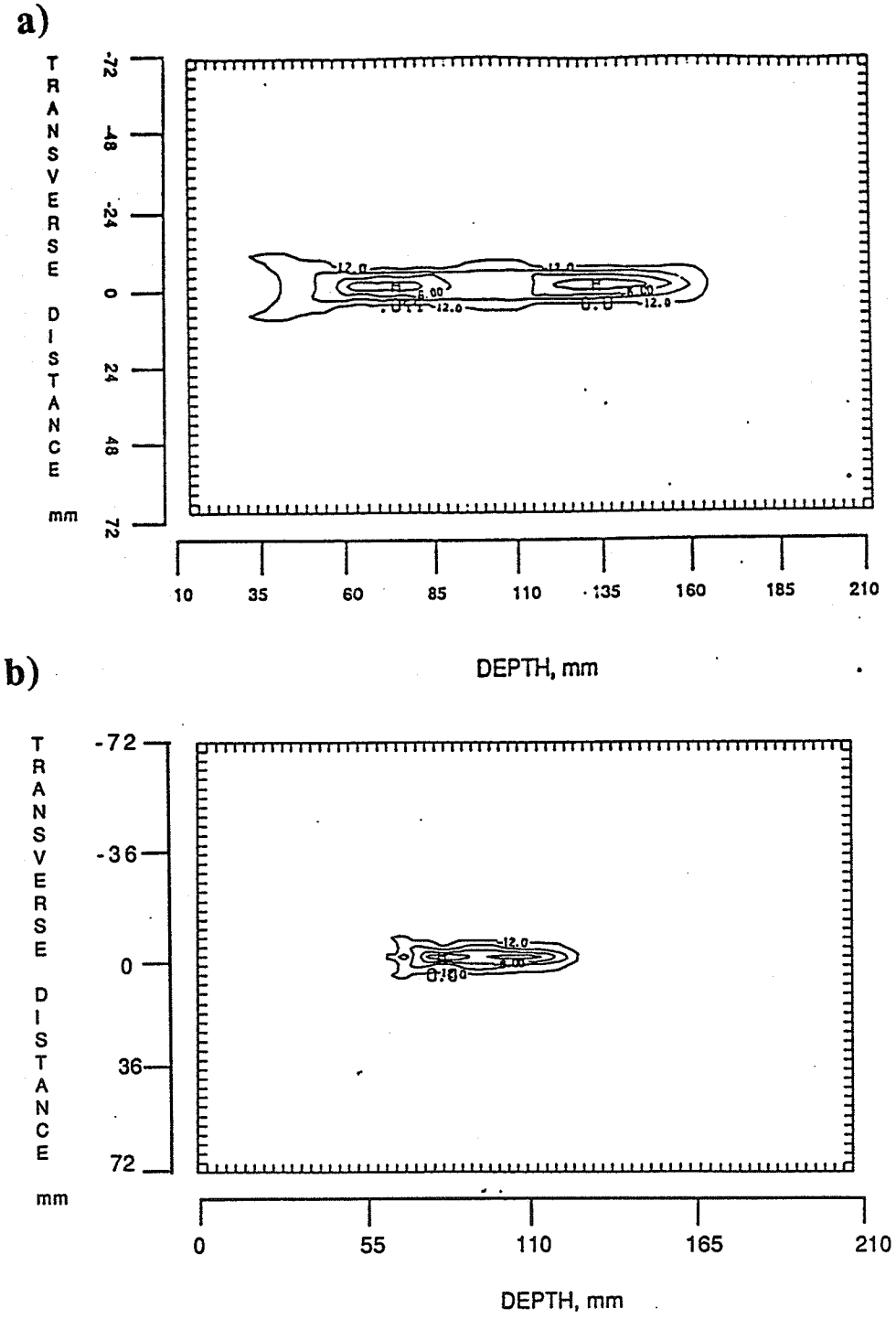

Figure 3.11. Multiple foci along the CRA axis. a) A contour plot of the pattern resulting when the array is simultaneously focused at (0,0,65) and (0,0,130), respectively, and b) a contour plot of the pattern resulting from simultaneously focusing at (0,0,80) and (0,0,105), respectively. Contours are given in increments of 3 dB.

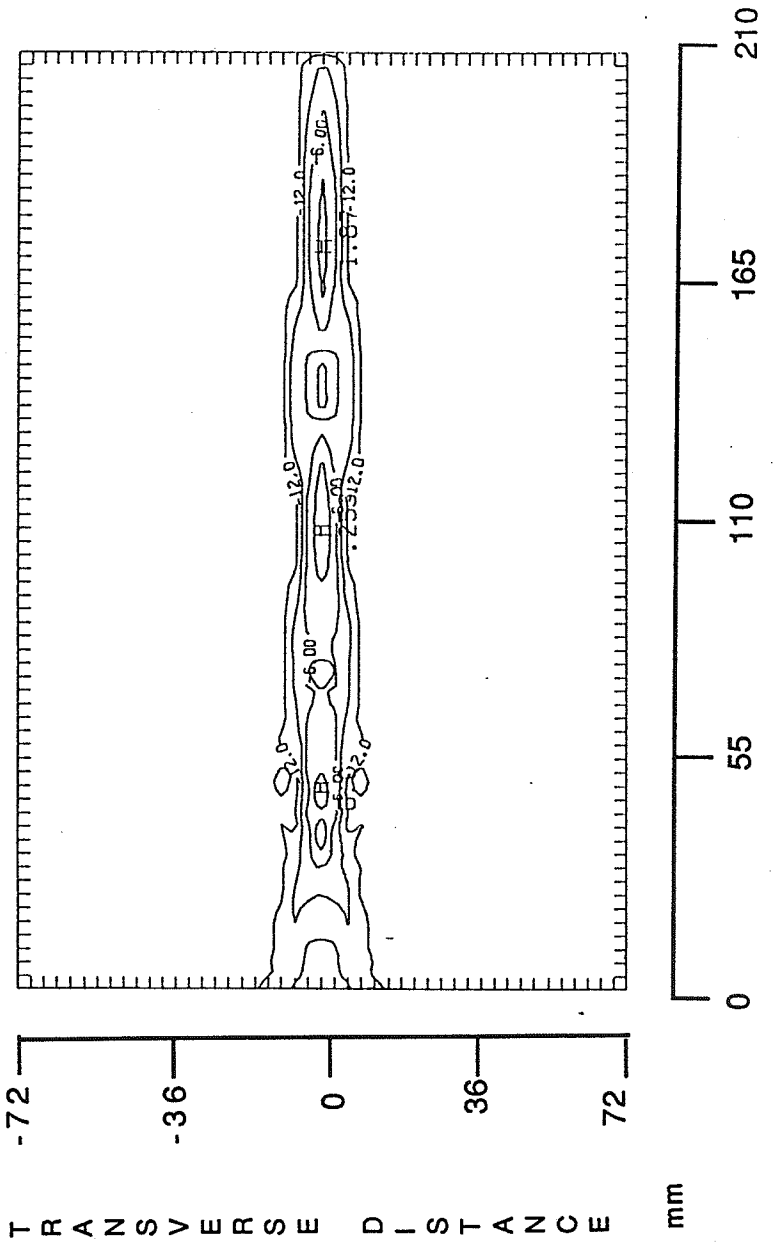

Figure 3.12. Multiple foci along the CRA axis. a) A contour plot of the pattern produced by simultaneously focusing at (0,0,55), (0,0,105), and (0,0,160) along the array axis. All intensities are normalized to that of the focus and contours are given at levels of 3 dB.

The synthesis of multiple annular rings is also demonstrated. Figures 3.13a) and b) illustrate the pattern obtained in the focal plane(z= 80 mm) from the synthesis of two annular rings and three annular rings, respectively.

Because of the circular symmetry of the assumed source, a high intensity region is produced on the main axis in the proximity of the transducer. This results from the constructive interference of the acoustic waves when interfering on the main axis. In fact, because of the symmetry of the applicator and that of the assumed source, acoustic waves interfer on the main axis with the same phase. Figure 3.14 is an illustration of the axial intensity resulting from the synthesis of a 40 mm radius ring at 80 mm depth. All intensities are normalized to that of the focus and then converted to the dB scale. It is noticed that the high intensity on the main axis exceeds the focal intensity and, hence, needs to be considered when using the FCM.

By using simple geometrical considerations, the formation of the sharp intensity and its extension on the main axis can be predicted. Figure 3.15 is a cross section of the CRA and the assumed annular source in the focal plane. By tracing only the acoustic rays emanating from the outermost and innermost elements to the opposite side of the assumed source, it can be noticed that the rays will consolidate along the segment BC on the main axis. An approximation of this extension can be computed easily by comparing the triangles ABC and DEC; therefore

$$\frac{r}{R} = \frac{F-d}{d} \tag{3.4}$$

$$d = \frac{R}{R+r} F \tag{3.5}$$

where r, R, d, and F are the synthesized annular ring radius, the applicator radius, the extension of the high intensity over the main axis, and the focal depth, respectively.

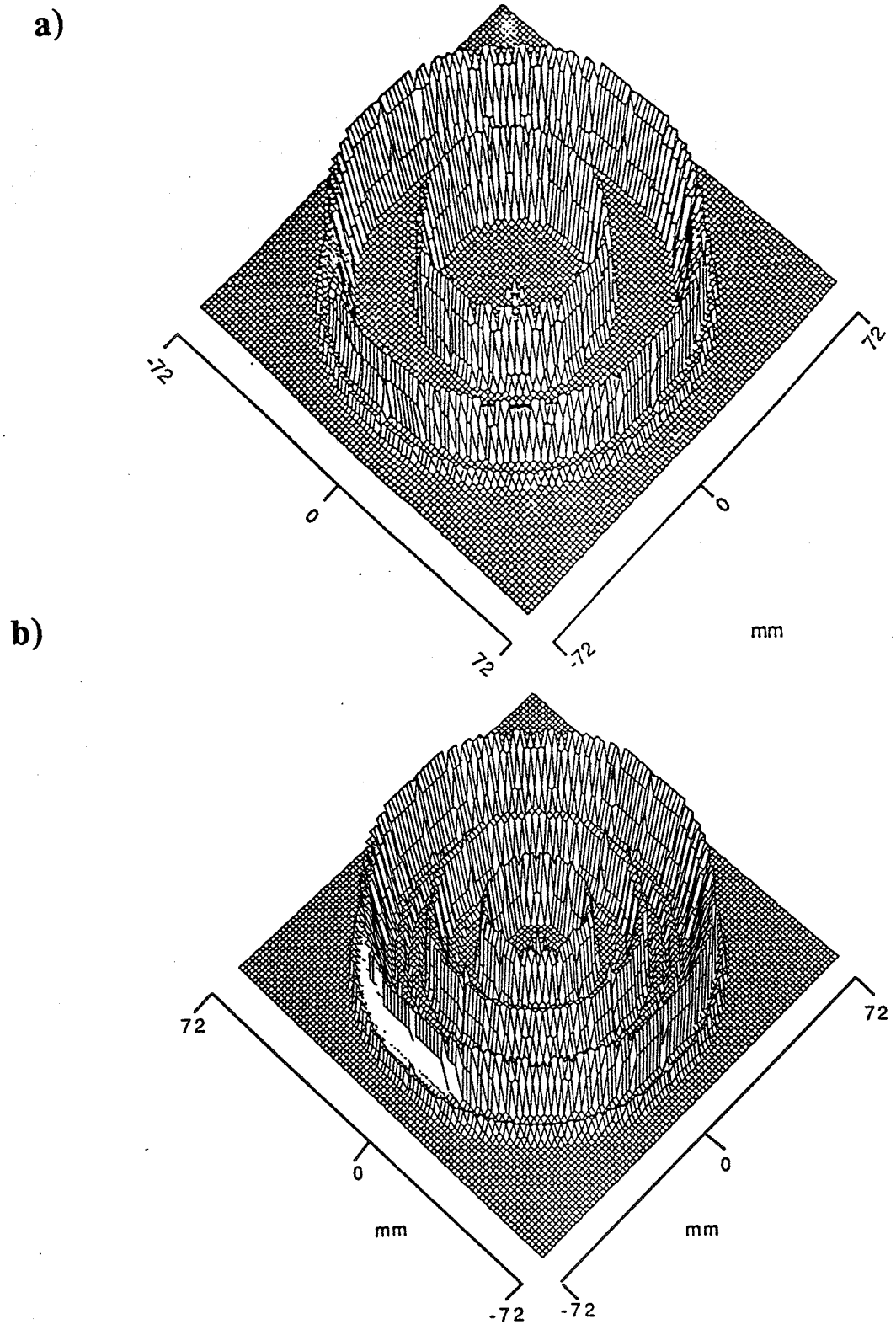

Figure 3.13. Multiple foci synthesis. a) A surface plot of two concentric annular foci of radii 30 and 45 mm, respectively. b) A surface plot of three concentric annular foci of 20,30, and 45 mm radii at 80 mm depth.

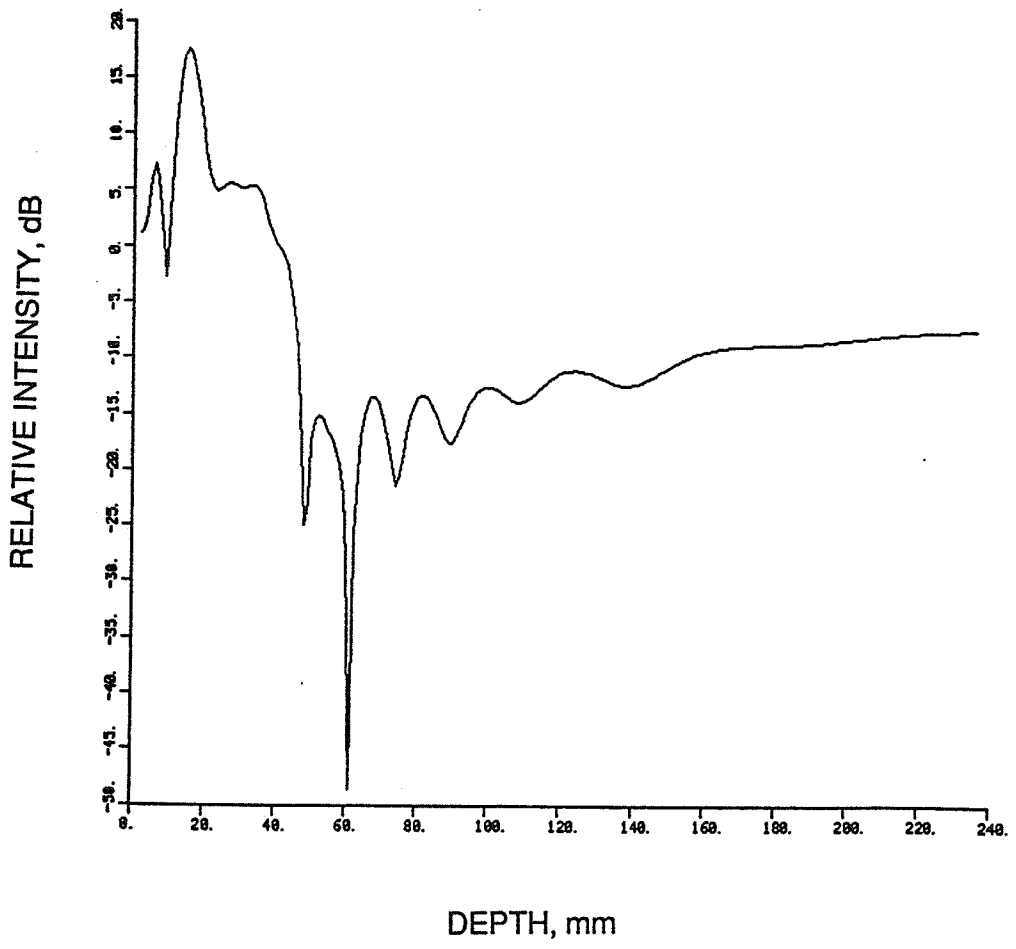

Figure 3.14. A plot of the relative intensity versus z (depth) . All intensities are normalized to the intensity evaluated at the focal site.

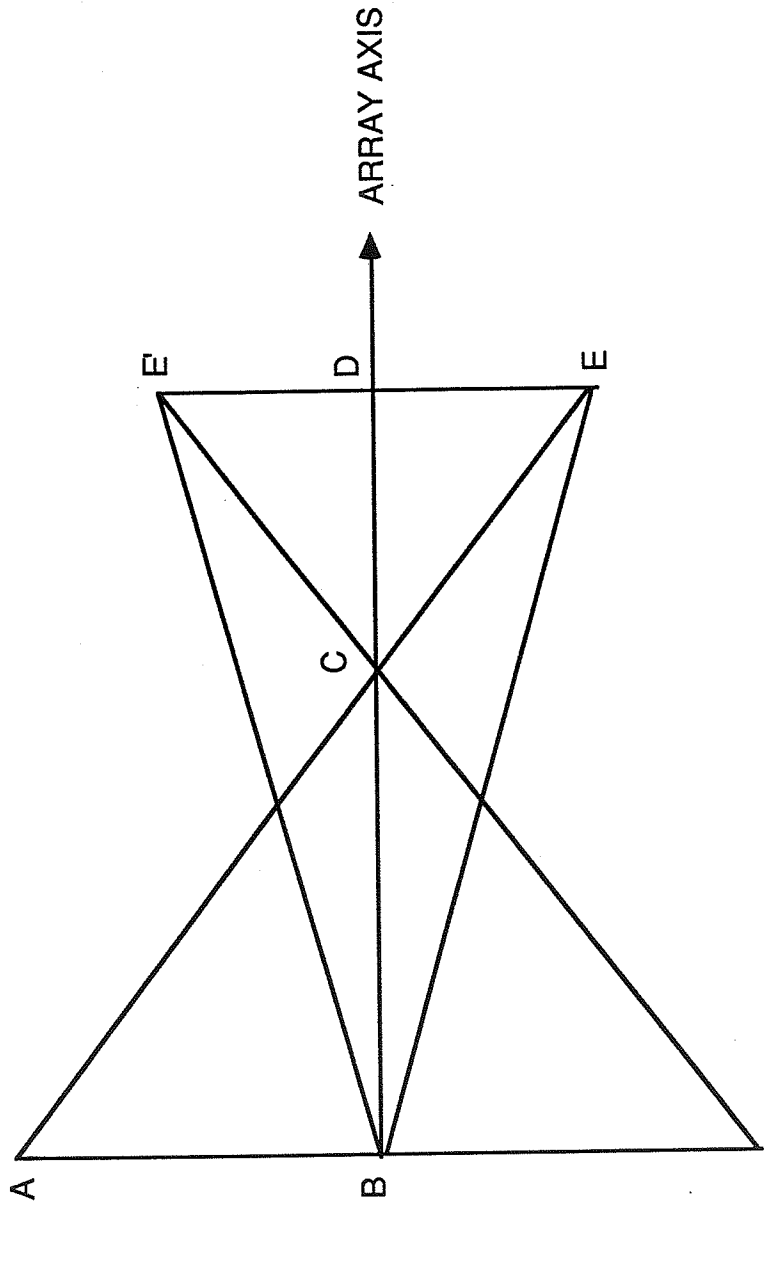

Figure 3.15. A schematic of a cross sectional view of the position of an assumed source, for the synthesis of an annular pattern via the FCM, with respect to the array.

This simple calculation indicates that the sound interference will cause a high intensity region on the main axis extending between the transducer and the point C as shown in Figure 3.15. Equation (3.5) shows that the radius of the focal ring needs to be at least equal to that of the applicator to limit the high intensity extension (on the main axis) to approximately half of the focal depth. However, the radius of the focal ring needs to be smaller than that of the applicator in order to obtain a reasonable gain at the focal site and, consequently, the undesired high intensity region will always extend to more than half of the focal depth.

This problem can be partially resolved by cooling the surface of the skin of the treated volume or by using a suitable bolus to contain the high intensity extension out of the patient body. However, the latter solution tends to limit the usable focal depth to a fraction of the designed one.

A more efficient solution is to create another pattern such that the interference of the two patterns is destructive at least over some part of the main axis. This can be produced by synthesizing an annular focal ring of a slightly different diameter and at a very close depth. The excitation signal of the new assumed ring should be identical to that used for the excitation of the original source except for its phase. In fact, if the original ring is excited with a signal A $\exp(j\phi)$, then the new annular source is excited by a signal A $e^{j(\phi-\pi)}$.

This procedure is best illustrated by an example. If a focal ring of a 40 mm radius at an 80 mm depth is to be synthesized, the approach consists of thinking of the problem as a multiple foci synthesis of two rings of 40 and 41 mm radius at 80 and 79 mm depth, respectively. The FCM is then applied by assuming two rings of 40 and 41 mm at the appropriate location. These assumed rings are then excited by identical signals except for a phase difference of π (i.e., A $e^{j(\phi-\pi)}$). This procedure will lead to destructive interference along a part of the main axis, and the extension of the high intensity axial region is reduced. Figure 3.16a) illustrates the normalized intensity resulting on the primary axis when the outlined procedure is used. It is noticed that the high intensity extension is limited to less

a)

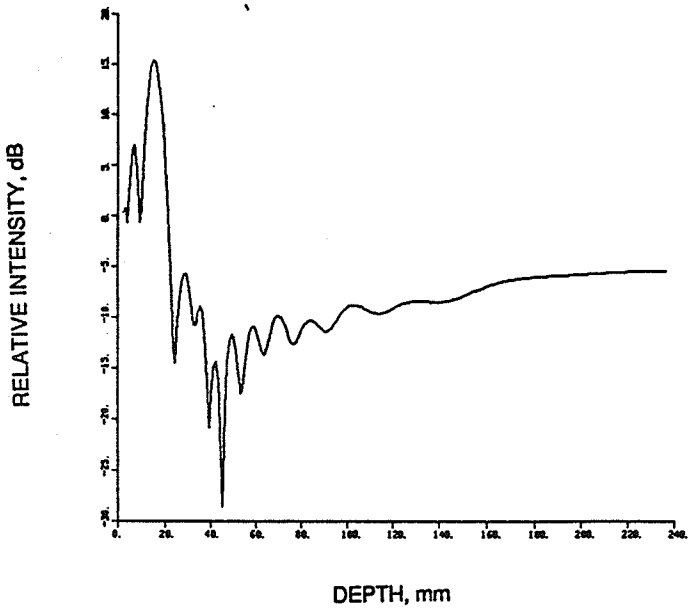

b)

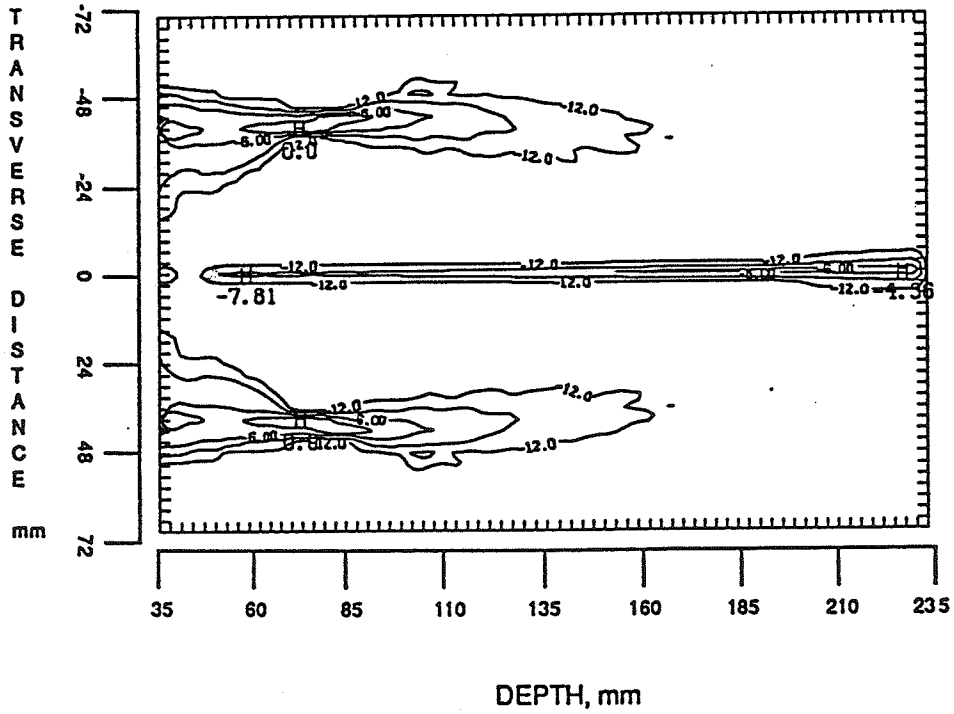

Figure 3.16. a) A plot of relative intensity in dB along the axis as a function of z (depth). Intensity is normalized to the intensity evaluated at the focal site. b) A contour plot of a pattern produced by assuming two "rings" of slightly different sizes with surface velocities 180^0 out of phase. The procedure is used to reduce the intensity of secondary foci along the main axis.

than 2 cm compared to the 5 cm extension obtained earlier (see Figure 3.14). Figure 3.16b) is a contour plot of the resulting heating pattern in the (r,z) plane.

3.4.2 Synthesis of an annular focal pattern using a pseudo-direct approach.

The high intensity extension on the main axis of the array is explained by the interference of the acoustic waves constructively on the main axis. In fact, because of the circular symmetry of the assumed source, the sound beams consolidate along the main axis, and, consequently, a high intensity region results in the proximity of the transducer. However, because of the circular symmetry of the applicator, the array is constrained to produce annular patterns even if the assumption of an annular source is replaced by assuming a point source placed arbitrarily on a point on the periphery of the desired ring. In fact, by assuming a point source placed at a point P on the periphery of the desired annular ring, the FCM is then used to calculate the phase and amplitude of the excitation signal as explained earlier. However, due to the circular geometry of the applicator, the excitation signal will result in an annular heating pattern with the desired radius. The name pseudo-direct is due to the similarity between this method and a direct approach which is frequently used in the literature. The direct approach is summarized in the following paragraphs as a reference.

As proposed in [15,17], the method consists of calculating the phase delay necessary to be applied to each annular element such that the resulting field converges at a point P. As illustrated in Figure 3.17a), the delay is computed by calculating the distances separating point P from the annular elements S_1, S_2,. , S_N which are then divided by the sound velocity in tissues to find the time delay. The result is finally converted to phase delay as follows:

$$\Phi_i = \frac{2\pi f \sqrt{F^2 + (r\text{-}id)^2}}{C} \tag{3.6}$$

a)

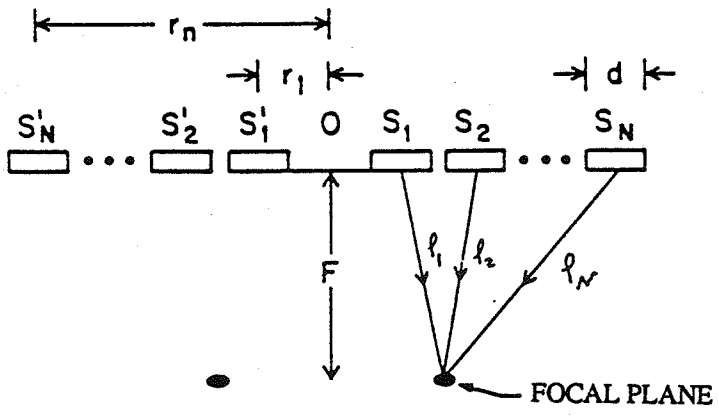

b)

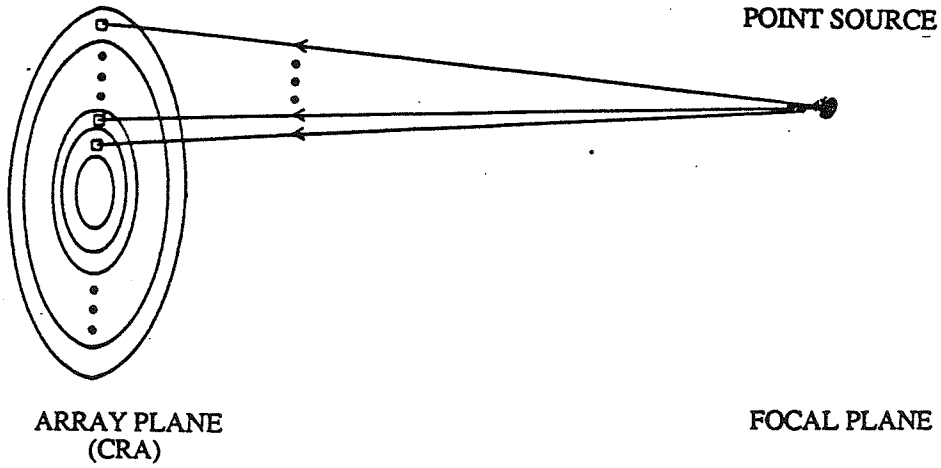

Figure 3.17. A schematic of the pseudo-direct synthesis technique. a) A cross section view and b) a general view of the position of the assumed source with respect to the array.

Once each element is excited with the proper signal, the pattern in the focal plane is an annular ring of radius r (distance separating the point P from the main axis). In the remainder of this chapter, this will be referred to as the direct phasing method.

It is obvious that a slight modification of the FCM, as explained earlier, will lead to heating patterns similar to those obtained by the direct phasing method. The main difference between the original FCM and this procedure is with respect to the assumed source. In fact, while the assumed source in the FCM is an annular ring, the one assumed here is a point source. Figure 3.17b) is a schematic illustration of the array and a point source placed at a point P. The point P is chosen arbitrarily on the periphery of the ring to be synthesized. The effect of this point source is then computed at the center of each annular element of the array. These values are finally conjugated and used as excitation signals to the proper array elements.

The annular patterns obtained using this technique are similar to those obtained by the direct phasing method because both methods assume a point source and neglect the effect of the farthest side of the array. The power deposition pattern of synthesizing a 40 mm radius ring at an 80 mm depth using the pseudo-direct method is illustrated in Figures 3.18. Figure 3.18a) is the surface plot of the heating pattern in six transverse planes including the focal plane at z= 80 mm, while Figure 3.18b) is a contour plot of the pattern obtained in the (r,z) plane. The driving phase and amplitude as calculated by the pseudo-direct method are given in Figure 3.18c).

In summary, the synthesis of annular heating patterns can be achieved using the FCM and the pseudo-direct techniques. An outline of a direct phasing method was then presented. In a later section, the direct and pseudo-direct methods will be compared to the FCM, and advantages and limitations of each will be discussed.

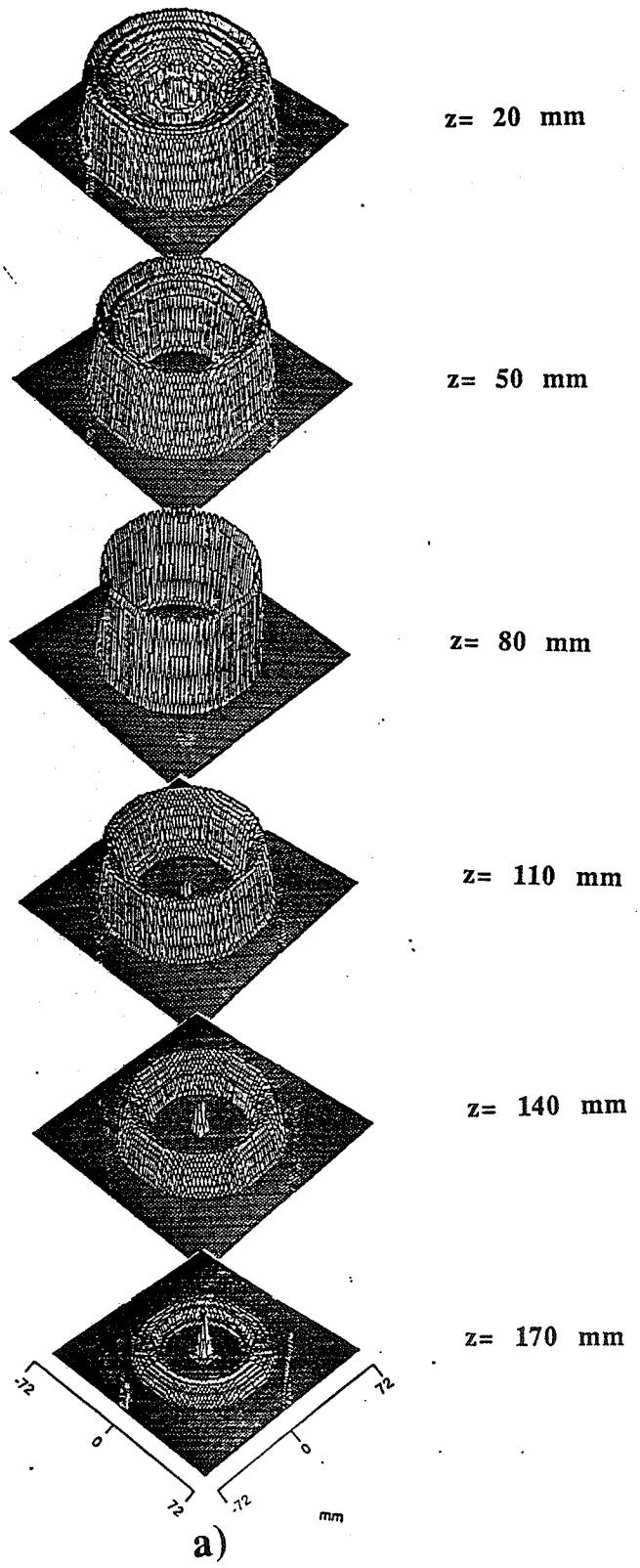

Figure 3.18. a) A surface plot of an annular pattern produced by the pseudo-direct technique . The pattern is of a 40 mm radius at an 80 mm depth. Several transverse planes at different depths are shown.

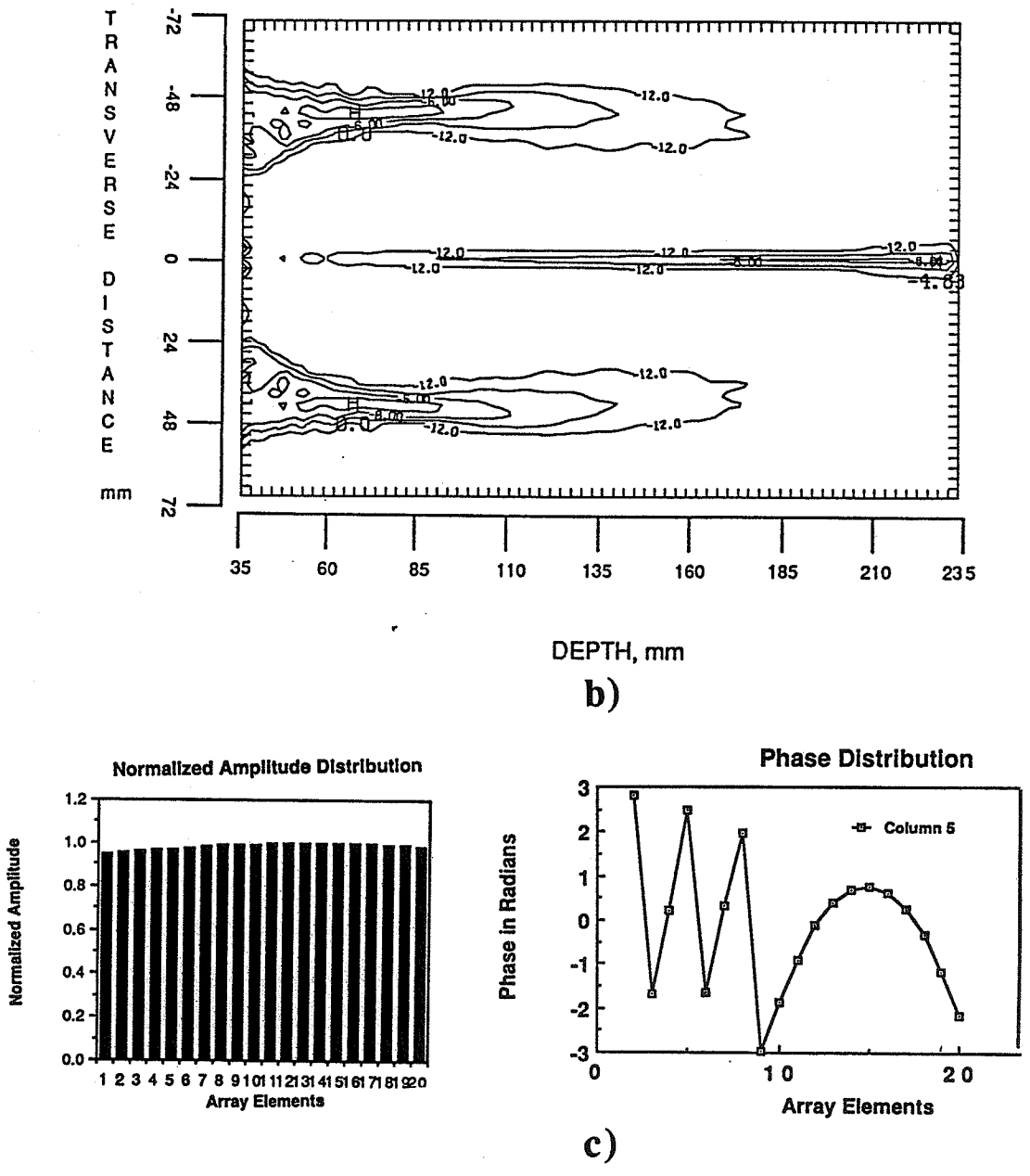

Figure 3.18. b) A contour plot of the pattern of a) in the (r,z) plane. The contours are given at intervals of 3 dB. c) Magnitude and phase distributions of the required excitation signal.

3.5 The Design Parameters

3.5.1 Geometrical considerations

Due to the particular symmetry of the applicator and that of the synthesized patterns (annular rings), we have observed that undesired hot spots (secondary foci) might result on the main axis in some cases. In this section, an attempt is made to understand the origin of these undesirable hot spots and some useful approaches to reduce the effect of such undesired heating are discussed.

When synthesizing annular rings using a CRA, the direct phasing method leads to a secondary focus on the main axis beyond the focal plane. This secondary focus had been observed by Huu and Hartemann [15] and later described by Cain and Umemura [17].

The FCM also leads to a similar secondary focus in some cases, but with a lower intensity than those produced by the direct phasing method. To make a meaningful comparison, the secondary focus intensity was normalized in both cases to the peak intensity produced at the annular focus. The observed difference in the normalized secondary focus intensities between the two methods is due to the amplitude shading of the driving signal required by the FCM and to the nature of the assumed sources.

For the same synthesis parameters (annular ring radius, frequency, depth, etc.), the normalized secondary focus resulting from the application of the FCM is about 4 dB less than that resulting from the direct phasing method. Figure 3.19a) illustrates the heating pattern obtained in the (r,z) plane for the synthesis of a 40 mm radius ring at an 80 mm depth using the FCM, while Figure 3.19b) is the same pattern synthesized using the direct phasing method. It should be noticed that the secondary focus intensity, in Figure 3.19a), is about 8 dB less than that of the annular focus. Figure 3.19b) shows that ,for the same case, the secondary focus intensity produced by the direct phasing method is about 4.5 dB less than that of the annular focus. However, the effect of these secondary focus intensities will be further reduced by blood perfusion in the normal tissues. This issue will be discussed in Chapter 5 when the resulting temperature distributions are calculated.

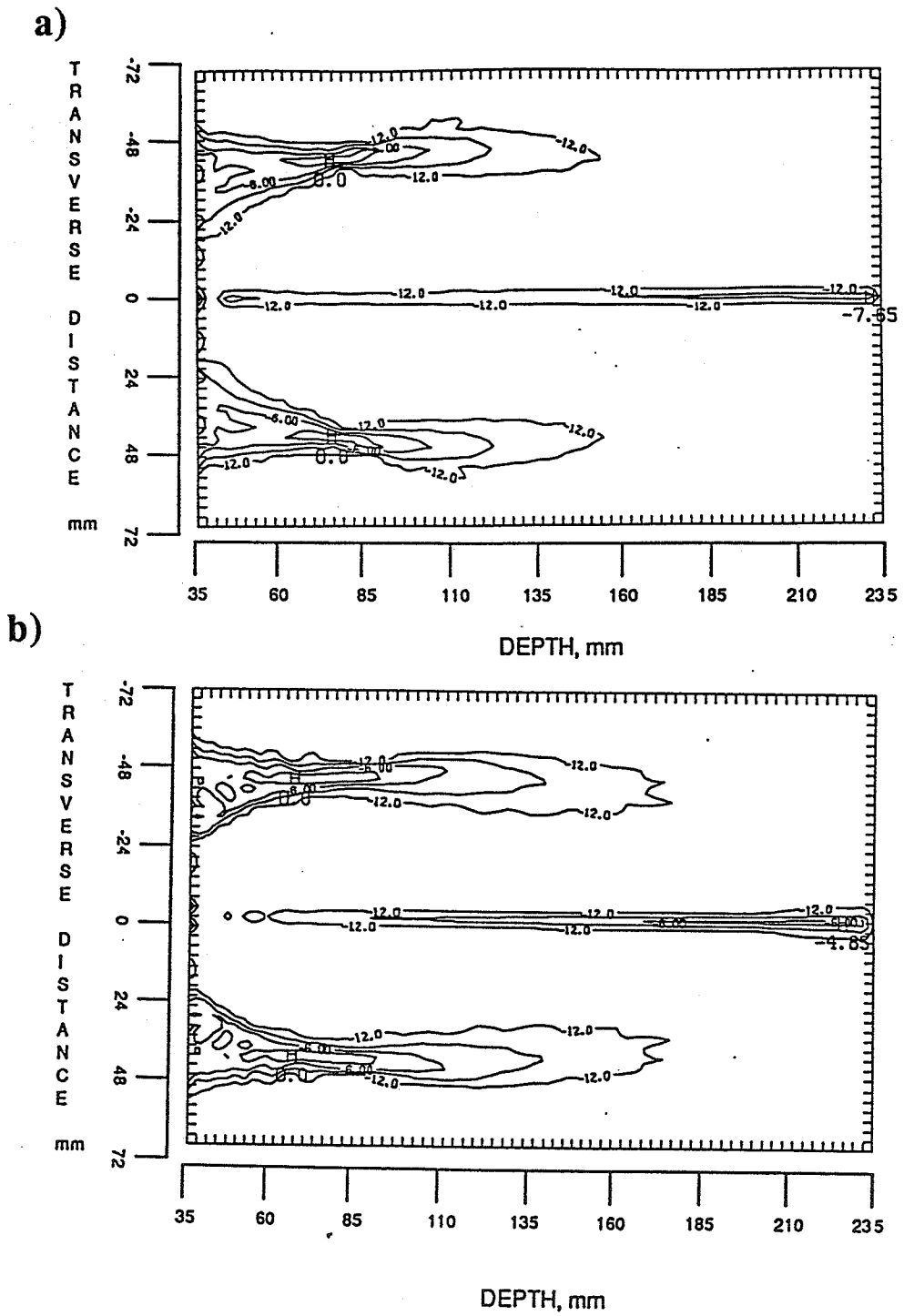

Figure 3.19. Comparison between the FCM and the pseudo-direct method. a) a contour plot in the (r,z) plane of an annular pattern of 40 mm radius at 80 mm depth synthesized by the FCM and b) the same pattern synthesized using the pseudo-direct method.

The problem becomes more serious when the array is used to synthesize annular patterns with smaller diameters. In fact, to avoid significant secondary foci, the radius of the synthesized pattern should be kept larger than that which divides the array surface into two equal areas. This half-area radius R_s is precisely equal to the applicator radius divided by $\sqrt{2}$. This is due to the fact that when the synthesized radius is smaller than R_s, more than half of the applicator energy (extracted energy is proportional to the surface area) will be steered toward the main axis beyond the focal plane, as illustrated in Figure 3.20a). Hence, a strong secondary focus appears at point F' beyond the annular focus.

This interpretation is in accordance with that given by Beard et al. [20]. In fact, when the synthesized radius is less than or equal to R_s, the situation is similar to that which would have resulted from a specially designed lens, illustrated in Figure 3.20b).

For a radius greater than R_s, more than half the energy extracted from the applicator is steered toward the outside of the annular focus as shown in Figure 3.21a). In the latter case, the situation is similar to that which would have resulted from the lens presented in Figure 3.21b).

The effect of the masking procedure proposed in [17], to reduce the secondary focus intensity, is to actually reduce the effective applicator radius to satisfy the requirement that the synthesized radius should be of the order of R_s of the array. More specifically, the direct phasing method was used to synthesize a focal ring of a radius of 30 mm at an 80 mm depth using an applicator of a 60 mm radius [17]. The resulting secondary focus intensity, beyond the focal plane, exceeded that of the annular focus. This result could have been predicted because the synthesized radius is far less than R_s of the applicator (R_s=42 mm). However, the authors proposed to mask the outer 5 annular rings which would reduce the effective applicator radius to 45 mm and, consequently, reduce R_s to 31.8 mm. The contour plot of the pattern obtained by masking the outermost 15 mm width ring, using the direct phasing method, is reproduced and presented in Figure 3.22a). Figure 3.22b) is the pattern obtained using the FCM as a means of synthesis. Figure 3.22a) suggests that while masking reduces

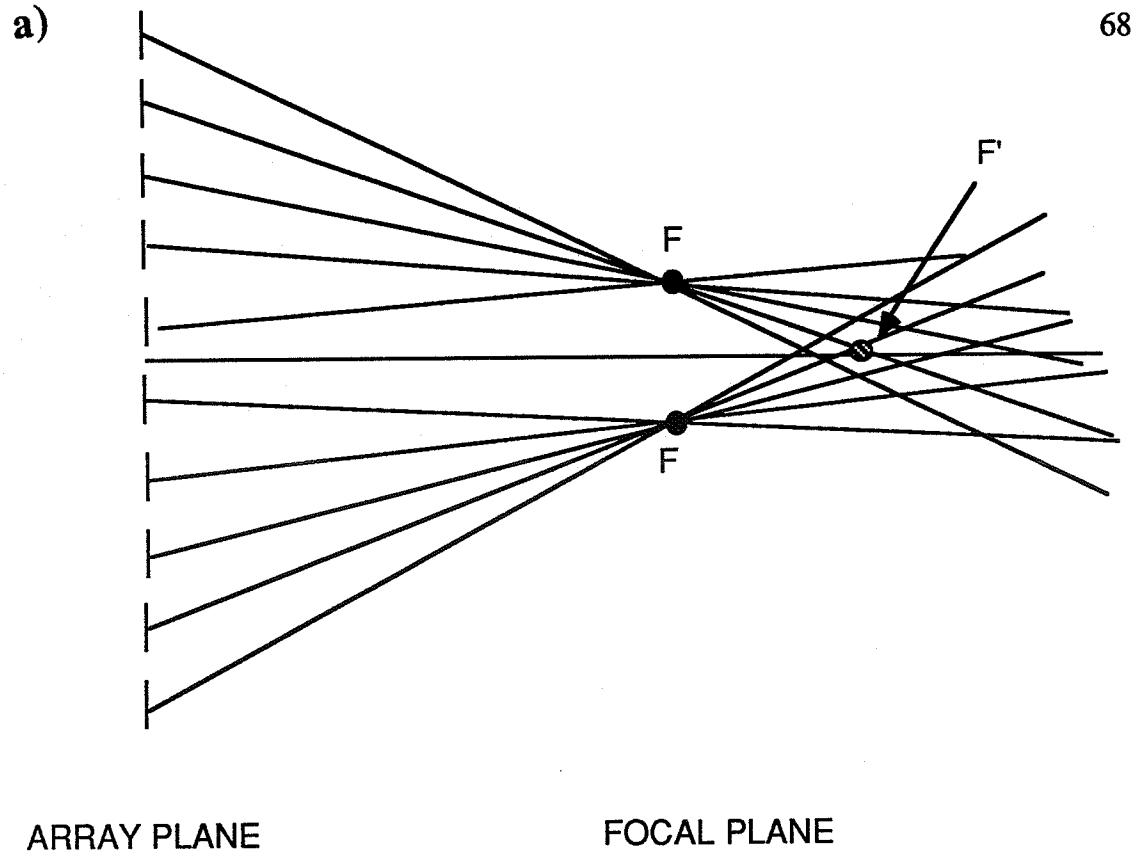

Figure 3.20. a) A schematic of synthesis of an annular pattern of small radius ($R \leq R_s$). A secondary foci is developed at point F'. b) Formation of a secondary foci beyond the focal plane of a specially designed concave lense.

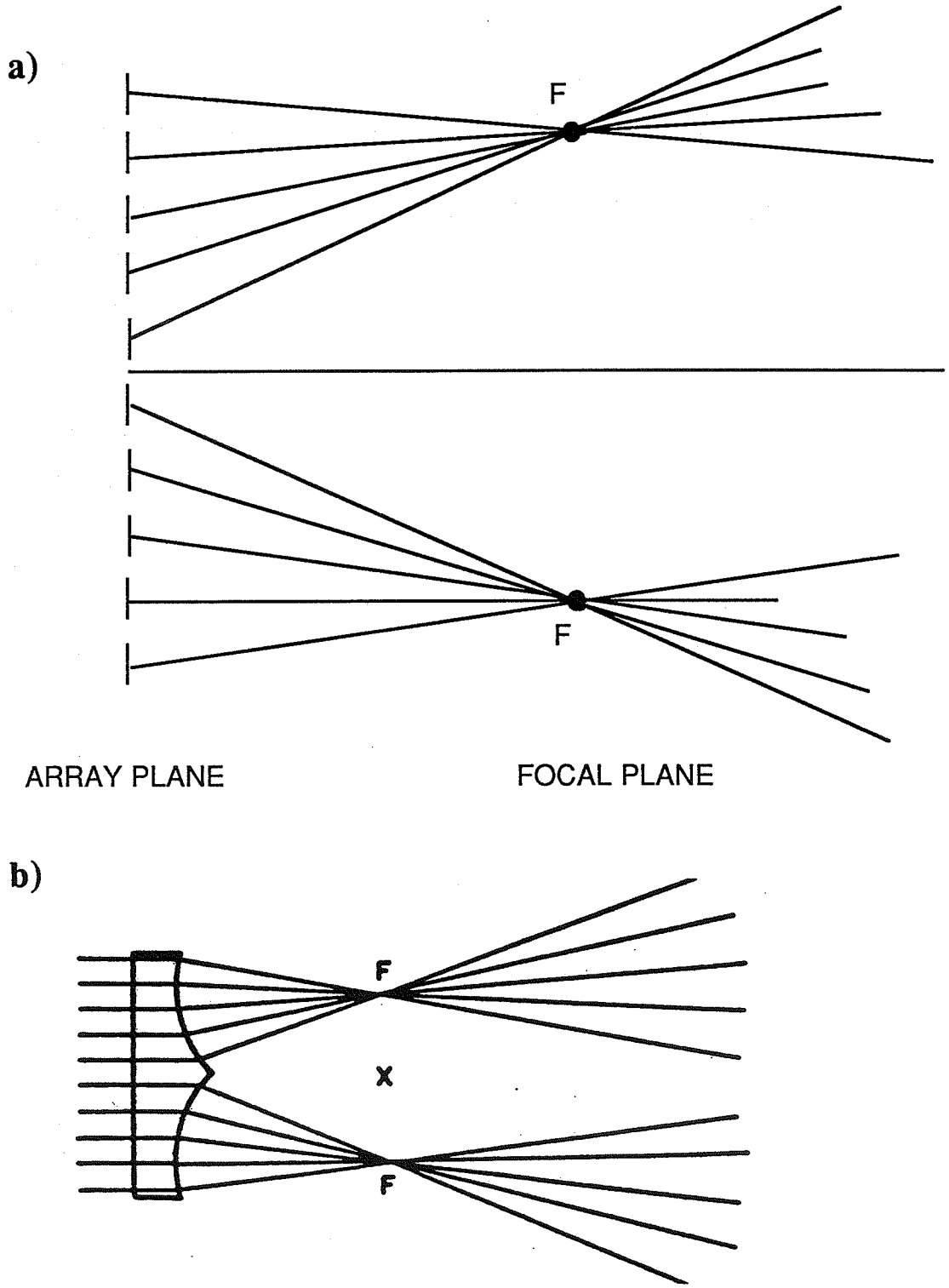

Figure 3.21. a) A schematic of a large size annular pattern synthesis. b) A similar type of pattern produced by a specially designed lense.

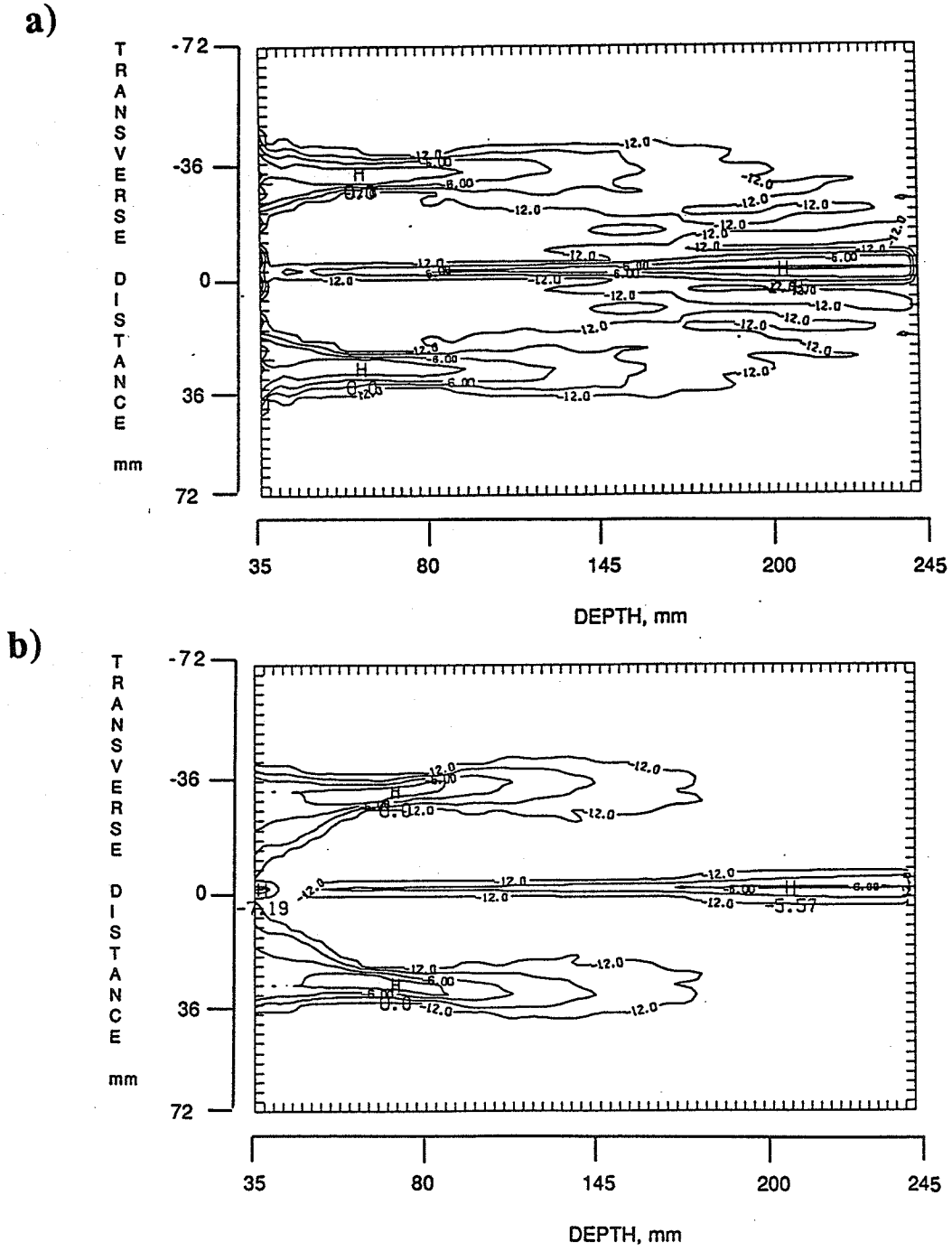

Figure 3.22. Reduction of the secondary foci intensity. a) A contour plot of the synthesis of a 30 mm radius annular pattern at 80 mm depth using the direct method. The secondary foci, beyond the focal plane, intensity was reduced by masking the 5 outer elements as proposed in [17]. b) The same pattern synthesized using the FCM (no masking).

the secondary foci intensity, it also leads to a substantial surface heating and, consequently, cannot be considered an efficient solution.

In conclusion, the preceding analysis suggests that a potential problem might result when synthesizing annular heating patterns of a radius smaller than R_s because of the formation of a secondary focus beyond the focal plane. A higher frequency might be used to reduce the intensity of the secondary focus beyond the focal plane. However, the possible depth of treatment would be shorter due to the attenuation effect.

3.5.2 The driving amplitude control of the annular elements

In general, focusing is achieved by exciting each element of a phased array by an appropriate signal. The excitation signal is established by calculating the length of the path separating the center of each element from the desired focus location. This length is then divided by the sound velocity in tissue, and the resulting time delay is converted to the necessary phase delay for each element. However, the FCM establishes not only the necessary phase delay but also the amplitude of the signal needed for each array element. The requirement of amplitude control, although easy to be implemented electronically, might lower the amount of acoustic power extracted from array, in some cases, to a limit where heating the tumor might become difficult, if not impossible.

To illustrate the problem of amplitude control, a heating pattern is generated by assuming an annular focal ring of a 40 mm radius at an 80 mm depth from the surface of the CRA. For this example, the width of the assumed ring is taken to be 1 mm.

The amplitude of the required signal is illustrated in Figure 3.23a). The required driving phase is shown in Figure 3.23b) which suggests that while some annular elements are driven with relatively high amplitude signals (e.g., 4, 5, 6), others are excited with very small amplitude signals (e.g., 2, 8, 12, 15, 18, 20). This observation means that some elements are delivering their maximum power while others are merely supplying a fraction of

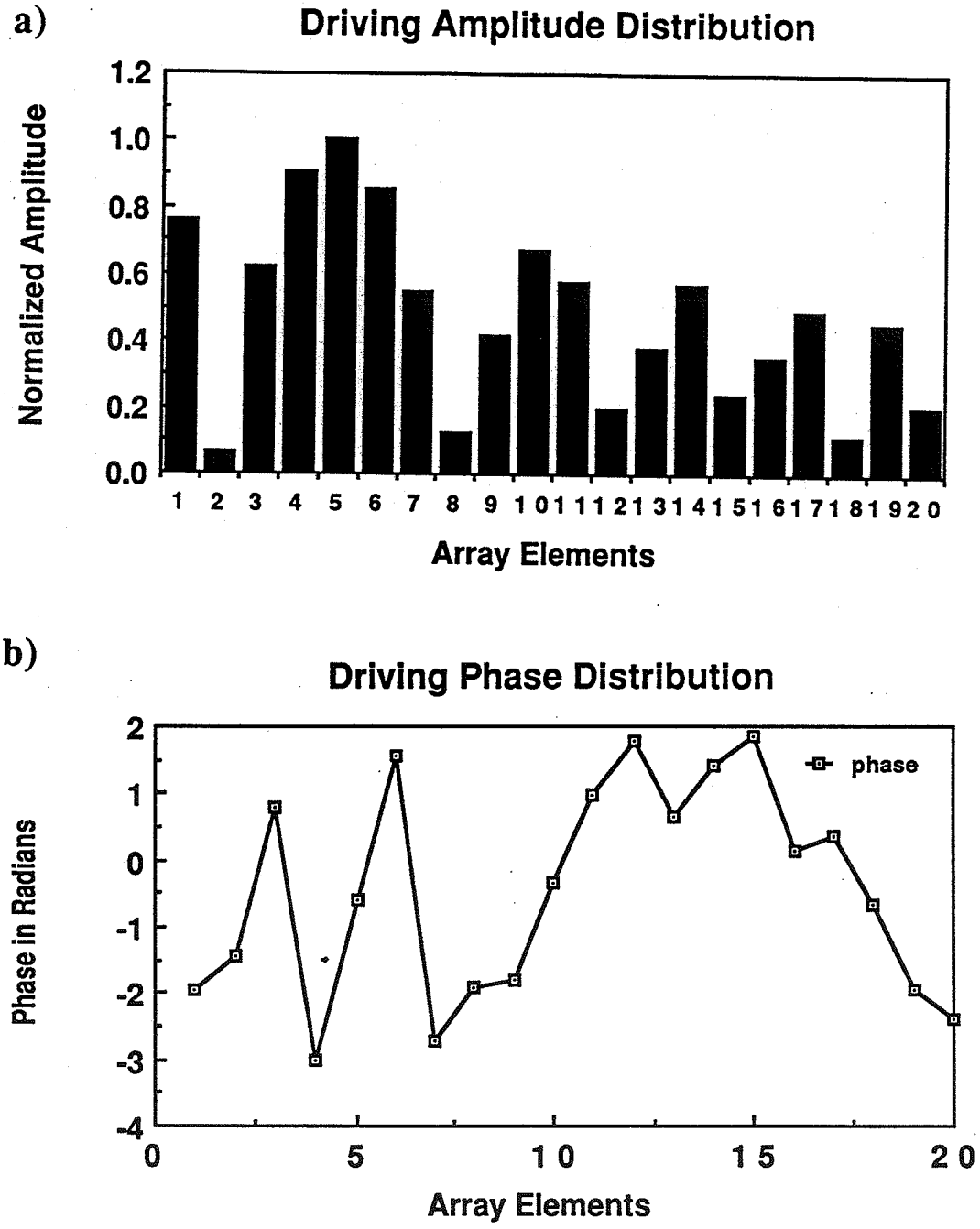

Figure 3.23. Phase and amplitude distributions of the driving signal as required by the FCM. a) The normalized amplitude distribution and b) phase distribution. The assumed source is an annular ring of 40 mm at 80 mm depth.

it. The amplitude of the excitation signals, established by the FCM, needs to be optimized in order to allow the array elements to deliver enough power to induce therapeutic heating.

The amplitude of the driving signal depends on many factors, among which are tumor size, depth, the number of synthesized rings, and the width of the focal ring. It is then necessary to define a standard quantity to enable the therapist to judge how efficiently the array is excited and to estimate the maximum amount of power that can be extracted from the array for a given signal amplitude distribution.

Intuitively, such a standard quantity should take into account the power delivered by every annular element, for a given magnitude distribution, to that which would have resulted if the elements were uniformly driven to deliver their maximum power. However, because the surface areas of the annular elements are different, an averaging procedure over the applicator surface is necessary. We will call such a standard quantity "the amplitude shading factor" and define it as follows:

$$\varepsilon = 1 - \frac{\sum_{i=1}^{N} (A_i)^2 S_i}{A^2 S} \tag{3.7}$$

In the above equation, A_i and S_i are the amplitude of the driving signal of element i and its surface area, respectively. Also, A is the maximum excitation magnitude allowed by the ceramics and S is the total effective surface of the applicator. It is to be emphasized that for a fixed driving amplitude excitation (A_i=A=constant and $\sum_{i=1}^{N} S_i$=S), the amplitude shading factor as calculated by Eq. (3.7) is zero .

The amplitude shading factor is an important quantity in determining the gain of the array as will be discussed in Section 3.5.4. Simulations show that, for a specified treatment depth and tumor diameter, an optimum value of the amplitude shading factor can be obtained by adjusting the width of the assumed focal ring. To illustrate this point, a focal ring of a 30

mm radius at an 80 mm depth was synthesized for different widths of fictitious annular sources. The width of the assumed ring was varied from 2 to 15 mm and the driving amplitude was calculated. Figure 3.24 illustrates the driving amplitude for each width. The amplitude shading coefficient is then calculated and given below:

Ring width in mm	Amplitude Shading
1	0.84
2	0.83
4	0.65
5	0.37
7.5	0.47
10	0.54
12	0.58
15	0.63
18	0.66
20	0.70

3.5.3 Choice of the annular ring width

In the previous section, it was shown that an optimum amplitude shading factor can be obtained by choosing the appropriate width of the assumed focal ring. Unfortunately, the amplitude shading factor is only one factor among many others that need to be considered in synthesizing an optimum heating pattern. Among those factors are the length of the focal region (depth of field), the intensity of the undesired hot spot (secondary foci) beyond the focal plane, and the high intensity region which appears on the main axis near the transducer. These different factors need to be considered when choosing the width of the assumed annular ring.

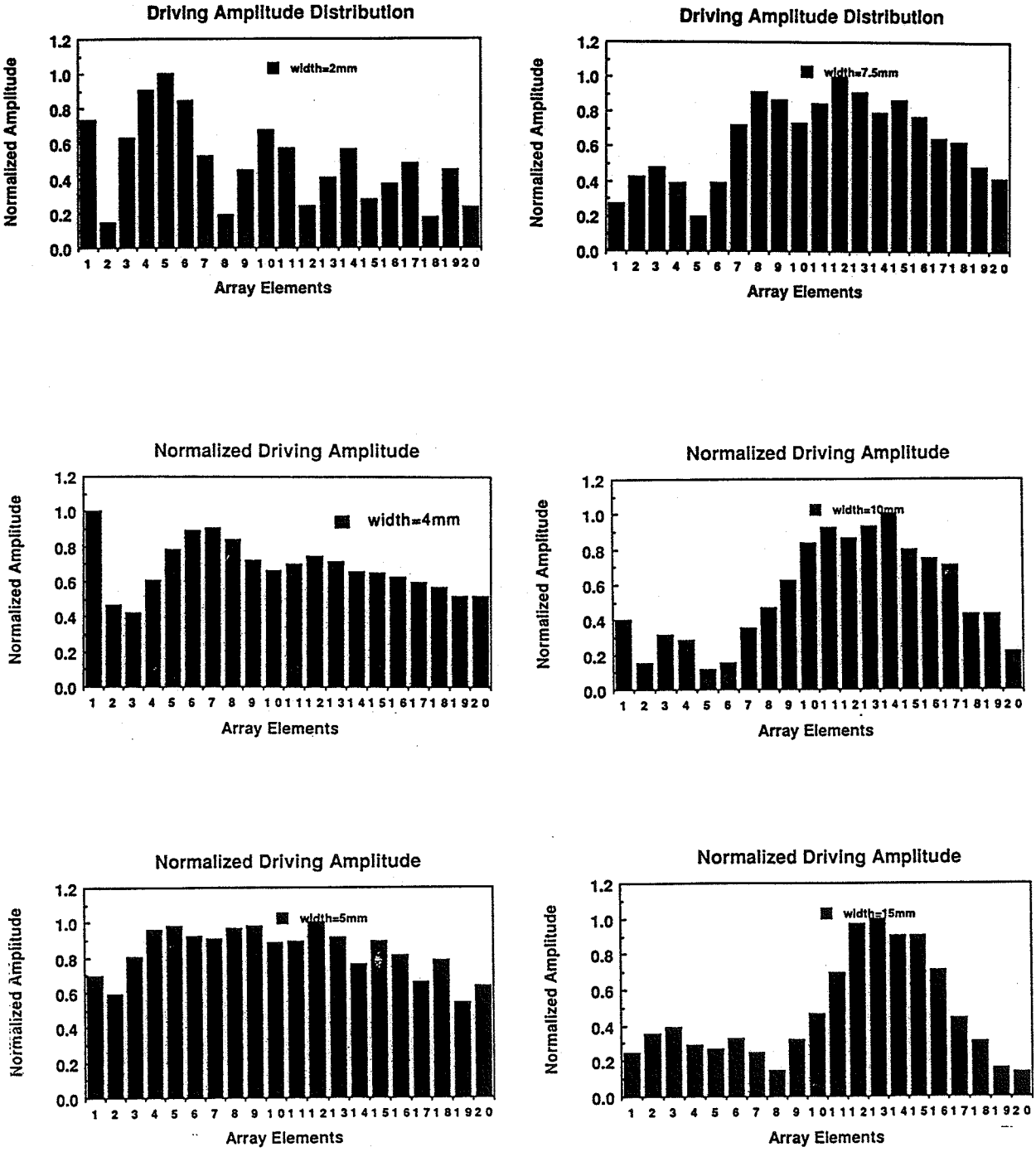

Figure 3.24. The normalized amplitude distribution as a function of the assumed annular source width. A 40 mm radius annular ring was assumed at 80 mm depth. The ring width was varied while keeping all other parameters fixed.

As demonstrated in Section 3.5.2, the choice of a 1 mm width annular ring of a 40 mm radius had led to a very high amplitude shading factor, which would limit the power output of the array to a small fraction of its maximum power output. On the other hand, when assuming annular rings with large widths ($> 3\lambda$), a substantial surface heating results, as demonstrated in Figures 3.25a) and b). Figure 3.25 is a contour plot of the pattern obtained from an attempt to synthesize a ring of 12 and 30 mm width, respectively. It is then necessary to determine an optimal range of focal widths which will maximize the power deposition at the tumor site without excessive surface heating while, at the same time, minimize the undesired hot-spot intensities. Moreover, the optimal focal width should result in a minimum amplitude shading factor in order to achieve therapeutic heating.

Simulations are conducted to solve this optimization problem with multiple constraints. Figure 3.26 illustrates the focal patterns obtained for annular ring widths ranging from 0.3 to 10λ (λ is the wavelength) at an operating frequency of 500 kHz. The synthesized annular ring is of a 30 mm radius at an 80 mm depth. Figure 3.27 is the surface plot of the pattern obtained when a full disk shaped source, of 60 mm radius, is assumed in the focal plane.

Although well behaved focal patterns result for all different widths, including the full disk shaped one, the corresponding contour plots in the longitudinal plane (r,z) suggest that surface heating occurs for a large width ($> 3\lambda$) as illustrated in Figure 3.25. Moreover, the driving amplitude control associated with thin rings ($< \lambda$) results in a high shading coefficient (see Section 3.4.2). Furthermore, a lower secondary focus intensity, when compared to that of the annular focus, results for annular sources with larger widths. This reduction of the secondary focus intensity is due to the splitting of the focused energy over a wider surface in the focal plane and consequently, the secondary focus (beyond the focal plane) is smoothed out.

In conclusion, the width of the assumed annular ring should not be very large in order to avoid surface heating. However, a very thin annular ring results in a high amplitude

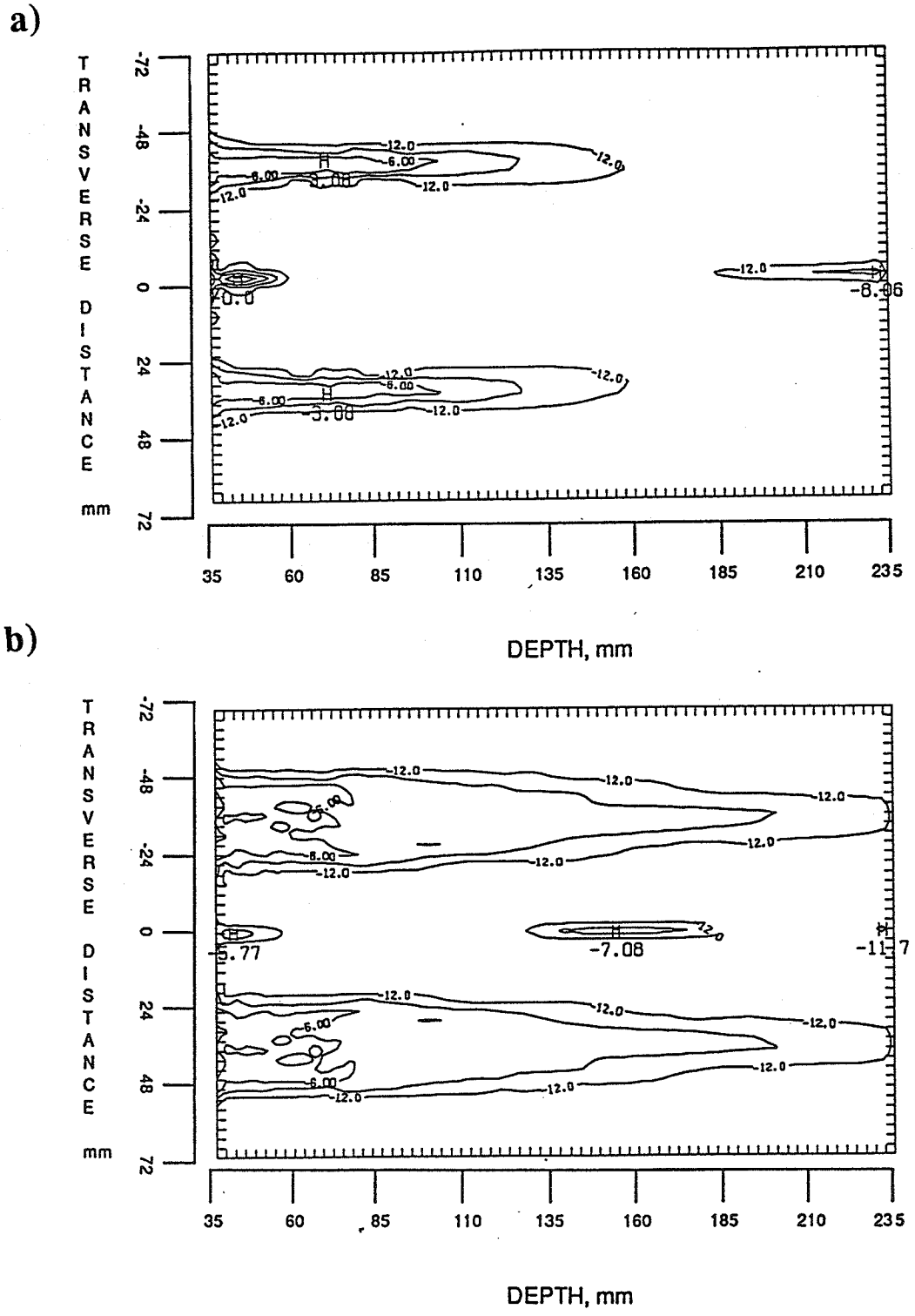

Figure 3.25. Surface heating resulting from large width annular rings. a) A contour plot of the pattern resulting when assuming a "ring" of 12 mm width in the focal plane (z= 80 mm) and b) resulting from assuming a 30 mm width annular source at 80 mm from the array surface.

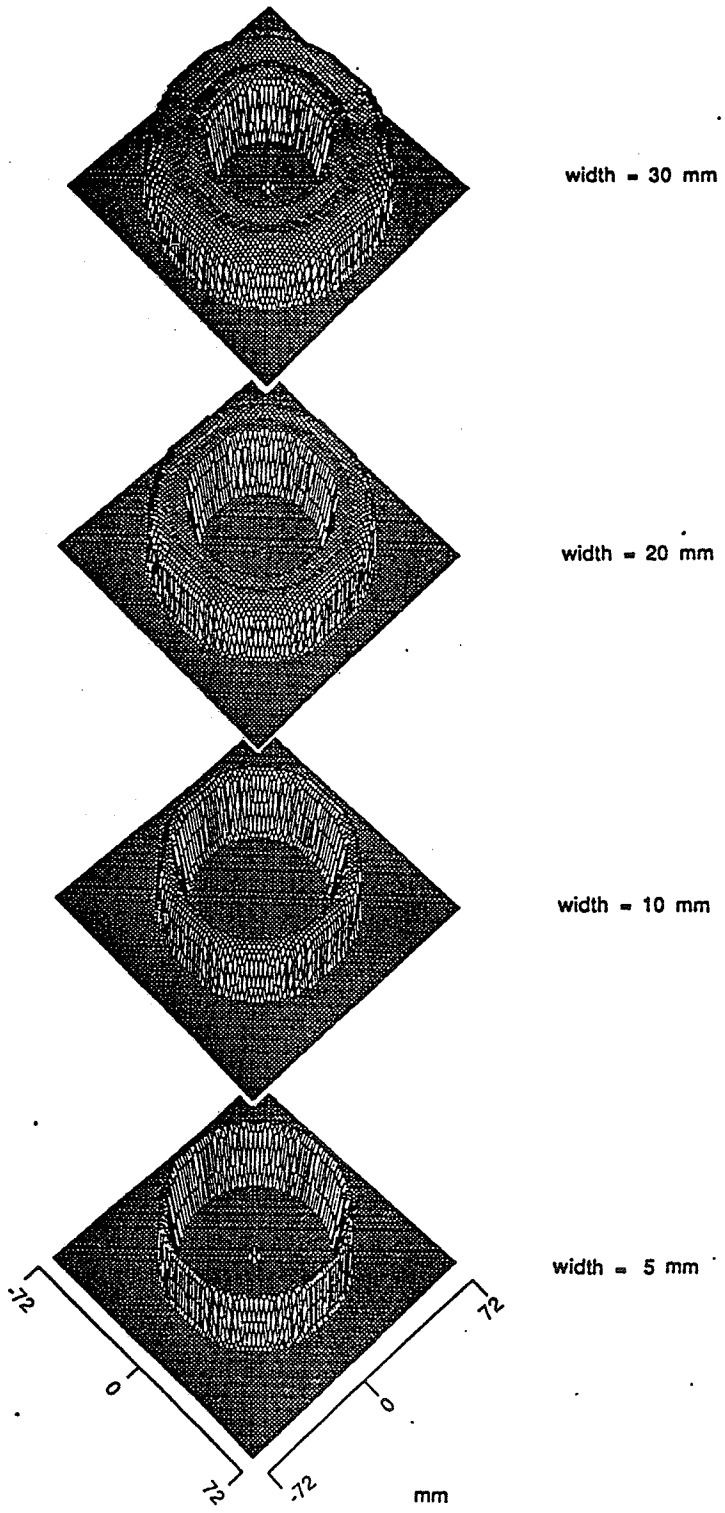

Figure 3.26. A surface plot of the the focal pattern (z=80) of a 30 mm radius annular ring synthesized using different width sources. Pattern resulting from 5, 10, 20, and 30 mm width rings are illustrated.

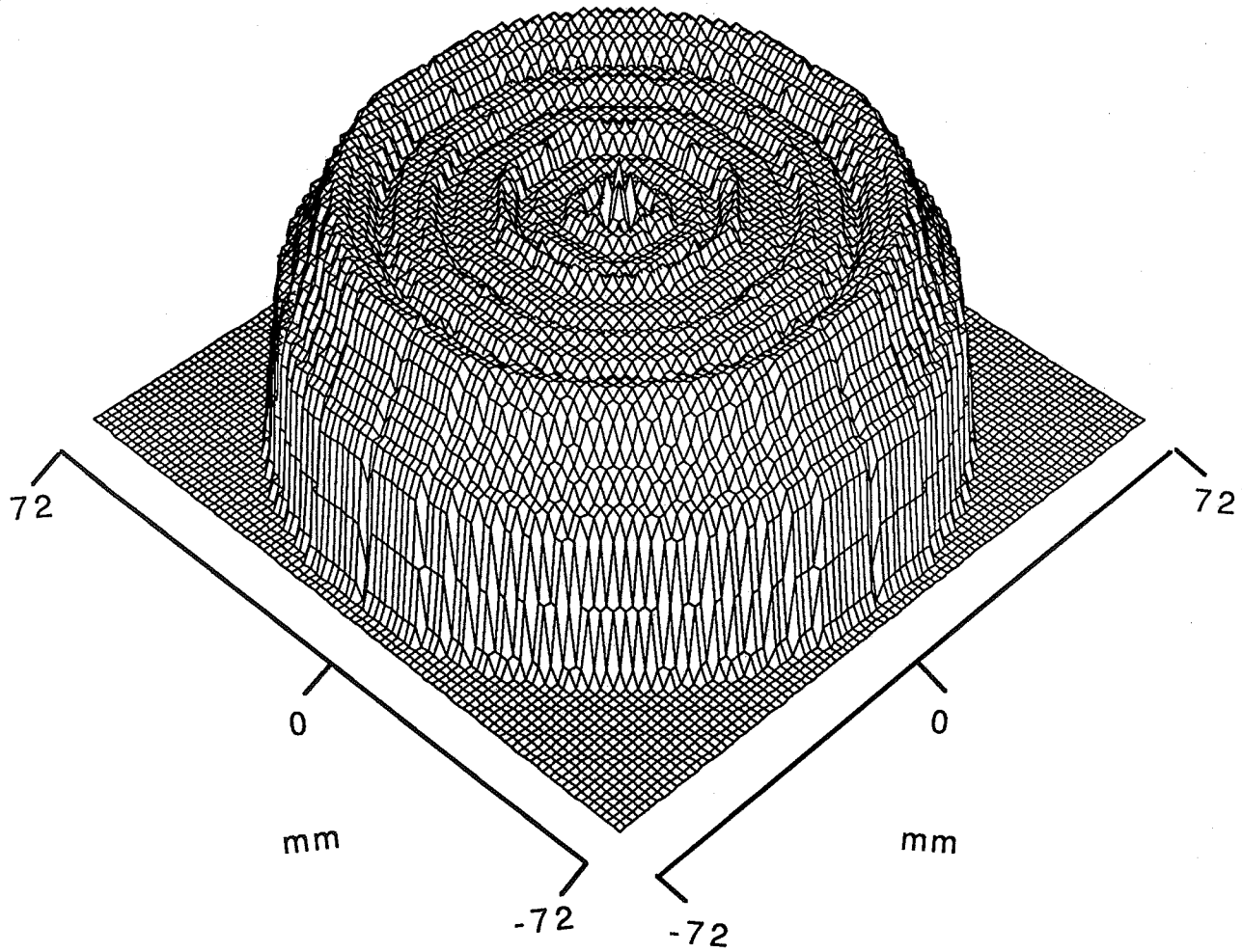

Figure 3. 27. A surface plot of the focal intensity profile (z=80) of a complete disk-shaped pattern. The pattern was synthesized by assuming a 60 mm radius disk (same size as the applicator) at 80 mm distance from the array surface.

shading coefficient and, consequently, a poor maximum extracted power. Simulations demonstrate that, for the synthesized focal depth and pattern radius, an optimum pattern was obtained for an annular source of a 5 mm width. It is necessary to conduct a similar series of simulations, for each case of synthesis, to determine the optimum width to be considered as this width depends necessarily on the synthesis parameters.

3.5.4 Array Gain

The intensity gain is defined as the ratio of the peak intensity at the focal site to that at the applicator surface (or at the skin surface). For a plane wave, this can be expressed as

$$G = \frac{I_z}{I_0} = e^{-2\alpha z} \tag{3.8}$$

where I_z and I_0 are the acoustic intensities evaluated at the tumor site and at the applicator surface respectively, α is the attenuation factor in NP/cm/MHz and z is the treatment depth in centimeters.

It is obvious that the value of G in Eq. (3.8) can only decrease exponentially for increasing depth. Moreover, its value is equal to unity at the surface z= 0 and less than unity for z>0 and, consequently, no gain is achieved by using plane waves. However, gain at depth can be achieved using focused transducers. For a focused transducer, the gain is obtained by the reduction of the cross-sectional area traversed by the sound beam [12]. Then Eq. (3.8) can be modified to account for the focusing effect as follows:

$$G = \frac{I_z}{I_0}\left(\frac{A_s}{A_t}\right) \tag{3.9}$$

where G is the intensity gain, A_s and A_t are the cross-sectional areas traversed by the sound beam at the skin surface and at the tumor site, respectively.

Equation (3.9) assumes that the effective surface of the applicator is driven by a constant amplitude control, which is not a valid assumption for the synthesis using the FCM.

This is due to the driving amplitude control required by the method. Hence, Eq. (3.9) needs to be modified to account for the amplitude shading factor. This is done as follows:

$$G = \frac{A_s}{A_t}(1-\varepsilon)\, e^{-2\alpha z} \tag{3.10}$$

It is obvious that for a fixed amplitude signal, Eq. (3.10) is reduced to Eq. (3.9), as expected ($\varepsilon = 0$). The frequency dependence of the gain factor is implicit and can appear by using

$$\alpha = \alpha_0 f \tag{3.11}$$

Equation (3.11) is a linear approximation of the empirical relation $\alpha=\alpha_0 (f)^h$, where α_0 is the attenuation in NP/cm at 1 MHz, f is the frequency in MHz, and h is a real number (h ~(0.8-1.3) for biological tissues) [40].

Finally, by using Eqs. (3.11) and (3.10), one gets

$$G = \frac{A_s}{A_t}(1-\varepsilon)\, e^{-2\alpha_0 f z}$$

and an explicit formula for the CRA gain can be derived by considering simple triangular similarities in Figure 3.28.

$$x = \frac{(F-d)R+r\,d}{F} \tag{3.12}$$

$$A_s = \pi \left[\frac{(F-d)R+r\,d}{F}\right]^2 \tag{3.13}$$

where As is the cross-sectional area traversed by the sound beam at the skin surface. By assuming a synthesized ring of width D, the cross-sectional area of the focal region is

$$\frac{A_s}{A_t} = \left[\frac{(F-d)R+r\,d}{F}\right]^2 \frac{1}{2Dr} \tag{3.14}$$

Using the simple geometrical presentation illustrated in Figure 3.28, an explicit expression for A_s/A_t as a function of the design parameters results. In the geometrical

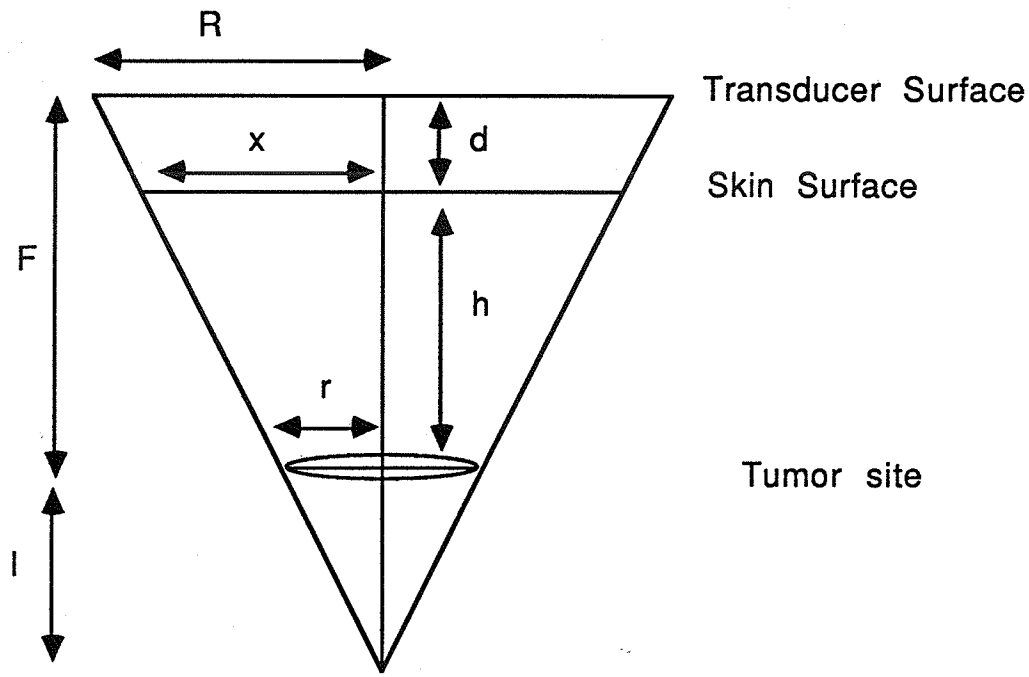

Figure 3.28. Geometry used in the CRA gain calculation.

illustration, R is the CRA radius, r is the tumor cross-sectional radius, d is the coupling medium (bolus) thickness, F is the focal depth, and h is the tumor depth from the skin surface. Finally, the CRA gain can be expressed as

$$G = \left[\frac{(F-d)R+r\,d}{F} \right]^2 \frac{(1-\varepsilon)}{2Dr} e^{-2\alpha_0 f\,(F-d)} \tag{3.15}$$

3.6 Analysis of the FCM : Advantages and Limitations

The ability of the CRA to produce conventional focusing (intense focal spot) on the main axis is well known [15]. Moreover, the ability of this configuration to produce annular heating patterns was investigated in [17]. In both cases, the synthesis method (referred to as the direct phasing method) consisted of establishing the driving phase necessary for each element by directly computing the distance separating the element center from the desired focus.

The field conjugation method, in addition to its ability to produce conventional and annular focusing, offers some unique advantages over the direct phasing method. These advantages include the generation of multiple foci and the production of annular rings with variable widths. Multiple focusing, if used appropriately, can be used to heat the back of the tumor as well as the front by carefully placing the treated volume between two foci. Moreover, focal rings with variable widths can be used to heat tumors with higher blood flow. Furthermore, it has been demonstrated that appropriate widths result in a lower secondary focus intensity compared to those produced by the direct phasing method.

In this section, the FCM is investigated and the characteristics of the conventional and annular heating patterns are compared to those produced by the direct phasing method.

3.6.1 Conventional focusing on the main axis.

By assuming a point source at the desired location on the primary axis, or by considering a small disk shaped source at the desired focal location, the FCM procedure is applied and the phase and amplitude of the driving signal are established.

Figure 3.10 is a contour plot of a conventional focus at a 100 mm depth from the applicator surface. The assumed source is a small disk of a 4 mm diameter placed at z=100 mm on the primary axis.

To investigate the characteristics of simple focusing on the main axis, the resulting focal region (3 dB region) was checked for different design parameters and the results confirmed those published by Huu and Hartemann [15]. Two different sets of simulations were conducted. In the first series of simulations, the F-number (F= focal distance/aperture diameter) was kept constant for different focal depths and the axial and lateral extensions of the focal region were measured. Those extensions were defined as the length and width of the 3 dB region, respectively. To obtain a constant F-number for different focal depths, the effective number of annular rings (effective applicator size) was adjusted to the desired focal depth. The simulation results are given in Table 3.3 for focal depths ranging from 50 to 120 mm and a constant f-number (0.96-1.06). Table 3.3 demonstrates the possibility of heating similar small volumes (~1cm^3) at different depths by varying the number of effective annular rings.

A second series of simulations consisted of varying the F-number while keeping the focal depth constant (z=120 mm). The F-number was varied by adjusting the number of excited annular elements (applicator diameter) for the same focal depth. Table 3.4 illustrates the data obtained for F-number varying from 0.8 to 1.5 for a constant focal depth. Under these conditions, the resulting focal region volumes ranged from 1 to 3 cm^3.

Table 3.3

Focal Region Dimensions for a Fixed F-number

Number of excited electrodes	Focal depth (F_d) in mm	F-Number F= (F_d/R)	Depth of field in mm	Lateral width of focal region in mm
8	50	0.96	20.9	3.37
10	60	1.00	23.9	3.38
12	70	1.02	23.1	3.61
13	80	0.97	23.0	3.60
15	90	1.00	24.0	3.62
17	100	1.02	24.0	3.62
18	110	0.97	23.5	3.61
20	120	1.00	24.5	3.6

Table 3.4

Focal Region Dimensions for Different Values of the F-number

Number of exited electrodes	F-Number F=Fd/R	Depth of field in mm	Lateral width of focal region in mm
20	1.00	24.5	3.66
18	1.10	31.5	4.01
16	1.20	32.0	4.20
15	1.3	36.2	4.57
14	1.42	41.3	4.75
13	1.53	44.5	4.83

Multiple focusing can also be produced by assuming point sources (or small disks) at the desired locations along the main axis. Elongated focal regions can be produced to accommodate special tumor geometries (see Section 3.4.1). In addition, heating the back as well as the front of a small tumor can be synthesized by producing separate foci at different depths as illustrated in Section 3.4.1.

3.6.2 Annular focal patterns.

By assuming an annular-shaped source at the location where an annular focal ring is to be produced, the driving signal needed to excite the different array electrodes can be established using the FCM. The size, width, and depth of the synthesized pattern are governed by those of the assumed source. Two methods of synthesis were discussed in this chapter: the FCM and the pseudo-direct method.

While the pseudo-direct method is somewhat similar to the direct phasing method, the FCM has two advantages over the direct phasing method. The first advantage is a more localized focal region (3 dB region) compared to that obtained by the direct phasing method . This property is the result of the assumption of a full annular ring as a fictitious source, in the focal plane, as compared to that of a point source. More precisely, the direct phasing method considers only the effect of the nearest side of the array to calculate the necessary phasing for each element. However, if the direct phasing method were modified to account for the farthest side of the array, a high intensity region (near the transducer), similar to that observed for the FCM, would have resulted. Figure 3.19a) illustrates the pattern obtained using the FCM to synthesize an annular ring of a 40 mm radius at an 80 mm depth. The extension of the 3 dB region (depth of field) is about 21 mm (7 λ) compared to the 51 mm (17 λ) length obtained by the direct phasing method as illustrated in 3.19b. Figure 3.18b) is the contour plot of the same pattern using the pseudo-direct method. The length of the 3 dB region is about 42 mm, which is twice the length of that produced by the FCM, but still shorter than that produced by the direct approach.

The second advantage is with respect to the hot spot (secondary focus) appearing on the main axis, beyond the focal plane in some cases. The normalized secondary focus produced by the FCM is at least 3.5 dB lower than those produced by the direct or pseudo-direct techniques for the same specifications. Figures 3.19a) and b) illustrate the pattern obtained from the synthesis of a 40 mm radius ring at an 80 mm depth using the FCM and the direct method, respectively. It is demonstrated that while the secondary focus intensity resulting from the FCM is about 7.5 dB less than that of the annular focus, the direct phasing method leads to about a 4.5 dB difference, which might prove inadequate to avoid distal bone heating.

One disadvantage associated with the FCM is the formation of a high intensity extension over a part of the main axis near the transducer. As mentioned earlier, this can be resolved by accounting for the high intensity region to fall within the coupling medium (bolus). However, this solution tends to limit the practical treatment depth to a few centimeters. Another solution consists of substituting the pseudo-direct method for the FCM by to reduce the high intensity extension. Furthermore, it was shown that the synthesis of small diameter annular patterns ($r < R_s$) would produce a strong secondary focus on the axis beyond the focal plane. To overcome these limitations, a method based on the combination of multiple focusing on the main axis with a simple mechanical movement of the applicator is proposed in the following section.

3.7 Simple and Multiple Focusing on the Main Axis Combined with Mechanical Scanning as a Means of Heating Deep Seated Tumors.

3.7.1 Motivation

The CRA configuration, investigated throughout this chapter, is well suited for the production of annular heating patterns. Two methods were proposed to directly synthesize annular foci, the FCM and the pseudo-direct method. The FCM, while capable of producing heating patterns judged as more suitable (secondary focus intensity, depth of

field,...,etc.) than those produced by other methods, is limited to the treatment of superficial tumors, as shown earlier. This limitation is due to the formation of a high intensity region prior to the focal plane as demonstrated in Section 3.4.1. In addition, a significant secondary focus might result beyond the focal plane if the direct or the pseudo-direct phasing method is used for the synthesis. This problem is more serious when the synthesis of focal rings of a smaller radius ($r< R_s$) is attempted. The production of annular heating patterns of large diameters ($r > R_s$) might not produce adequate time averaged intensity gain to produce therapeutic heating. In conclusion, annular heating patterns are expected to produce therapeutic effects at shallow depths (up to 5 cm for the applicator considered throughout this chapter).

Focusing on the primary axis results in very localized focal regions at depths ranging from very shallow to extremely deep in the body. In addition, multiple foci at different depths can be produced simultaneously as discussed in Section 3.4.1. However, the resulting focal regions are extremely small and cannot be used to heat even small tumors without some electrical or mechanical manipulation. To resolve this problem, it is proposed to produce a simple (or multiple) focusing on the main axis, and to mechanically scan the resulting focal spot (spots) over a predetermined trajectory. This technique has many advantages over the mechanical scanning of a fixed focus transducer. The advantages include the possibility of easily varying the depth of treatment, the capability of producing multiple focusing on the main axis at different depths which can be scanned simultaneously, and the elimination of any possibility of intervening tissue heating due to the highly localized focal regions produced on the primary axis. These different issues are discussed in detail in the following paragraphs to justify the combination of mechanical and electrical scanning which might appear very unusual.

The depth of the treatment can be adjusted electronically by simply varying the phase of the driving signal. This feature will allow the treatment of tumors at depths ranging from shallow to very deep in the body. This would have to be handled, in the case of a focused

transducer, by varying the thickness of the coupling medium (bolus), which would result in a more complicated transducer-patient interface.

Scanning of multiple foci on the main axis leads to unique heating patterns that cannot be obtained by scanning a fixed focus transducer. Among these patterns is heating the back, as well as the front, of a large tumor by simultaneously focusing at two depths and scanning the resulting pattern. This probably would have been achieved, in the case of traditional mechanical scanning, by the use of several transducers (arranged in different planes), which is complex, cumbersome and requires a complicated coupling medium (bolus).

By examining the contour plot of the pattern obtained by focusing at z= 100 mm on the main axis as illustrated in Figure 3.10a), it is clear that the focal region (the 3 dB region) extends to less than 13 mm while the power deposition intensity drops more than 10 dB in less than 5 mm away from this region. This very localized power deposition will allow the scanning of the tumor periphery without the risk of excessively heating the intervening tissues as frequently observed when using large focused transducers.

3.7.2 Method

The method consists of generating a focal spot (or multiple focal spots) along the array axis by electronically adjusting the phase and amplitude distribution to the array elements.This stationary field intensity profile is characterized by its spatial-peak temporal-peak (SPTP) value which coincides with the peak intensity at the focus (foci) when the array is focused at a point (points) along its main axis. However, the SPTP and the peak intensity at the focus could be different for other applications such as annular focusing which might lead, in some cases, to secondary foci with intensities higher than those evaluated at the focal site (i.e., near the transducer surface or far beyond the focal plane) as demonstrated earlier. The SPTP intensity is defined as the absolute maximum field intensity in time and space which might or might not be at the focal site as stated earlier. The stationary field

intensity pattern is then scanned mechanically over a desired trajectory (or surface) , i.e., single or multiple concentric rings. The mechanical scanning is assumed to be uniform and fast enough to avoid thermal ripples. The effect of scanning can be simulated by convoluting the stationary field intensity pattern resulting from the electronic focusing with a surface function h(r) as defined in [12],

$$h(r) = \begin{cases} 1 & \text{for } r \text{ within the surface A and identically zero elsewhere} \end{cases} \qquad (3.16)$$

where r is the radial distance from the main axis and A is the surface area of the scanned region, the scanned field intensity that results from scanning the stationary field profile $I_0(r)$ over a surface s is obtained by performing the following convolution integral [12],

$$I(r) = A^{-1} \int_S I_0(r-r')\, h(r')\, d^2r' \qquad (3.17)$$

where h(r) is as defined above, s is the scanned surface, and d^2r is an elementary surface over s.

To simulate the mechanical scanning over an annular surface of inner and outer radius r_1 and r_2, respectively, it is only necessary to modify h(r) and S of Eq. (3.17) as follows:

$$h(r) = \begin{cases} 1 & r_1 \le r \le r_2 \text{ and zero elsewhere} \end{cases} \qquad (3.18)$$

with s is now the surface of the annular region and the time-averaged field intensity is simulated by evaluating Eq. (3.17).

3.7.3 Simulations and results

In the following simulations, a concentric-ring applicator of 20 annular elements is assumed. The annular elements are of an individual width of 3 mm each with center-to-

center spacing of 4 mm. An operating frequency of 500 kHz was chosen to allow a deep penetration of ultrasound in tissue-like media (> 10 cm). The tissue attenuation coefficient and the ultrasound velocity in tissue-like media were taken to be 1 dB/cm/MHz and 1500 m/s, respectively.

The CRA was first focused at Z=70 mm along its main axis. The contour plot of the field intensity pattern in the (r,Z) plane is shown in Figure 3.29a). Figure 3.29b) is the normalized amplitude distribution needed for this synthesis as established by the FCM. The amplitude shading factor for this distribution was computed and found to be 0.69. This amplitude shading factor was improved by applying the logarithmic scaling procedure as explained in Chapter 2. The new amplitude distribution is shown in Figure 3.29c). This new distribution resulted in an amplitude shading factor of 0.39. The spatial-peak temporal-peak (SPTP) focal intensity gain is found to be 22.3 dB. This focal intensity gain was also evaluated using Eq. (3.15) and found to be 23.4 dB. An SPTP focal intensity of 638 W/cm^2 is computed at the focal site assuming that the annular electrodes are capable of producing a surface intensity of 4 W/cm^2. To simulate scanning, the convolution integral was evaluated for a disk-shaped surface of 35 mm radius. The resulting field intensity pattern is shown in Figure 3.30a). The scanned field intensity gain of the resulting pattern is 5.95 dB. However, when the convolution integral was evaluated over an annular ring of inner and outer radii of 9 and 15 mm, respectively, the annular heating pattern of Figure 3.30b) was produced. The scanned field intensity gain evaluated at the focal site was 15.09 dB. These patterns will be used as inputs to the BHTE, and their associated temperature distributions will be discussed in Chapter 5.

An elongated focus is also generated by simultaneously focusing at 60 and 80 mm (along the axis) from the array surface. The contour plot of the resulting field intensity pattern is illustrated in Figure 3.31a). An SPTP focal intensity of approximately 432 W/cm^2 was evaluated compared to 648 W/cm^2 for the previous case. The convolution integral was

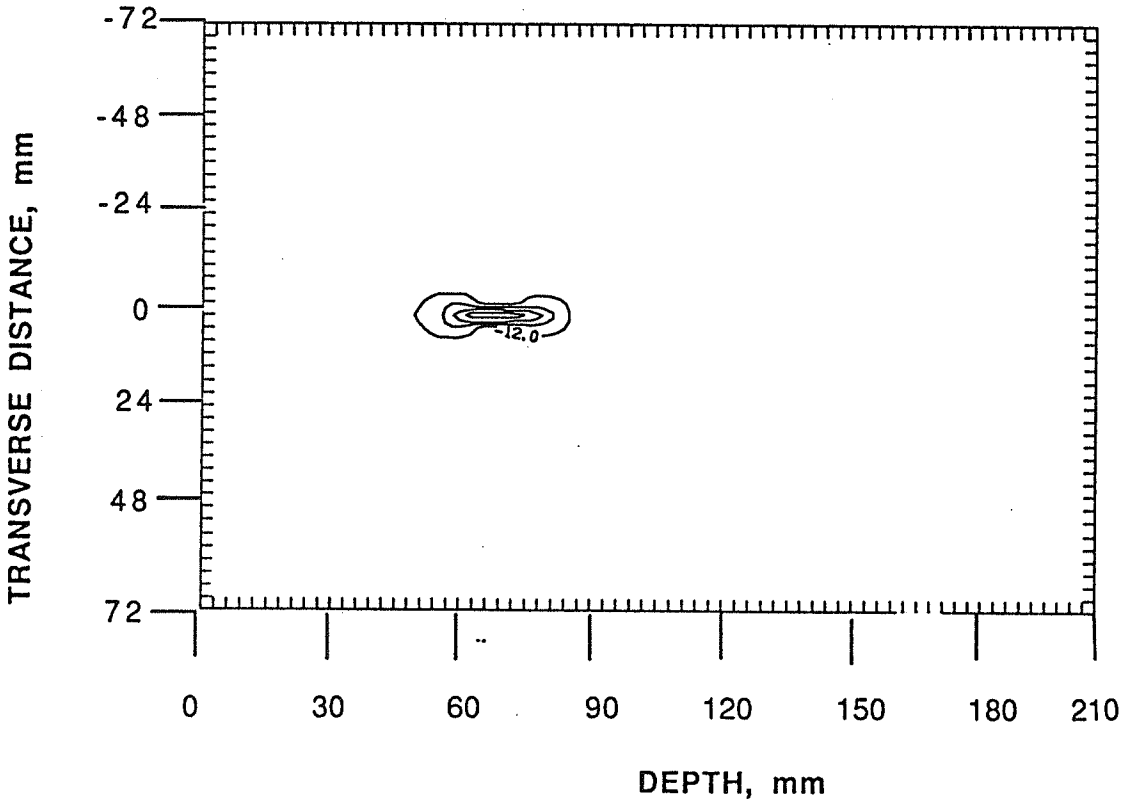

Figure 3.29. Synthesis of a conventional foci along the axis. a) A contour plot of the pattern resulting from focusing at (0,0,70) along the array axis. The lowest contour level is -12 dB and contours are given at 3 dB intervals.

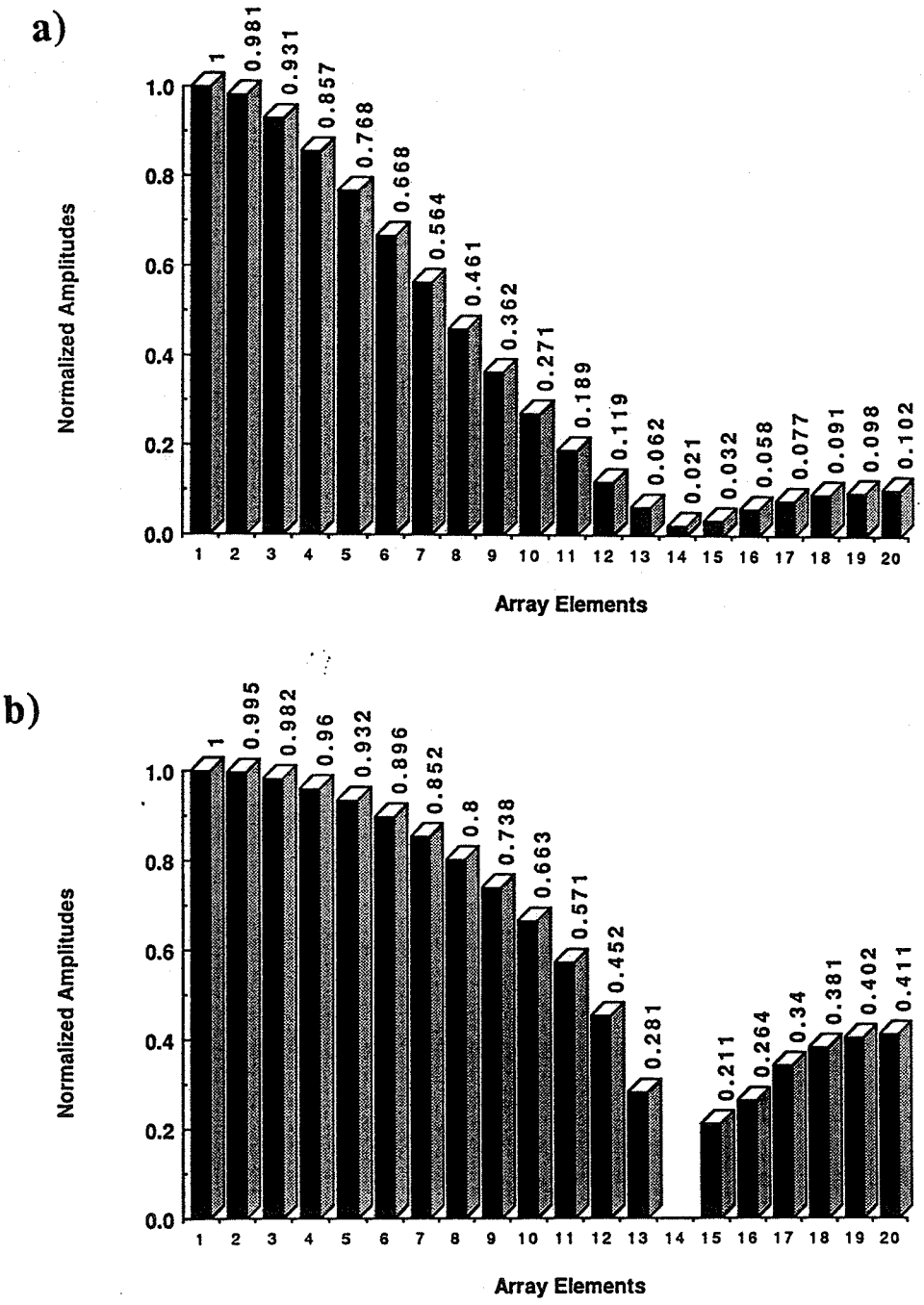

Figure 3.29. b) Normalized amplitude distribution of the excitation signal required by the FCM for the synthesis of (a) and b) is the normalized driving amplitude distribution logarithmically scaled as described in Chapter 2.

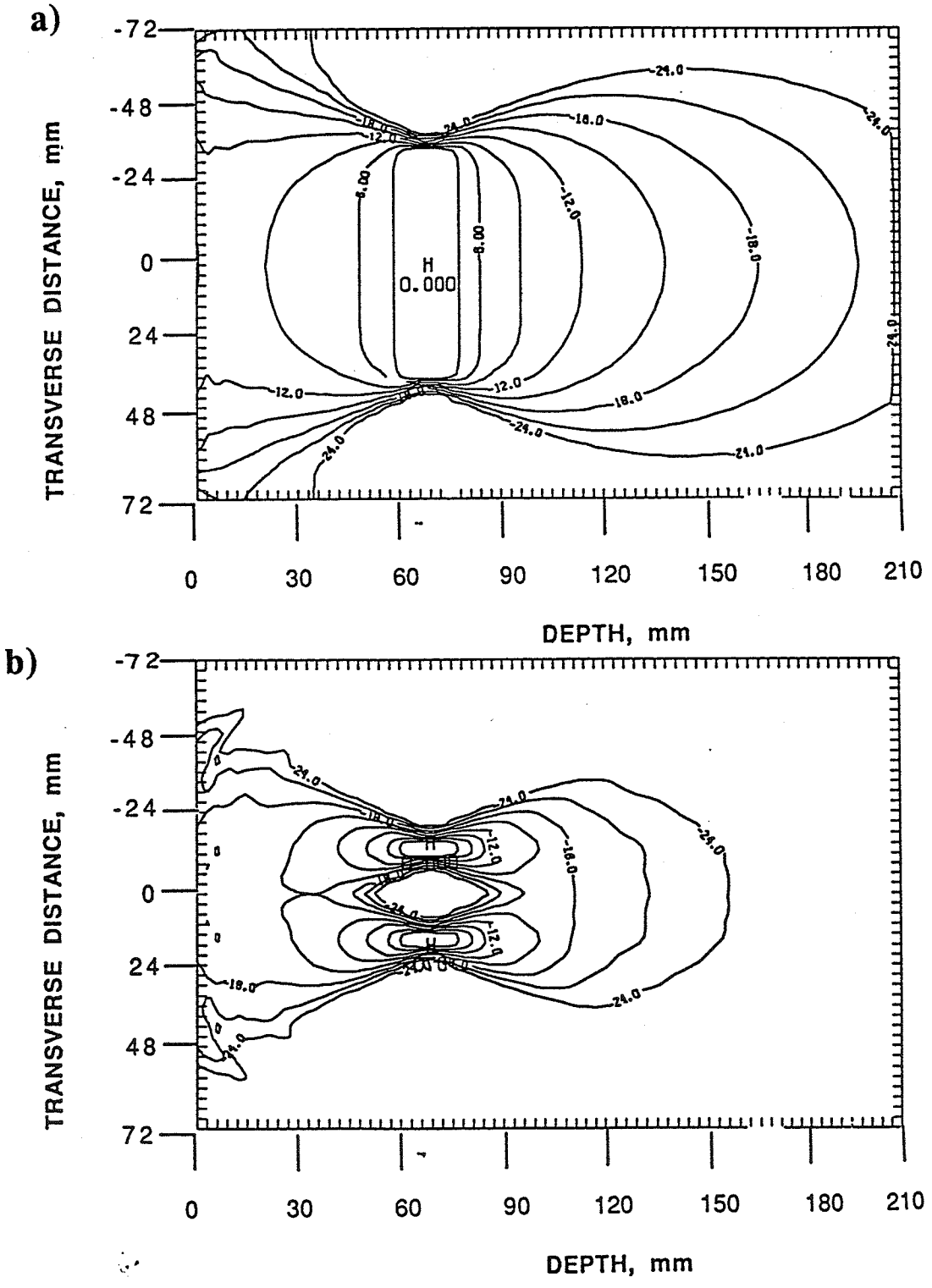

Figure 3.30. Simulated intensity profiles resulting from mechanical scanning. a) Scanned field (time-averaged) intensity over a disk 35 mm radius and b) is the time-averaged intensity produced by scanning the array over an annular ring of 9 and 15 mm, respectively. Lowest contour level is -24 dB and contours are given at intervals of 3 dB.